Available on the CMS information server **CMS AN-18-277**

The Compact Muon Solenoid Experiment

CMS Draft Note

Mailing address: CMS CERN, CH-1211 GENEVA 23, Switzerland

2019/07/17
Archive Hash: fc79902-D
Archive Date: 2019/07/17

Search for new phenomena in events with an opposite-sign same-flavor pair with the Run 2 dataset

C. Fernández Madrazo[2], P. Martínez Ruiz del Árbol[2], S. Sánchez Cruz[3], B. Sathia Narayanan[4], M. Teroerde[1], and G. Zevi Della Porta[4]

[1] RWHT Aachen
[2] Instituto de Física de Cantabria
[3] Universidad de Oviedo / ICTEA
[4] University of California, San Diego

Abstract

A search is presented for physics beyond the standard model in final states with two opposite-sign same-flavor leptons, jets, and missing transverse momentum. The data sample corresponds to an integrated luminosity of 140 fb^{-1} of proton-proton collisions at $\sqrt{s} = 13$ TeV collected with the CMS detector at the CERN LHC in Run 2. The analysis focuses on searches for a kinematic edge in the invariant mass distribution of the opposite-sign same-flavor lepton pair and electroweakly produced resonances compatible with the Z boson mass. The observations are consistent with expectations from standard model processes and are interpreted in terms of upper limits on the production of supersymmetric particles.

Contents

1 Introduction

This Note presents a search for physics beyond the standard model (BSM) in events containing a pair of same-flavor (SF) opposite-sign (OS) leptons, jets, and missing transverse energy (), in a sample of pp collisions at a centre-of-mass energy of 13 TeV. The data sample was collected with the Compact Muon Solenoid (CMS) detector at the Large Hadron Collider (LHC) in 2016 and corresponds to an integrated luminosity of 140 fb^{-1}. The OS SF final state can occur in BSM models in three ways:

1. through the production of an on-shell Z boson, in which case the invariant mass of the lepton pair is compatible with the Z boson mass;
2. through the production of a virtual Z/γ^{*} boson in the cascade decay of a heavy particle, such as ;
3. in the cascade decay of a heavy particle producing a pair of OS SF leptons, such as $\to \ell\tilde{\ell} \to \ell^{+}\ell^{-}$, where is the next-to-lightest neutralino, is the lightest neutralino, and is a slepton.

Case (1) leads to an excess over SM background on the Z mass peak, while in cases (2) and (3) the invariant mass distribution exhibits a characteristic edge. In the following, we present searches for BSM physics processes corresponding to the three signatures mentioned above.

Briefly describe simplied models that motivate the search

We exploit the fact that in dileptonic $\mathrm{t\bar{t}}$ and WW events the two lepton flavors are uncorrelated and use a sample of $e^{\pm}\mu^{\mp}$ events to estimate this background in $e^{+}e$ and $\mu^{+}\mu$ events. This also covers any BSM decay chain that would equally produce OS same-flavor and opposite-flavor (OF) lepton pairs. We additionally exploit data-driven methods to estimate the contribution of processes with instrumental missing transverse momentum in processes that are non flavor symmetric.

2 Datasets, triggers, and Object Selection

2.1 Datasets and triggers

Change desccription of unblinded policy

The most dominant datasets in this analysis are the di-leptonic streams of 13 TeV p-p collision data recorded by CMS at a bunch spacing of 25 ns. The list of the analyzed samples is given below in Table 1. It is worthwhile to state already here that the collision data in the signal regions (described in chapter 3) were blinded before pre-approval except for the 12.9 fb^{-1} that were covered in the version of this analysis that was published for the ICHEP conference (SUS-16-021) and 4.4 fb^{-1} of Run2016G data. The data outside the signal regions (i.e. in the control regions for measurement of background estimation quantities etc.) was not blinded. Besides the di-leptonically triggered datasets, orthogonally triggered datasets were used for the study of the di-lepton trigger efficiencies. All events used for the final event counts in the three — ee, $e\mu$, and $\mu\mu$ — channels were made sure to be assigned to the correct triggering dataset.

Add all datasets

Additionally, Table 2 lists the most important SM Monte-Carlo samples used in this analysis. The simulation is normalized to luminosity using cross sections from `https://twiki.cern.ch/twiki/bin/viewauth/CMS/SummaryTable1G25ns`.

MiniAODv2 samples are used consistently for data and MC.

Table 1: Collision datasets analyzed in the course of the analysis. All samples are of the `MINIAOD` data format.

Name
/DoubleEG/Run2016B-03Feb2017_ver2-v2/MINIAOD
/DoubleEG/Run2016(C-G)-03Feb2017-v1/MINIAOD
/DoubleEG/Run2016H-03Feb2017_ver2-v1/MINIAOD
/DoubleEG/Run2016H-03Feb2017_ver3-v1/MINIAOD
/MuonEG/Run2016B-03Feb2017_ver2-v2/MINIAOD
/MuonEG/Run2016(C-G)-03Feb2017-v1/MINIAOD
/MuonEG/Run2016H-03Feb2017_ver2-v1/MINIAOD
/MuonEG/Run2016H-03Feb2017_ver3-v1/MINIAOD
/DoubleMuon/RRun2016B-03Feb2017_ver2-v2/MINIAOD
/DoubleMuon/Run2016(C-G)-03Feb2017-v1/MINIAOD
/DoubleMuon/Run2016H-03Feb2017_ver2-v1/MINIAOD
/DoubleMuon/Run2016H-03Feb2017_ver3-v1/MINIAOD
/JetHT/Run2016B-03Feb2017_ver2-v2/MINIAOD
/JetHT/Run2016(C-G)-03Feb2017-v1/MINIAOD
/JetHT/Run2016H-03Feb2017_ver2-v1/MINIAOD
/JetHT/Run2016H-03Feb2017_ver3-v1/MINIAOD

Update list of triggers for the three years Change to met control triggers

Table 2: Simulated SM datasets analyzed in the course of the analysis. All samples are of the `MINIAOD` data format. `Moriond17` is an abbreviation for `RunIISummer16MiniAODv2-PUMoriond17_80X_mcRun2_asymptotic_2016_TrancheIV_v6/` and `Tune` is short for the pythia8 tune `CUETP8M1`.

Name	$\sigma_{process}$ (pb)
/TTo2L2Nu_TuneCUETP8M2_ttHtranche3_13TeV-powheg-pythia8/Moriond17-v1	87.31
/TTToSemilepton_TuneCUETP8M2_ttHtranche3_13TeV-powheg-pythia8/Moriond17-v1	364.31
/DYJetsToLL_M-50_Tune_13TeV-madgraphMLM-pythia8/Moriond17_ext1-v2	6025.2
/DYJetsToLL_M-10to50_Tune_13TeV-madgraphMLM-pythia8/Moriond17-v1	18610.
/ST_s-channel_4f_leptonDecays_13TeV-amcatnlo-pythia8_Tune/Moriond17-v1	3.36
/ST_tW_antitop_5f_NoFullyHadronicDecays_13TeV-powheg_Tune/Moriond17_ext1-v1	11.7
/ST_tW_top_5f_NoFullyHadronicDecays_13TeV-powheg_Tune/Moriond17_ext1-v1	11.7
/ST_t-channel_antitop_4f_inclusiveDecays_13TeV-powhegV2-madspin-pythia8_Tune/Moriond17-v1	124.
/ST_t-channel_top_4f_inclusiveDecays_13TeV-powhegV2-madspin-pythia8_Tune/Moriond17-v1	208.
/ZZTo2L2Q_13TeV_amcatnloFXFX_madspin_pythia8/Moriond17-v1	3.28
/ZZTo2L2Nu_13TeV_powheg_pythia8/Moriond17-v1	0.520
/ZZTo4L_13TeV_powheg_pythia8/Moriond17-v1	1.256
/WZTo2L2Q_13TeV_amcatnloFXFX_madspin_pythia8/Moriond17-v1	5.595
/WZTo3LNu_Tune_13TeV-amcatnloFXFX-pythia8/Moriond17-v1	4.40
/WWTo2L2Nu_13TeV-powheg-pythia8/Moriond17-v1	10.481
/WWZ_Tune_13TeV-amcatnlo-pythia8/Moriond17-v1	0.165
/WZZ_Tune_13TeV-amcatnlo-pythia8/Moriond17-v1	0.05565
/ZZZ_Tune_13TeV-amcatnlo-pythia8/Moriond17-v1	0.01398
/TTZToLLNuNu_M-10_Tune_13TeV-amcatnlo-pythia8/Moriond17_ext1-v1	0.2529
/TTZToQQ_Tune_13TeV-amcatnlo-pythia8/Moriond17-v1	0.5297
/TTWJetsToLNu_Tune_13TeV-amcatnlo-madspin-pythia8/Moriond17-v1	0.2043
/TTWJetsToQQ_Tune_13TeV-amcatnloFXFX-madspin-pythia8/Moriond17-v1	0.4062
/ttHToNonbb_M125_TuneCUETP8M2_ttHtranche3_13TeV-powheg-pythia8/Moriond17-v1	0.215
/ttHTobb_M125_TuneCUETP8M2_ttHtranche3_13TeV-powheg-pythia8/Moriond17-v1	0.293
/VHToNonbb_M125_13TeV_amcatnloFXFX_madspin_pythia8/Moriond17-v1	0.952
/tZq_ll_4f_13TeV-amcatnlo-pythia8/Moriond17_ext1-v1	0.0758
/TTTT_TuneCUETP8M2T4_13TeV-amcatnlo-pythia8/Moriond17-v1	0.009103

On the trigger side, the selection is dominated by the di-lepton signature. Trigger paths asking for isolated leptons are utilized as the main triggers. Due to the changes in instantaneous luminosity, different di-lepton triggers were active at different times and with varying prescales. Thus, a variety of triggers with slighlty different requirements are used. Non isolated double lepton paths are considered as well to increase the efficiency in events with a high dilepton system p_{T}. Supporting triggers are used for the study of the trigger efficiencies taken from hadronic events. All triggers which are used one way or the other are documented in Table 3.

Table 3: Triggers used in the analysis. The first section are the triggers used in most control and signal regions, while the supporting triggers are mostly for the calculation of the trigger efficiencies of the signal triggers.

Pathname
Signal triggers
HLT_Mu17_TrkIsoVVL_Mu8_TrkIsoVVL_v⋆
HLT_Mu17_TrkIsoVVL_Mu8_TrkIsoVVL_DZ_v⋆
HLT_Mu17_TrkIsoVVL_TkMu8_TrkIsoVVL_v⋆
HLT_Mu17_TrkIsoVVL_TkMu8_TrkIsoVVL_DZ_v⋆
HLT_Ele17_Ele12_CaloIdL_TrackIdL_IsoVL_DZ_v⋆
HLT_Ele23_Ele12_CaloIdL_TrackIdL_IsoVL_DZ_v⋆
HLT_Mu8_TrkIsoVVL_Ele17_CaloIdL_TrackIdL_IsoVL_v⋆
HLT_Mu8_TrkIsoVVL_Ele23_CaloIdL_TrackIdL_IsoVL_v⋆
HLT_Mu8_TrkIsoVVL_Ele23_CaloIdL_TrackIdL_IsoVL_DZ_v⋆
HLT_Mu17_TrkIsoVVL_Ele12_CaloIdL_TrackIdL_IsoVL_v⋆
HLT_Mu23_TrkIsoVVL_Ele8_CaloIdL_TrackIdL_IsoVL_v⋆
HLT_Mu23_TrkIsoVVL_Ele8_CaloIdL_TrackIdL_IsoVL_DZ_v⋆
HLT_Mu23_TrkIsoVVL_Ele12_CaloIdL_TrackIdL_IsoVL_v⋆
HLT_Mu23_TrkIsoVVL_Ele12_CaloIdL_TrackIdL_IsoVL_DZ_v⋆
HLT_Mu27_TkMu8_v⋆
HLT_Mu30_TkMu11_v⋆
HLT_Mu30_Ele30_CaloIdL_GsfTrkIdVL_v⋆
HLT_Mu33_Ele33_CaloIdL_GsfTrkIdVL_v⋆
HLT_DoubleEle33_CaloIdL_GsfTrkIdVL_v⋆
HLT_DoubleEle33_CaloIdL_GsfTrkIdVL_MW_v⋆
Supporting triggers
HLT_PFHT125_v⋆
HLT_PFHT200_v⋆
HLT_PFHT250_v⋆
HLT_PFHT300_v⋆
HLT_PFHT350_v⋆
HLT_PFHT400_v⋆
HLT_PFHT475_v⋆
HLT_PFHT600_v⋆
HLT_PFHT650_v⋆
HLT_PFHT800_v⋆
HLT_PFHT900_v⋆

2.2 Physics Objects

The main driving principle behind the identification and isolation requirements on the leptons is their symmetry after applying these selections. To simplify the analysis it is desirable, if not necessary, to keep the ratio of the muon and electron efficiencies close to unity. The selection presented in the following assure this ratio to be close to one. Kinematically, the most important selection on both lepton flavors stems from the trigger requirement of $p_{\mathrm{T}} > 23, 17, 12,$ and 8 GeV depending on the exact path. Full efficiency for any of these three values is reached at a p_{T} of 25(20) GeV for the leading (trailing) lepton , which is the cut applied to all leptons. One specific selection of this analysis is that not only the electrons are rejected if they appear in the crack between the barrel and the endcap, but also the muons. The reason for this is simply that the flavor symmetric background is taken from $e\mu$ events, thus the necessety of having symmetric cuts not only on the efficiency but also on the fiducial regions. For this reason any lepton within the $|\eta|$ region of 1.4 to 1.6 is rejected.

In addition, selection criteria on jets, , and b-tagging are presented, which all follow standard CMS SUSY recommendations (including the leptons).

2.2.1 Electrons

Update electron definition Table 4 summarizes briefly the most important selection criteria for electrons. Besides kinematical selections, an MVA-trained identification discriminator is used. The discriminator is optimized on electrons from prompt W-boson decays in $\mathrm{t\bar{t}}$ versus leptons stemming from so-called “fakes”[1] in $\mathrm{t\bar{t}}$. The used working point for the MVA identification discriminator corresponds to the SUSY-PAG-recommended “tight” value, developed at the end of 2016. The actual MVA cut value depends on the lepton p_{T} and $|\eta|$. In each $|\eta|$ bin the lower value is used for electrons with $p_{\mathrm{T}} > 25$ GeV while the cut decreases linearly from the upper to the lower value for p_{T} between 15 and 25 GeV. Additionally, conversion rejection cuts are applied.

As isolation variable, the mini-isolation is used which features a shrinking cone-size with increasing p_{T} of the lepton. Thus, the cone size in which the PF particles are summed to calculate the relative isolation is no longer constant, but a function of the p_{T} of the lepton

$$R = \frac{10.}{min\left[max\left(p_{\mathrm{T}}, 50\right), 200\right]} \quad .$$

For p_{T} values below 50 GeV, this leads to a constant cone size of 0.2. For p_{T} values between 50 GeV and 200 GeV, the cone size shrinks from 0.2 to 0.05 at which it remains for higher p_{T} leptons.

Corrections to the isolation are applied by subtracting the average energy density ρ from the effective geometrical area of the lepton’s isolation cone. The variable cone size is taken into account for this correction.

2.2.2 Muons

Selection for the muons follow POG recommendations and are summarized in Table 5. All the variables used are standard variables, and the isolation variable is also mini-isolation.

---

[1] “Fake” leptons are mostly semi-leptonic b-quark decays where $b \to cW \to c\ell\nu$

Table 4: Electron selection criteria.

cut	value
Kinematics	
p_T	> 25 (20) GeV
$\|\eta\|$	< 2.4
$\|\eta\|$	$\ni [1.4, 1.6]$
Identification	
MVA tight	2016 Working point
conversion rejection	maxLostHits == 0 passConversionVeto()
Isolation	
mini Isolation	< 0.1
Impact parameter	
d_{xy}	0.05
d_z	0.10
SIP3D	< 8

Table 5: Muon selection criteria.

cut	value
Kinematics	
p_T	> 25 (20) GeV
$\|\eta\|$	< 2.4
$\|\eta\|$	$\ni [1.4, 1.6]$
Identification	
medium Muon ID (POG)	
Isolation	
mini Isolation	< 0.2
Impact parameter	
d_{xy}	0.05
d_z	0.10
SIP3D	< 8

2.2.3 Loose leptons

Add complete definition of the third lepton veto For the electroweak search a veto on loosely isolated third leptons are applied. Tables 6 and 7 summarize the loose lepton selections. All the variables used are standard variables, and the isolation variable is also mini-isolation. In order to improve the veto efficiency, the events are rejected if there is an isolated third lepton, or an isolated track as defined in the MT_2 analysis [?].

Table 6: Electron selection criteria for the electroweak third lepton veto.

cut	value
Kinematics	
p_{T}	> 10 GeV
$\|\eta\|$	< 2.5
Identification	
MVA loose	$>$ -0.96 to -0.86 ($\|\eta\| < 0.8$)
	$>$ -0.96 to -0.85 ($\|\eta\| < 1.479$)
	$>$ -0.95 to -0.81 ($\|\eta\| < 2.4$)
conversion rejection	maxLostHits == 0
	passConversionVeto()
Isolation	
mini Isolation	< 0.4
Impact parameter	
d_{xy}	0.05
d_z	0.10
SIP3D	< 8

Table 7: Muon selection criteria for the electroweak third lepton veto.

cut	value
Kinematics	
p_{T}	> 10 GeV
$\|\eta\|$	< 2.4
Identification	
medium Muon ID (POG)	
Isolation	
mini Isolation	< 0.4
Impact parameter	
d_{xy}	0.05
d_z	0.10
SIP3D	< 8

2.2.4 Lepton pair selection

Since there are some events with multiple lepton pairs, it is important to define an unambiguous way of selecting the "relevant" opposite-sign, same-flavor lepton pair. The implemented algorithm is rather straight forward as it selects the two highest p_{T} leptons which are fully identified and that have a distance between them of 0.1 in ΔR. This is to say, there is no cross-cleaning or prioritization between electrons and muons applied, and non-identified leptons (including the crack region) do not enter in the consideration of the lepton pair selection. This is motivated by the expected SUSY signal in which real leptons stemming from the decay of heavy particles are expected to be "clean" (i.e. well identified) and have rather large p_T. Lepton pairs are additionally required to have an invariant mass of > 20 GeV. To be consistent with the p_T requirement for the photons in the MET-template method (see AN-16-468), the p_T of the dilepton system is required to be > 25 GeV. Update dilepton pt cut to 50

2.2.5 Jets and E_T^{miss}

Update JECs, jet ID, b-tagging and met filters Add fat jet selection Jet selection is rather straightforward as well and follows standard selectors and corrections. The p_T of the selected jets is 35 GeV and the $|\eta|$ is required to be < 2.4. They are required to be seperated from selected leptons by 0.4 in ΔR. Jet energy corrections are applied, namely the `Spring16_23Sep2016V2` set for data and for MC, which is the recommended recipe from the JERC group. At least two such jets are selected for all signal and control regions of this analysis.

With these selected jets, the quantity H_T is formed by simply summing the scalar p_T values of all the jets.

Tagging b-quark jets is done by the CSV algorithm optimized for 13 TeV data. For a b-veto in the electroweak search the p_T cut on the b-jets is lowered to 25 GeV.

Corrected ("Type-1") is used for the analysis. Several filters rejecting events where known problems were present have been applied. The names of these filters are the following: primary vertex, CSC beam halo, HBHE noise, HBHEiso noise, eebadSC, and Ecal TP. The detailed description of these filters can be found in the official page of the MET POG[2]. Additional ad-hoc filters are used that were proposed on the SUSY hypernews [3]. These filters veto events either have PFMET/caloMET > 5 or contain a jet that has $p_T > 200$ GeV, a muon fraction > 0.5, and $\Delta\phi$(jet,MET) $> \pi - 0.4$.

2.2.6 MT_2

The leptonic MT_2 variable is used to define the signal region in the electroweak search. It is defined as documented in references [? ?]. It is in essence a generalization of the transverse mass for pair-produced particles which decay into visible objects and invisible ones. In this case, the visible objects are the two selected leptons and the invisible objects either two LSPs from signal processes, or neutrinos in the case of di-leptonic $t\bar{t}$. This variables proves to be very efficient to suppress the $t\bar{t}$ background and is therefore used in parts of the analysis.

2.3 Summary of minimal event selection

Update minimal event selection, as slepton regions do not have jets To summarize, the following list gives all the details of the minimal event selection used for the analysis.

- two selected leptons of opposite charge with $p_T > 25$ GeV for the leading and $p_T > 20$ GeV for the trailing lepton
- the two highest p_T leptons are selected for this pair
- > 20 GeV, di-lepton system $p_T > 25$ GeV
- between the two leptons of > 0.1
- two selected jets with $p_T > 35$ GeV, $|\eta| < 2.4$ each, > 0.4 away from any lepton passing the criteria established for analysis signal-like leptons (Sec. 2.2.1 and 2.2.2).

---

[2] https://twiki.cern.ch/twiki/bin/viewauth/CMS/MissingETOptionalFiltersRun2

[3] https://hypernews.cern.ch/HyperNews/CMS/get/susy/2265.html

- no minimal requirement. Cuts on are applied according to signal and control regions

3 Signal Models and Signal Regions

This section describes the set of targeted SUSY models along with a short description of their decays and expected signatures in the detector. Furthermore, the signal regions derived from these expectations are described.

3.1 Signal Models

Our search is targeting different modes of the neutralino decay into a final state with two opposite sign same flavor leptons and coming from the LSP. In order to study this kind of processes we have considered two Simplified Models, one producing a resonant lepton signature through an on-shell Z mass and the other producing an edge like distribution in the invariant mass of the leptons.

The signal model for the edge search, *T6bbslepton*, is based on the pair-production of sbottom-squarks , which decay to the next-to-lightest neutralino and a b-quark. It is designed to exhibit mass edges given by the mass differences between the and . The decay $\rightarrow \ell\ell$ can happen either via an (off-Shell) Z boson or via intermediate sleptons . The masses of the sleptons ($\tilde{e}, \tilde{\mu}$) are assumed degenerate and set to be in between the masses of and , given by the relation $m = m + \frac{m-m}{2}$. The mass of the is fixed to 100 GeV, while and masses are scanned. The decay of the is now possible either via virtual or real Z bosons or intermediate sleptons, as shown in the Feynman graph in Figure 1. The Z^* boson decays according to its SM branching fractions, sometimes producing a charged lepton pair $\ell^+\ell^-$ (ℓ = e, μ).

The models for the EWK search, *TChiWZ* and *TChiHZ*, are based on the production of a neutralino and chargino undergoing Z, Higgs and W production and the LSP. The diagrams for two EWK models and the *T6bbslepton* can be seen in Fig. 1.

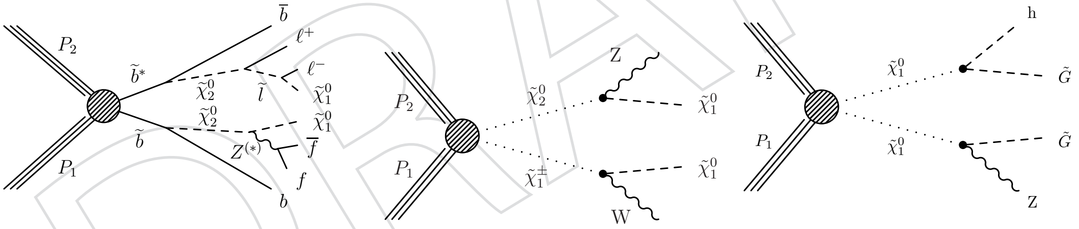

Figure 1: (Left) Feynman diagram for pair production and decays realized in the T6bbslepton simplified model. The model features pair production and the occurrence of mass edges in the decay of a via an intermediate slepton. (Middle) Diagram corresponding to the TChiWZ model of neutralino/chargino production decaying into vector bosons and the LSP. (Right) Diagram corresponding to the TChiHZ model of neutralino neutralino production decaying into a Z or a Higgs boson and the LSP.

3.2 Signal Regions

The selection of signal regions follows closely the expected signatures from the previous section. They can be divided into two separate categories, one with electroweak production and an on-shell Z-boson in the final state and the other with strong production and without a resonance at the Z-boson mass.

A baseline signal region is defined by requiring:

- MET $> 150\,\mathrm{GeV}$,
- at least two jets,

- $> 80\,\mathrm{GeV}$,
- $|\Delta\phi(\mathrm{jet}_{1,2}, MET)| > 0.4$

With the much increased cross section of $\mathrm{t\bar{t}}$ at 13 TeV, some reduction had to be achieved. The distribution should exhibit a sharp drop-off at the mass of the W boson for a perfectly measured $\mathrm{t\bar{t}}$ event, and therefore it was chosen as the main discriminating variable. In practice the distribution extends slightly beyond the W boson mass (see 2) due to jet mismeasurements, resolution and other experimental effects. Since the MC modeling of this kind of effects is not necessarily very trustworthy, we kept the requirement to a moderate level to allow enough statistics to apply a data driven technique to predict the remaining $\mathrm{t\bar{t}}$. Therefore, a requirement at exactly 80 GeV was chosen and not tighter. Furthermore, once the $\mathrm{t\bar{t}}$ background is reduced by a large amount, the remaining background that can be optimized is DY+jets with fake-$E_{\mathrm{T}}^{\mathrm{miss}}$. This is reduced by requiring the $|\Delta(\phi)|$ between the $E_{\mathrm{T}}^{\mathrm{miss}}$ vector and the leading jets.

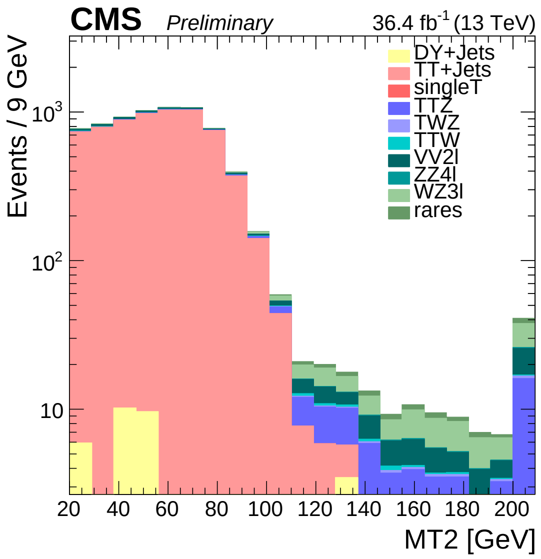

Figure 2: distribution for MC simulation events in a signal region with two same flavor leptons, more than 2 jets and $E_{\mathrm{T}}^{\mathrm{miss}} > 150\,\mathrm{GeV}$.

Except for the 8 TeV and ICHEP edge legacy regions, all signal regions require this baseline selection.

3.2.1 Electroweak on-Z signal regions

The signal regions targeting the TChiWZ model requires the following cuts in addition to the baseline selection (and with the exception of the MET cut):

- $86 < \;< 96\,\mathrm{GeV}$,
- a veto on additional loose leptons or isolated tracks with $p_{\mathrm{T}} > 10\,\mathrm{GeV}$,
- a veto on b-jets with $p_{\mathrm{T}} > 25\,\mathrm{GeV}$,
- the invariant mass of the two jets with closest $|\Delta\phi|$ has to be lower than $110\,\mathrm{GeV}$ ($m_{jj} < 110 GeV$).

The signal region is divided into four bins in $E_{\mathrm{T}}^{\mathrm{miss}}$: $100-150\,\mathrm{GeV}$, $150-250\,\mathrm{GeV}$, $250-350$and above $350\,\mathrm{GeV}$. The logic behind this selection is to follow the $E_{\mathrm{T}}^{\mathrm{miss}}$ binning of the on-Z search in order to minimize confusion, as well as the move from a $E_{\mathrm{T}}^{\mathrm{miss}}$ and jet-binned signal region to something more optimal for searches for electroweak signals.

The signal regions targeting the TChiHZ model in turn require the following in addition to the baseline selection (and exception the MET and the cuts):

- $86 < < 96\,\mathrm{GeV}$,
- a veto on additional loose leptons or isolated tracks with $p_{\mathrm{T}} > 10\,\mathrm{GeV}$,
- exactly two b-jets with $p_{\mathrm{T}} > 25\,\mathrm{GeV}$,
- the invariant mass of the two b-jets $m_{bb} < 150\,\mathrm{GeV}$
- the variable formed with the 2 b-jets $M_{T2bb} > 200\,\mathrm{GeV}$.

This signal region is then binned in 3 $E_{\mathrm{T}}^{\mathrm{miss}}$ bins: : $100 - 150\,\mathrm{GeV}$, $150 - 250\,\mathrm{GeV}$, and above $250\,\mathrm{GeV}$.

3.2.2 Edge Signal Regions

The edge search consists of two parts. On the one hand, a kinematic fit is performed on the distribution in the baseline signal region to search for a kinematic edge. On the other hand, a counting experiment is performed. For the counting experiment, the baseline signal region is further subdivided into 14 exclusive signal regions that are defined in 7 bins in and 2 (described in section 4.5) bins :

- bins [GeV]: [20-60, 60-86, 96-150, 150-200, 200-300, 300-400, 400+],
- $\mathrm{t\bar{t}}$ like: < 21,
- not $\mathrm{t\bar{t}}$ like: ≥ 21

The bins give sensitivity for edge like features in different parts of the phase space. The binning divides the remaining events again in a $\mathrm{t\bar{t}}$ like and non-$\mathrm{t\bar{t}}$ like category. The exact value of greater and smaller than 21 was chosen because this corresponds to the 95% $\mathrm{t\bar{t}}$ efficiency point. Studies comparing this new binning with additional mass bins and the cut show a significant improvement in the analysis' sensitivity. Fig. 3 compares the expected exclusion contour derived in the 2016 ICHEP PAS (SUS-16-021) using 2 mass and 2 bins to the expected limits with the same strategy for the full dataset and to the new binning with the additional bins and the cut. It can be observed that the new binning increases the sensitivity at low masses by about 150 GeV which is caused by the newly introduced cut. The additional mass bins at high dilepton mass significantly increase the sensitivity to points with high masses. This is caused by the fact, that the background in the high bins is small, while high masses correspond to high edge positions and thus deposit most of the signal events in the high mass bins

Two additional counting signal regions are defined because of the observed deviations in 8 TeV data (see SUS-12-019) and in the 2016 ICHEP PAS (SUS-16-021). These regions are defined to repeat the exact same analysis (modulo new objects definitions) and thus do not use the baseline signal region.

The 8 TeV legacy signal region is defined as:

- MET > 150 (100) GeV, and at least two (three) jets,
- $20 < < 70\,\mathrm{GeV}$,
- $|\eta| < 1.4$ for both leptons
- $|\Delta(R)| > 0.3$ between the leptons

The ICHEP legacy signal region is given by:

- MET $> 150\,\mathrm{GeV}$,

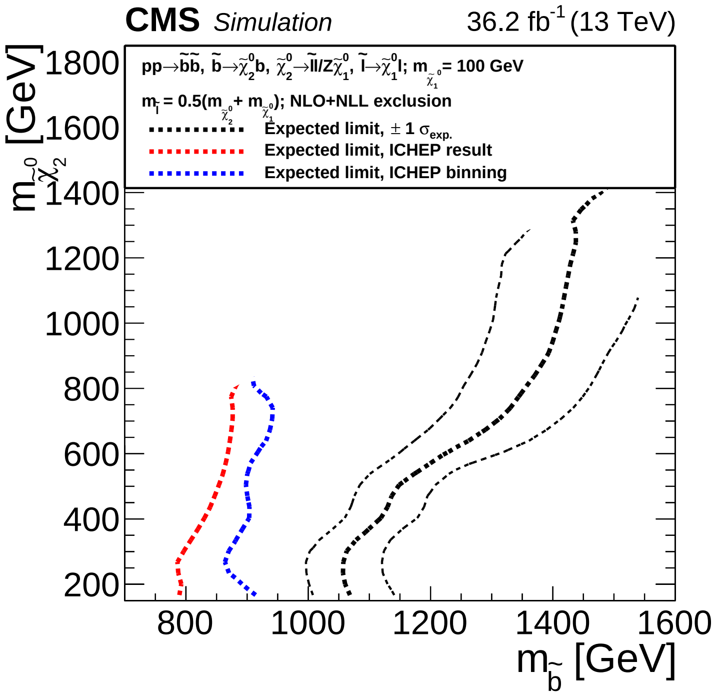

Figure 3: Comparison of the expected limits of the edge analysis strategy in the 2016 ICHEP PAS, the expected limits when applying the same binning to the full dataset, and the expected limits for the new signal regions using and more bins.

- at least two jets,
- $>$ 101 GeV,
- not $t\bar{t}$ like: ≥ 21

4 Standard Model Background Predictions

As mentioned before, the main backgrounds to this analysis stem from the DY process and $\mathrm{t\bar{t}}$. While opposite-sign lepton pairs from $\mathrm{t\bar{t}}$ are produced flavor-symmetric, i.e, the theoretical probability of an $e\mu$ pair is equal to the probability of ee + $\mu\mu$; the DY process produces only same-flavor leptons and has its main contribution in the mass range around the mass of the Z boson. The estimation of the non flavor symmetric backgrounds is described in a seperate note (AN-16-468).

4.1 Flavor-symmetric Background

Any physical process which features decays into same flavor and opposite flavor lepton pairs with equal probability is comprised in this background estimation. This is, first and foremost, the $\mathrm{t\bar{t}}$ process, but also other processes such as WW, or ttW production. Other processes such as WZ production or ttZ and ttH production have some flavor symmetric component and some component stemming from the decay of the Z boson. Their contribution will be discussed separately later on.

Our flavor-symmetric background prediction in SF events utilizes the number of OF events as follows:

$$\begin{aligned} N_{\mathrm{ee}} &= R(\mathrm{ee}/OF) \times N_{OF} \\ N_{\mu\mu} &= R(\mu\mu/OF) \times N_{OF} \\ N_{SF} \equiv N_{\mathrm{ee}} + N_{\mu\mu} &= R_{SF/OF} \times N_{OF} \end{aligned} \tag{1}$$

At particle level (and before any FSR), the mapping ratios R are simply $R_{\mathrm{ee}/OF} = R_{\mu\mu/OF} = 0.5$ and $R_{SF/OF} = 1$. (Note that the OF sample size is two times that of the ee or $\mu\mu$ samples). Since trigger, reconstruction and identification efficiencies are not identical for detected electrons and muons, the factor $R_{SF/OF}$ is not longer one, but a quantity that depends on the efficiencies in a slightly more complicated form.

The following naming scheme is used here: A quantity without an upper index includes all efficiencies (trigger, selection and reconstruction), a $''^{*}''$ indicates that only reconstruction and selection efficiencies are applied, while $''^{hard}''$ stands for the quantity on particle level. Furthermore, the assumption is made that the reconstruction and selection efficiencies for the two leptons in the event have a negligible correlation, i.e. $\epsilon_{\ell\ell} = \epsilon_{\ell} \cdot \epsilon_{\ell}$.

An important quantity is the ratio of efficiencies for muons to electrons:

$$\begin{aligned} r_{\mu/e} &= \frac{\epsilon_{\mu}}{\epsilon_{e}} \approx \sqrt{\frac{\epsilon^{*}_{\mu\mu}\epsilon^{T}_{\mu\mu}}{\epsilon^{*}_{ee}\epsilon^{T}_{ee}}} = \sqrt{\frac{N_{\mu\mu}}{N_{ee}}} \\ r_{\mu/e} &\approx r^{*}_{\mu/e}\sqrt{\frac{\epsilon^{T}_{\mu\mu}}{\epsilon^{T}_{ee}}} \end{aligned} \tag{2}$$

Using this quantity one can estimate the number of ee and $\mu\mu$ events in the following way:

$$
\begin{aligned}
N_{ee} &= \epsilon^T_{ee} N^*_{ee} = \epsilon^T_{ee}\left(\epsilon^*_e\right)^2 N^{hard}_{ee} = \frac{1}{2}\epsilon^T_{ee}\left(\epsilon^*_e\right)^2 N^{hard}_{OF} = \frac{1}{2}\epsilon^T_{ee}\frac{\epsilon^*_e}{\epsilon^*_\mu}N^*_{OF} \\
&= \frac{1}{2}\frac{1}{r^*_{\mu/e}}\frac{\epsilon^T_{ee}}{\epsilon^T_{e\mu}}N_{OF} = \frac{1}{2}\frac{1}{r_{\mu/e}}\frac{\sqrt{\epsilon^T_{ee}\epsilon^T_{\mu\mu}}}{\epsilon^T_{e\mu}}N_{OF} \\
N_{\mu\mu} &= \epsilon^T_{\mu\mu} N^*_{\mu\mu} = \epsilon^T_{\mu\mu}\epsilon^{*2}_{\mu} N^{hard}_{\mu\mu} = \frac{1}{2}\epsilon^T_{\mu\mu}\epsilon^{*2}_{\mu} N^{hard}_{OF} = \frac{1}{2}\epsilon^T_{\mu\mu}\frac{\epsilon^*_\mu}{\epsilon^*_e}N^*_{OF} \\
&= \frac{1}{2}r^*_{\mu/e}\frac{\epsilon^T_{\mu\mu}}{\epsilon^T_{e\mu}}N_{OF} = \frac{1}{2}r_{\mu/e}\frac{\sqrt{\epsilon^T_{ee}\epsilon^T_{\mu\mu}}}{\epsilon^T_{e\mu}}N_{OF}
\end{aligned}
\tag{3}
$$

The combined prediction for the SF yield is therefore

$$
\begin{aligned}
N_{SF} &= \frac{1}{2}\left(r_{\mu/e} + \frac{1}{r_{\mu/e}}\right)\frac{\sqrt{\epsilon^T_{ee}\epsilon^T_{\mu\mu}}}{\epsilon^T_{e\mu}}N_{OF} \\
&= \frac{1}{2}\left(r_{\mu/e} + \frac{1}{r_{\mu/e}}\right)R_T N_{OF} = R_{SF/OF}N_{OF}
\end{aligned}
\tag{4}
$$

This parametrization underlines the advantage of using the combined SF sample compared to the separate $\mathrm{e^+e^-}$ and $\mu^+\mu^-$ samples. While $R_{\ell\ell/OF}$ is directly affected by the differences in reconstruction and trigger efficiencies by the factors or $r^{-1}_{\mu/e}$, these differences partially cancel out in . In order to get to a final value for , two approaches have been taken. The first is a direct measurement of the ratio in data in a control region enriched in $\mathrm{t\bar{t}}$, while the second consists of the separated estimation of the and R_T factors.

4.1.1 Direct measurement of

This procedure uses the ratio between SF and OF events in a control region enriched in $\mathrm{t\bar{t}}$. This control is defined orthogonal to the signal regions in terms of jets and . It lies just outside them in order to not be affected by a large extrapolation. The exact selections for this -measurement control region are:

- the same lepton selection
- exactly two jets
- between 100 and 150 GeV
- $70 < \; < 110$ GeV excluded

No cut is applied since it would significantly reduce the $\mathrm{t\bar{t}}$ background and thus the available statistics. The control region is shown in Fig. 4 as the green area below the signal region. The part of the phase space with 3 or more jets and 100-150 GeV of is part of the 8 TeV legacy region and thus not added to the control region.

A large mass window around the Z boson mass is excluded to avoid the contamination with Drell–Yan backgrounds. The numerical values are shown in Tab. 8. The results on data and MC agree within about 2% for the combination of both flavors. If the flavors are treated seperately,

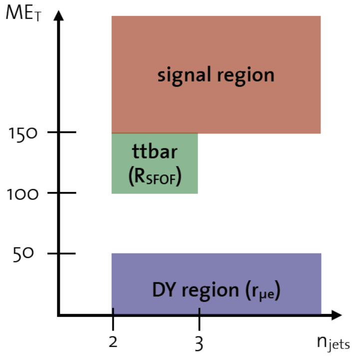

Figure 4: Location of the signal region and the control regions for measuring and in the versus plane.

the data MC agreement is between 1 and 3%. Only the combination of both flavors is used in the analysis.

As a closure test, the ratio of in the control and signal region (transfer factor) on simulation is studied. It is found to be compatible with unity within 2% for the combination of both flavors and for each flavor seperately.

Table 8: Observed event yields in the control region and the resulting values for $R_{SF/OF}$, $R_{ee/OF}$, and $R_{\mu\mu/OF}$ for both data and MC. The transfer factor is defined as the ratio of $R_{SF/OF}$ in the signal region devided by $R_{SF/OF}$ in the control region.

	N_{SF}	N_{OF}	$R_{SF/OF} \pm \sigma_{stat}$	Transfer factor $\pm\sigma_{stat}$
Data	13438	12138	1.107±0.014	–
MC	13289.5	12188.8	1.090±0.005	1.004±0.005
	N_{ee}	N_{OF}	$R_{ee/OF} \pm \sigma_{stat}$	Transfer factor $\pm\sigma_{stat}$
Data	4976	12138	0.410±0.007	–
MC	4851.8	12188.8	0.398±0.003	1.017±0.007
	$N_{\mu\mu}$	N_{OF}	$R_{\mu\mu/OF} \pm \sigma_{stat}$	Transfer factor $\pm\sigma_{stat}$
Data	8462	12138	0.697±0.010	–
MC	8437.7	12188.8	0.692±0.004	0.996±0.006

To evaluate possible dependencies when extrapolating from control to signal region and determine a systematic uncertainty, the ratio is displayed in Fig. 5 as a function of several important observables for both data and MC. The data shows some fluctuations due to the limited statistics in the control region, but no clear trends are observed.

A systematic uncertainty of 4% is found to be sufficient to cover differences between data and MC and fluctuations in important observables.

4.1.2 Measurement of via and (Factorization method)

In order to calculate according to Eq. 4, and have been measured in data.

Measurement of

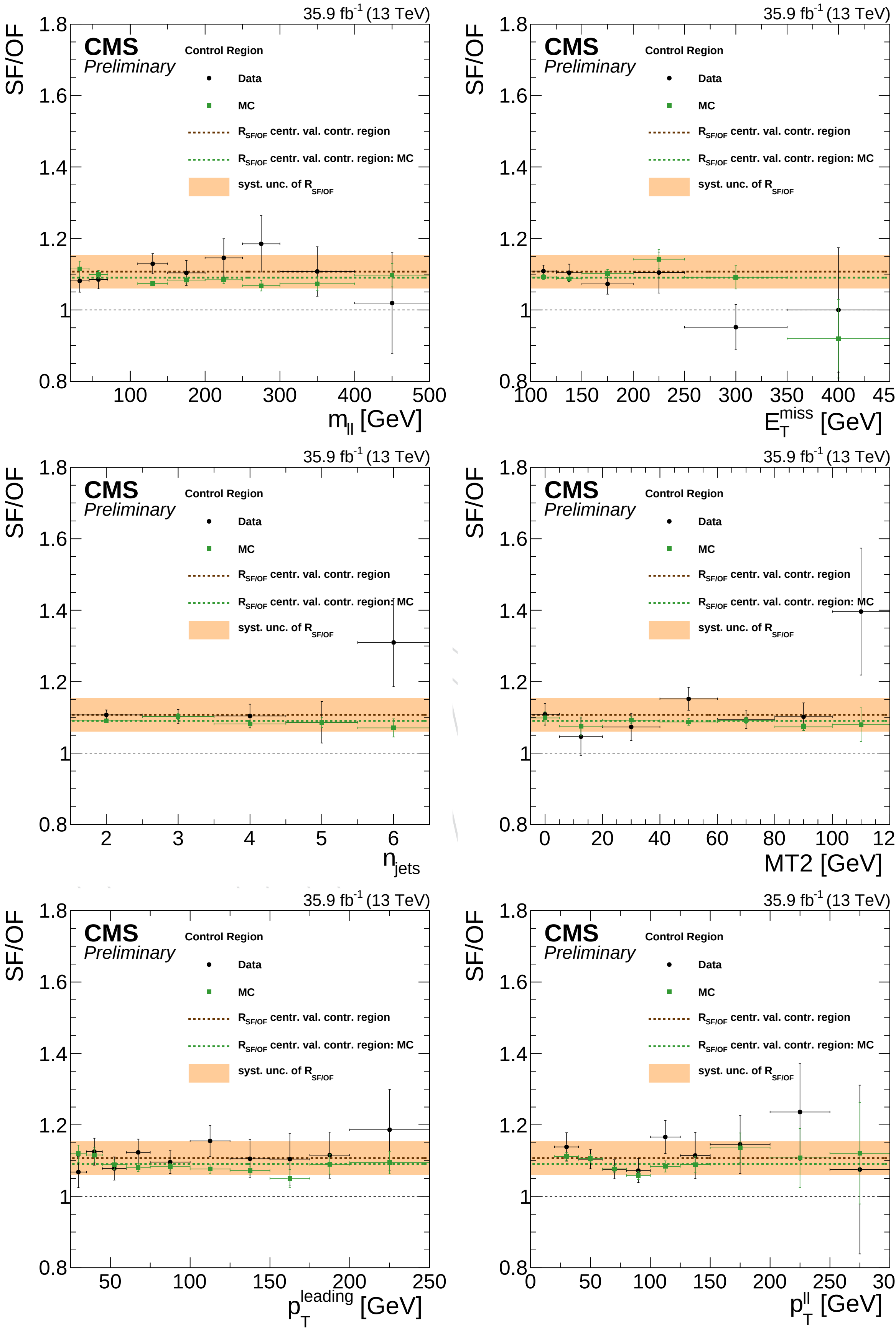

Figure 5: Direct measurement of in the control region for data and MC. Dependencies on the invariant mass of lepton-pair(top left), $E_{\mathrm{T}}^{\mathrm{miss}}$ (top right), jet count (left center), (right center), p_{T} of the first lepton (bottom left), and p_{T} of the dilepton system (bottom right) are shown. The assigned 4% systematic uncertainty on is indicated by the orange band.

The measurement of is performed in the Drell–Yan control region specified in Figure 4, utilizing the large number of e^+e^- and $\mu^+\mu^-$ pairs from Z boson decays. The invariant dilepton mass is required to be close to the Z boson mass, $60\,\text{GeV} < < 120\,\text{GeV}$. A small dependency on the lepton p_T was already observed in the past. With the full statistics of 2016, it became necessary to parameterize this dependency in order to (partially) correct for this effect. The following parameterization as a function of the p_T of the second lepton was chosen:

$$r_{\mu/e} = a + \frac{b}{p_T}$$

Here a and b are constants that are determined in a fit to data. The fit for this parameterization is shown in the upper left plot of Fig. 6. It can be seen that the efficiency for muons is higher than for electrons, especially at low lepton p_T. Consistent results are observed in the simulation. The determined parameters are stated in Tab. 9.

As a closure test, each dielectron event is weighted by $r^2_{\mu/e}$ (one has to square to correct each of the electrons to a "muon efficiency level") and a new ratio $r^{corr.}_{\mu/e}$ is calculated by dividing the number of dimuon events by the number of corrected dielectron events. Per definition, $r^{corr.}_{\mu/e}$ is expected to be close to 1 and to correct the trend in the p_T of the second lepton.

Other trends in observables correlated to the dilepton system are reduced as can be observed in Fig. 6 for the invariant dilepton mass. In case of the p_T of the leading lepton the trend is reduced but some effect remains. Since the effect is mainly at very low leading lepton p_T and less than 5% of the events fall into this category, we chose to use a flat systematic uncertainty of 10% to cover this remaining trend instead of doing a mutli-variable fit. An uncertainty band indicates these 10% in both the plots for $r^{corr.}_{\mu/e}$ and the uncorrected plots for and the leading lepton p_T in Fig. 6. Further dependencies of $r^{corr.}_{\mu/e}$ on important observables are studied in Fig. 7. The chosen 10% systematic uncertainty is sufficient to cover any remaining trends in these observables.

Table 9: Result of the fit of as a function of the p_T of the trailing lepton in the Drell–Yan control region. The same quantaties derived from simulation are shown for comparison. Only statistical uncertainties are given.

	a	b
Data	1.140±0.005	5.20±0.16
MC	1.162±0.011	5.15±0.36

As the measurement of is performed in a region differing from the signal selection, especially in E_T^{miss}, the extrapolation in the signal region is evaluated by studying the dependency of $0.5(r^{corr.}_{\mu/e} + 1/r^{corr.}_{\mu/e})$ on several important event properties using the parameterization introduced above. In Fig. 8 the results of these studies can be observed. Shown are the results on data in black and simulation in green. The dashed line illustrates the central value observed on data. To determine the systematic uncertainty the fit parameters a and b are varied by its statistical uncertainty and the full prediction is shifted up and down by the 10% systematic uncertainty from the studies above. The relative change of the mean value is used as the systematic uncertainty of the method. The quantity $0.5(r^{corr.}_{\mu/e} + 1/r^{corr.}_{\mu/e})$ is especially stable with respect to , E_T^{miss}, and , validating the extrapolation from the Drell–Yan control region into the signal region.

Measurement of

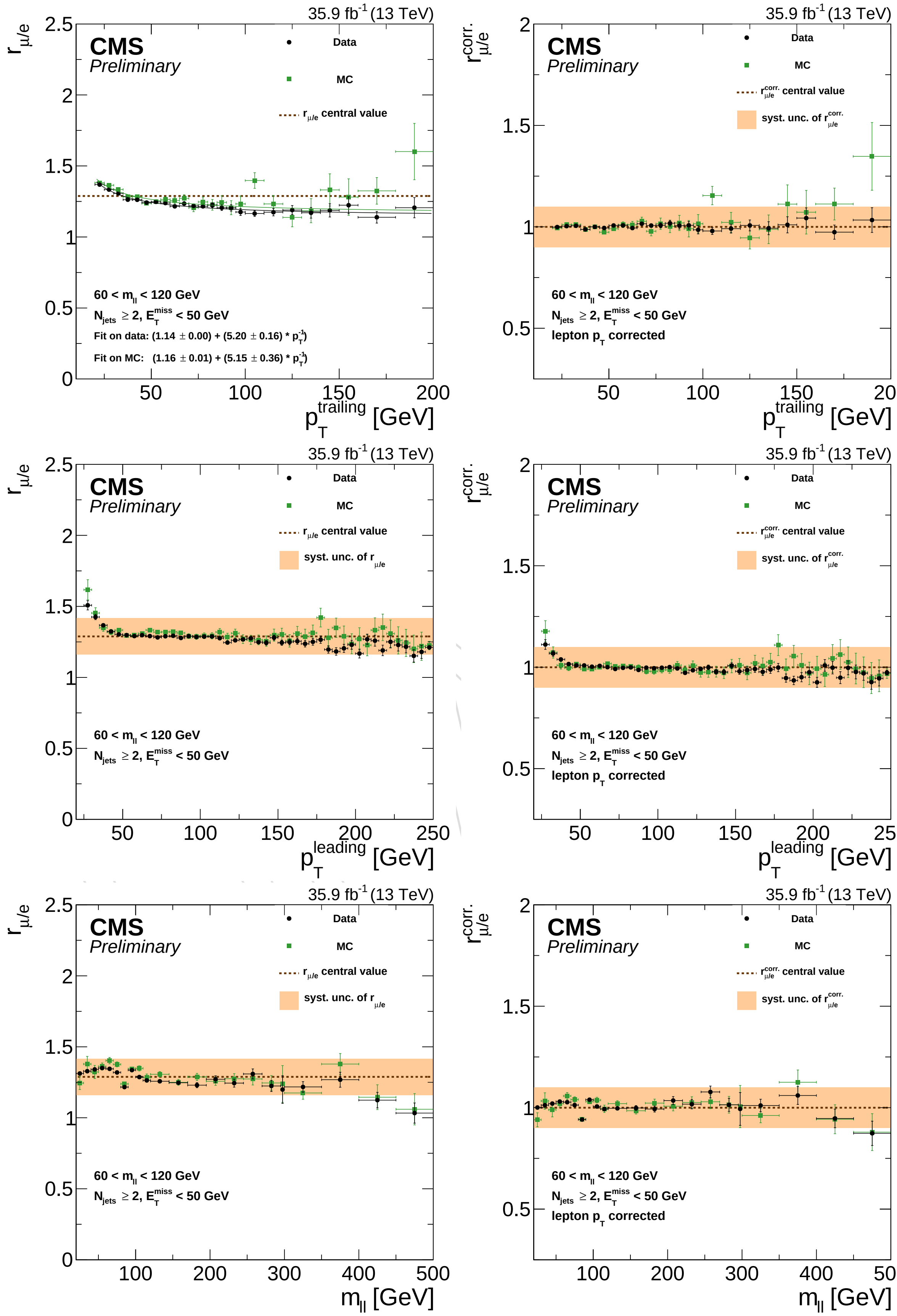

Figure 6: $r_{\mu/e}$ dependency on the p_T of the first (center) and second lepton (top), and the invariant dilepton mass (bottom) for data and MC. The left (right) plots show the values for before (after) the parameterization on the second lepton p_T is propagated to the dielectron events. The central value in the left plots indicates the value that would be obtained without the parameterization. The fit values of the parameterization are shown in the top left plot.

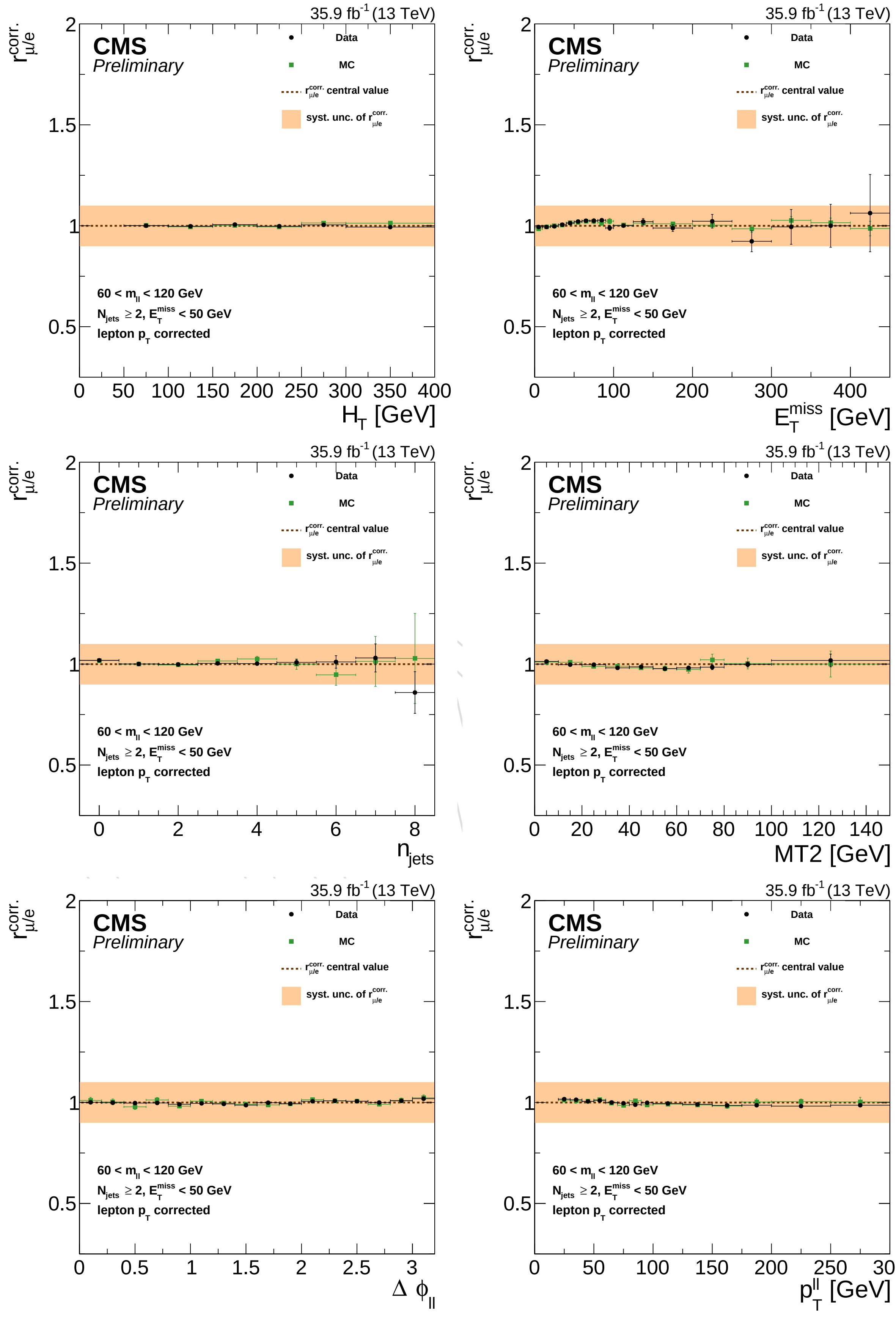

Figure 7: $r^{corr.}_{\mu/e}$ dependency on H_T (top left), E_T^{miss} (top right), jet count (left center), (right center), $\Delta\phi$ between the leptons (bottom left), and p_T of the dilepton system (bottom right) for data and MC after the parameterization on the second lepton p_T is propagated to the dielectron events. The systematic uncertainty of 10% is indicated by the orange band.

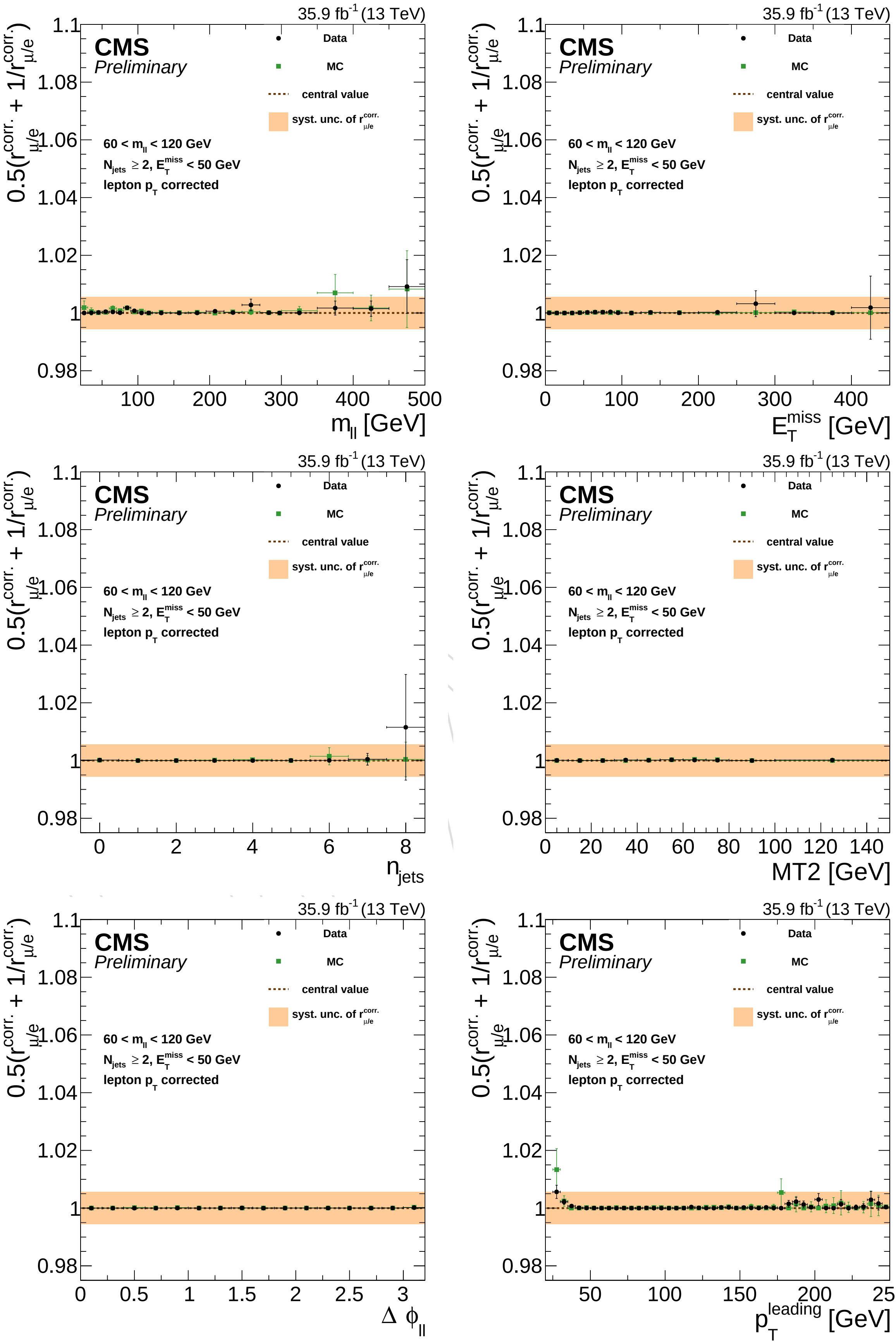

Figure 8: $0.5(r^{corr.}_{\mu/e} + 1/r^{corr.}_{\mu/e})$ dependency on the invariant mass of lepton-pair(top left), E_T^{miss} (top right), jet count (left center), (right center), $\Delta\phi$ between the leptons (bottom left), and second lepton (bottom right) for data and MC after the parameterization on the second lepton p_T is propagated to the dielectron events. The uncertainty introduced by shifting the fit parameters by its statistical uncertainty and the full prediction by 10% is indicated by the orange band.

Trigger efficiencies are measured using a lepton unbiased control sample of dilepton events, collected with Particle Flow HT triggers with thresholds between 125 GeV and 900 GeV. The efficiency is calculated as the fraction of events in this sample that also passes the dilepton triggers stated in Tab. 3 for the given flavor combination:

$$\epsilon_{trigger} = \frac{\text{Lepton pair } \cap PFH_T \text{ trigger } \cap \text{ Dilepton trigger}}{\text{Lepton pair } \cap PFH_T \text{ trigger}}. \tag{5}$$

No minimum values of or $E_{\mathrm{T}}^{\mathrm{miss}}$ are applied, but all events with ≥ 2 and $E_{\mathrm{T}}^{\mathrm{miss}} > 100\,\mathrm{GeV}$ are vetoed to exclude the signal region and ensure the orthogonality of the factorization method and the direct measurement of in the control region. As a further requirement, a minimum H_{T} value of 200 GeV is required to keep the PFHT triggers efficient.

The resulting trigger efficiencies measured in data are shown in Tab. 10. The trigger efficiencies on MC are given for comparison. No HT cross triggers are required on MC, thus the number of events is much larger. The observed efficiencies are about 96% for $\mathrm{e}^+\mathrm{e}^-$, 95% for $\mu^+\mu^-$ and 91% for . This leads to a value for of 1.052. The efficiencies for $\mu^+\mu^-$ and on MC are 2-3% higher, but =1.045 is close to the value on data. We assign a systematic uncertainty of 3% to each trigger efficiency, which is the maximal deviation between the efficiencies in data and MC. Error propagation of the uncertainties on the individual efficiencies to results in about 4% uncertainty on . The dependencies of on different observables are show in Fig. 9. No significant dependency of on any event property is observed and the chosen systematic uncertainty is found to be sufficient to cover fluctuations on data and small remaining trends on MC (and p_{T} of the dilepton system).

Table 10: Trigger efficiency values for data and MC with OS, $p_T > 25(20)$ GeV and $H_T > 200$ GeV.

	Data			MC		
	nominator	denominator	$\epsilon_{trigger} \pm \sigma_{stat}$	nominator	denominator	$\epsilon_{trigger} \pm \sigma_{stat}$
ee	12070	12584	0.959±0.002	111787	116654	0.958±0.001
$\mu\mu$	8741	9230	0.947±0.002	190067	194687	0.976±0.001
eμ	2437	2690	0.906±0.006	43069	46520	0.926±0.000
R_T	1.052±0.043			1.045±0.041		

4.1.3 Combination of the two methods

Due to the parameterization of the factorization method has to be aplied on an event-to-event basis and no constant result for can be given. Instead, the factorization method is applied in each signal region. The obtained prediction is divided by the number of OF events to get an factor for the factorization method in this region. This factor is combined with from the control region method by using the weighted average.

The resulting background estimates for flavor-symmetric backgrounds in the signal region of the edge search are summarized in Tab. 11. It can be observed that the event-by-event reweighting in the factorization method yields smaller values for higher mass bins (especially in the $\mathrm{t\bar{t}}$ like selection). This makes sense since is correlated to the p_{T} of the leptons and higher masses usually correspond to higher lepton p_{T} and thus smaller reweighting factors (see Fig. 6). Overall, the factors from the factorization method are a bit smaller than the factor from the control region method but still agree within their uncertainties.

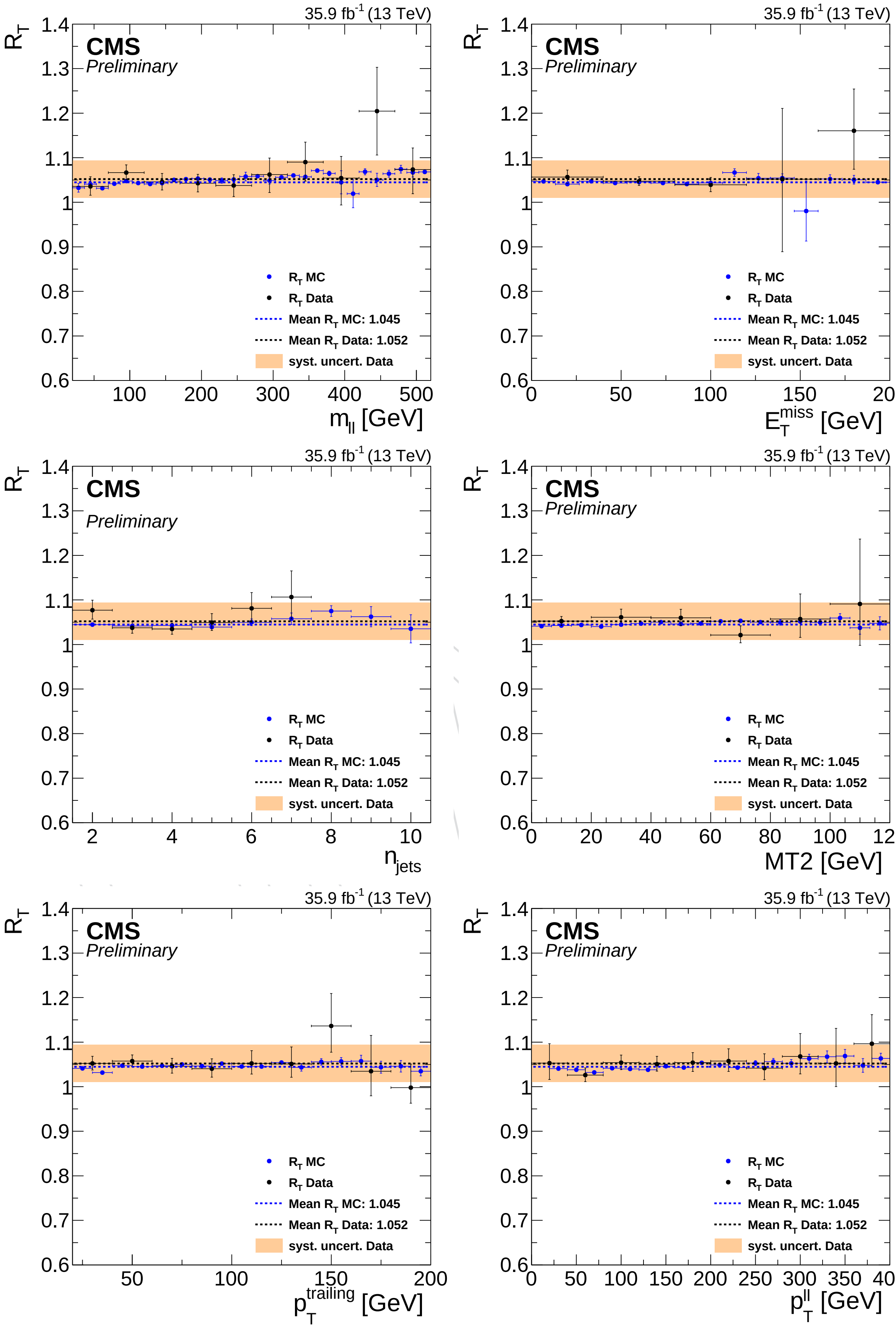

Figure 9: Dependency of SF/OF trigger efficiency ratio on the invariant mass of lepton-pair(top left), E_T^{miss} (top right), jet count (left center), (right center), p_T of the second lepton (bottom left) and p_T of the dilepton system (bottom right) for data and MC. The assigned systematic uncertainty of about 4% on is indicated by the orange band.

Table 11: Resulting estimates for flavour-symmetric backgrounds. Given is the observed event yield in events, the estimate in the SF channel using the event-by-event reweighting of the factorization method, $R_{SF/OF}$ for the factorization method, $R_{SF/OF}$ when combining this value with the constant $R_{SF/OF}$ from direct measurement, and the combined final prediction. Statistical and systematic uncertainties are given separately.

mass range [GeV]	OF events	pred. fact. method	$R_{SF/OF}$ fact. method	comb. $R_{SF/OF}$	pred.
ttbar like					
20-60	264	$289.1^{+18.3}_{-17.3}\pm14.2$	1.10 ± 0.05	1.10 ± 0.04	$290.9^{+18.5}_{-17.4}\pm9.3$
60-86	164	$179.1^{+14.5}_{-13.4}\pm8.7$	1.09 ± 0.05	1.10 ± 0.03	$180.5^{+14.7}_{-13.6}\pm5.7$
96-150	160	$173.5^{+14.3}_{-13.2}\pm8.2$	1.08 ± 0.05	1.10 ± 0.03	$175.5^{+14.4}_{-13.3}\pm5.5$
150-200	67	$72.4^{+10.0}_{-8.8}\pm3.3$	1.08 ± 0.05	1.09 ± 0.03	$73.3^{+10.1}_{-8.9}\pm2.3$
200-300	43	$46.1^{+8.2}_{-7.0}\pm2.1$	1.07 ± 0.05	1.09 ± 0.03	$46.9^{+8.3}_{-7.1}\pm1.4$
300-400	17	$18.2^{+5.6}_{-4.4}\pm0.8$	1.07 ± 0.05	1.09 ± 0.03	$18.5^{+5.7}_{-4.4}\pm0.6$
>400	4	$4.3^{+3.4}_{-2.0}\pm0.2$	1.07 ± 0.05	1.09 ± 0.03	$4.3^{+3.4}_{-2.1}\pm0.1$
non ttbar like					
20-60	3	$3.2^{+3.1}_{-1.8}\pm0.1$	1.07 ± 0.05	1.09 ± 0.03	$3.3^{+3.2}_{-1.8}\pm0.1$
60-86	3	$3.2^{+3.1}_{-1.7}\pm0.1$	1.07 ± 0.05	1.09 ± 0.03	$3.3^{+3.2}_{-1.8}\pm0.1$
96-150	6	$6.5^{+3.9}_{-2.6}\pm0.3$	1.08 ± 0.05	1.09 ± 0.03	$6.6^{+3.9}_{-2.6}\pm0.2$
150-200	5	$5.4^{+3.6}_{-2.3}\pm0.2$	1.08 ± 0.05	1.09 ± 0.03	$5.5^{+3.7}_{-2.4}\pm0.2$
200-300	3	$3.2^{+3.1}_{-1.7}\pm0.1$	1.07 ± 0.05	1.09 ± 0.03	$3.3^{+3.2}_{-1.8}\pm0.1$
300-400	3	$3.2^{+3.1}_{-1.7}\pm0.1$	1.07 ± 0.05	1.09 ± 0.03	$3.3^{+3.2}_{-1.8}\pm0.1$
>400	1	$1.1^{+2.4}_{-0.9}\pm0.0$	1.06 ± 0.05	1.09 ± 0.03	$1.1^{+2.5}_{-0.9}\pm0.0$
ICHEP legacy region					
>101	564	$609.9^{+26.2}_{-25.1}\pm27.6$	1.08 ± 0.05	1.09 ± 0.03	$617.6^{+26.6}_{-25.5}\pm19.0$
8 TeV legacy region					
20-70	5393	$5842.1^{+80.1}_{-79.0}\pm274.3$	1.08 ± 0.05	1.09 ± 0.03	$5867.4^{+80.4}_{-79.4}\pm185.4$

As validation of these background estimates, the observed data in the OF channel is compared to SM simulation and a closure test on flavor-symmetric MC is displayed in Fig. 10. Decent agreement between data and simulation and a good closure is observed.

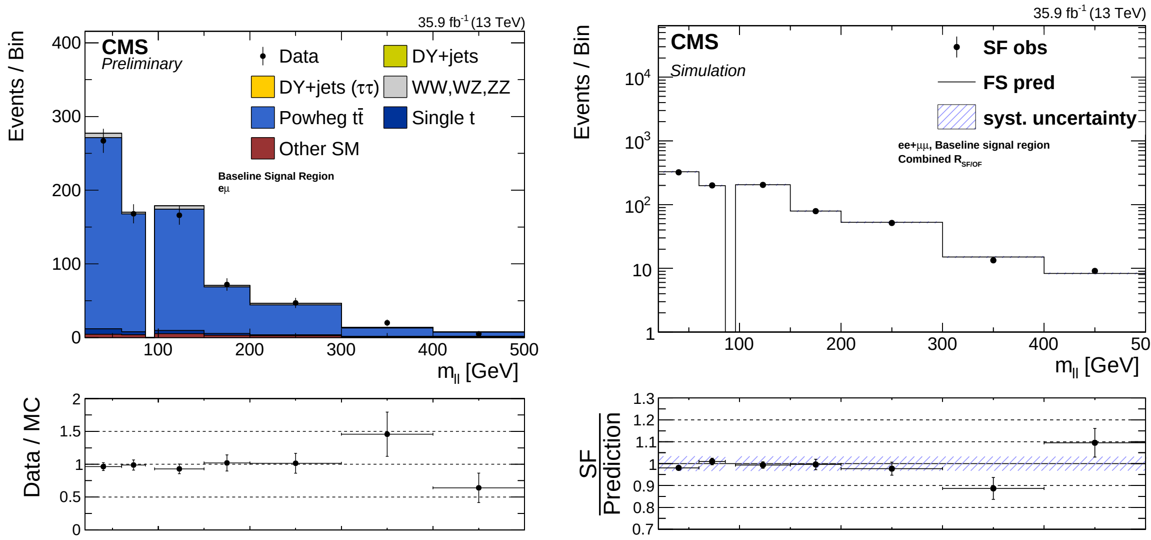

Figure 10: Left: Data/MC comparison in the edge signal region for OF events. The data is shown as black points while the backgrounds are shown as a stacked histogram. Below the plot, the data/MC ratio is shown as black points.
Right: Closure plot for the flavor-symmetric background prediction. SF MC is shown as black dots while the prediction from the OF MC · is shown as a black line and the systematic uncertainty as a shaded blue band.

4.2 Flavor-symmetric background prediction for the electroweak search regions

As is clear from the discussion in the last section, the underlying methodology of the flavor symmetric background prediction method is to measure a yield in an opposite-flavor control region, multiplying this yield by an OF-SF correction factor and thereby obtaining an estimate in the SF region. While this method is clearly simple and clean, its main pitfall is the limited statistical power in scarcely populated kinematic regions. This is to say, opposite-flavor and same-flavor regions are populated equally, and therefore if expected background levels are of the order of single events or less, this method suffers from large statstical uncertainties (in the extreme case of an empty OF control region, the central value of the prediction will be zero with infinite relative statistical error). In simplified terms, the prediction method can be written as:

$$N_{SF} = N_{OF} \cdot R_{SF/OF} \tag{6}$$

Since the guiding principle of the electroweak search regions is to suppres the tt̄ process to very low yields with a cut on this necessitates a slightly adapted method of predicting this background. The electroweak search regions have, however, a feature which can be exploited in the estimation of the tt̄ background, namely that the invariant mass of the SF di-lepton pair is required to be on-Z. This gives a lever arm to extend the OF control region from which the SF prediction can be deduced. This consideration allows us to extend the (form $86 < \; < 96$ GeV to > 20 GeV)window from which the estimation is taken by a large fraction. By implementing this approach in extending the OF control region, the simplified formula from before then becomes

$$N_{SF} = N_{OF}^{ext.mll} \cdot r_{SFOF} \cdot f_{mll}, \tag{7}$$

where is the ratio of OF events in the on-Z region over the number of events in the extended . While can be assumed to be the same number as for the strong (“edge”) search, the factor have to be measured. A detailed description of the method is provided in reference [**?**]. The measured value is $= 0.065 \pm 0.02$.

4.2.1 Closure test and MC-data comparison of the $t\bar{t}$ prediction in EWK searches

In order to test the feasibility and precision of the extended FS background prediction for the electroweak search regions, a closure test is performed on MC simulation by comparing the “observed” $t\bar{t}$ yields in the search region with the MC predicted values by multiplying the yields in the extended mass range yields by MC values for κ and . These two observations can also be compared to the expected data-yields which are obtained by replacing the MC yields for $N_{OF}^{ext.mll}$ in Eq. 7 by the data yield in this same kinematic region.

A full plot of the $t\bar{t}$ MC observation and prediction in the TChiWZ/TChiZZ and the TChiZH signal regions can be seen in Fig. 11. Since no significant trend is seen in the ratio, the corrected and non-corrected markers coincide. Closure of this method on MC simulation is good.

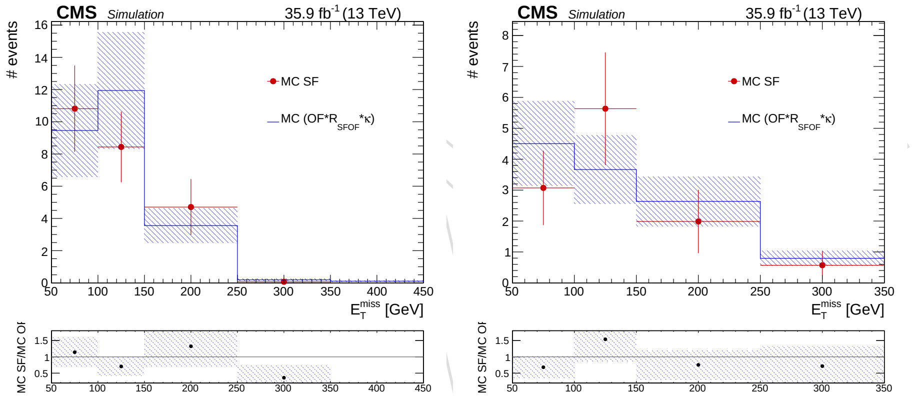

Figure 11: Closure test of the flavour symmetric prediction method for electroweak searches for 35.9 . The spectrum is shown since this is the variable in which the search region is binned.

Predicted values for the flavour symmetric yields in the spectrum agree reasonably for the signal region (≥ 100 GeV) and the systematic uncertainty assigned to the κ method of 30 % covers any discrepancies.

4.3 WZ, ZZ and $t\bar{t}Z$ validation for the electroweak searches

The electroweak search models and search regions are similar to the leptonic decay final states of the WZ, ZZ, $t\bar{t}Z$ processes. Because these backgrounds are taken from MC simulation it is necessary to validate the proper modeling of the leptonic distributions in the simulation by comparing them to control regions in data. For the regions which disclose a data/MC disagreement scale factors are derived. For this validation exercise, the veto on additional leptons are inverted and a three-lepton and a four-lepton control sample are considered, where the additional leptons are required to pass looser isolation and a p_T cut of 20 GeV. The control regions are constucted to isolate the specific process considered while still keeping many of the analysis baseline selections such as requiring at least two jets and the $|\Delta\phi(\text{jet}_{1,2}, MET)| > 0.4$.

For the validation of the WZ background, the three-lepton sample is considered with a moderate requirement on of less than 60 GeV. This sample is chosen to be inclusive in the lepton flavors and number of jet composition, although a veto on b-tagged jets with p_{T} greater than 25 GeV is applied.

Similarly, for the validation of the ZZ background component, the four-lepton sample is considered with no extra requirements on anything so as to improve the statistical power of this sample as much as possible.

For the validation of the $t\bar{t}Z$ background, a three-lepton sample is considered just as for the WZ background, but now with a requirement on the number of b-tagged jets to be exactly two and the $>$ 30 GeV. For both the ZZ and $t\bar{t}Z$ control regions, the where the scale factor is extracted from is made with the leptons having an invariant mass closest to the Z boson mass. For the ZZ region, a cut on $>$ 20 GeV for the second lepton pair to reduce contributions from low mass resonances. The simulated MC yield is then compared to the observed yields, as shown in Fig. 12 for 35.9 . The simulated MC yield is then compared to the observed yields, as shown in Fig. 12 for 35.9 . In the WZ control region, we believe the first bin represents a fluctuation since we have not observed this excess in any other region (for example inclusive in or jets). In addition the region of low is not used in the analysis.

Table 12 compares the yields obtained from these figures and shows almost perfect agreement in the WZ sample, where 116 signal (WZ) events are expected and 123 events are observed in data after subtracting the remaining MC backgrounds. We assign a conservative 30 % uncertainty to the MC-driven WZ estimation in the signal regions to cover for any remaining differences in the 2-lepton sample compared to the 3-lepton sample.

Agreement for the ZZ process is slightly inferior, 7.6 expected events are to be compared to 13 events observed in the data after subtracting the remaining MC backgrounds. Since this difference could potentially lead to an excess in the relevant on-Z signal region, it is translated into a scale-factor for the MC-driven ZZ background in the electroweak signal regions. This scale factor is therefore given by the ratio of data minus the remaining backgrounds over the expected ZZ signal which is 1.71. We assign an additional 50 % uncertainty to the final ZZ background to cover for any remaining differences in the kinematics.

The agreement for the $t\bar{t}Z$ in the constructed control region is inferior as well, comparing the 20 expected signal $t\bar{t}Z$ events to the observed 27.5 events after subtraction of the remaining MC backgrounds. This translates into a scale factor of 1.36 with a conservative 30 % uncertainty.

Table 12: 3-lepton, 4-lepton and $t\bar{t}Z$ control regions. Signal MC is $WZ \rightarrow 3l\nu$ in the 3-lepton region, $ZZ \rightarrow 4l$ in the 4-lepton region and $t\bar{t}Z \rightarrow 2l2\nu$ in the $t\bar{t}Z$ region

	3-lepton region	4-lepton region	ttZ region
signal MC	116.00 ± 3.23	7.66 ± 0.24	20.16 ± 0.37
bkg. MC	40.65 ± 2.86	1.90 ± 0.18	8.53 ± 1.05
data	**164**	**15**	**36**
data-bkg.	123.35 ± 13.12	13.10 ± 3.88	27.47 ± 6.09
(data-bkg.)/sig.	1.06 ± 0.12	1.71 ± 0.51	1.36 ± 0.30

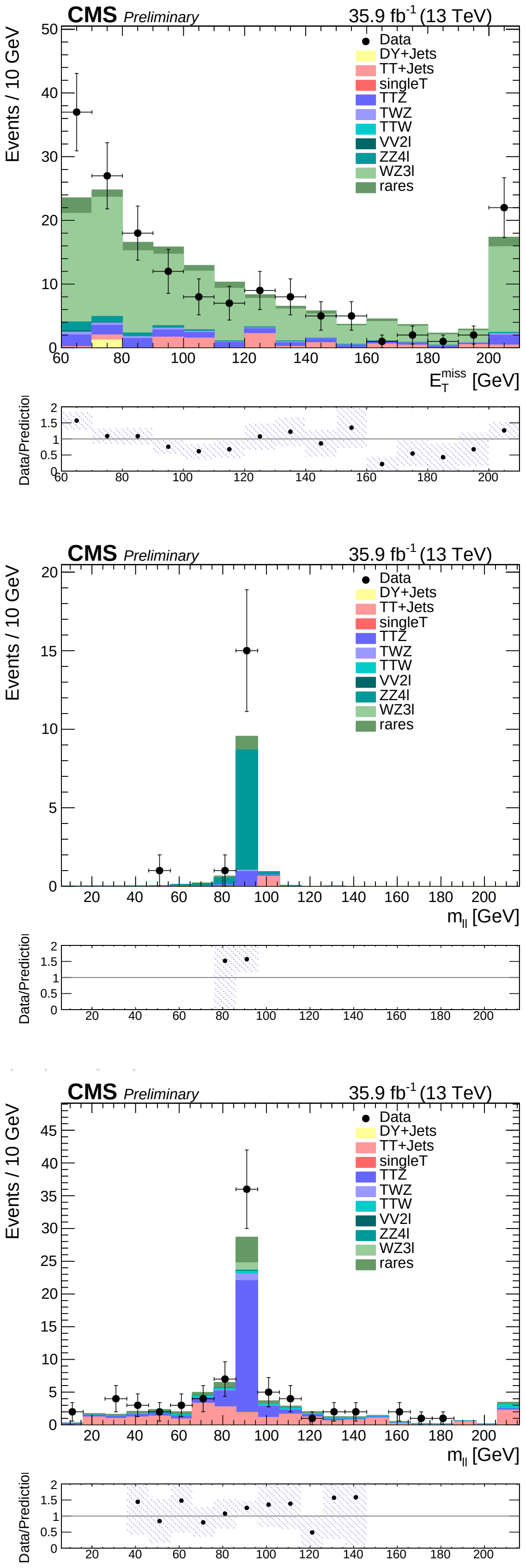

Figure 12: Distributions of in the 3-lepton (WZ) control region (left), in the 4-lepton (ZZ) control region (middle) and in the $t\bar{t}Z$ control region.

4.4 Drell-Yan like Background

DY-type backgrounds on the Z peak are estimated using the - templates method. This methods is described in a separate note (AN-16-468).

4.4.1 Prediction of DY contribution in off-Z signal regions -

Contributions of the DY spectrum with purely instrumental to the off-Z searches for the edge are expected to be small in comparison to the contributions of $\mathrm{t}\bar{\mathrm{t}}$, other flavor-symmetric backgrounds or rare Z+ν processes (which are taken from MC). The prediction of the events containing a Z and purely instrumental is done with the MET-template method (see AN-16-468) and can only be performed on the Z peak. Although the contribution is small, it is important to make a prediction also for the regions outside of the Z-window of 86-96 GeV. This is accomplished with a simple translation factor named which is measured in a DY dominated control region (at least 2 jets, $<$ 50 GeV and $>$ 80 GeV). The $>$ 80 GeV requirement is removed for the two edge legacy regions. is defined as the ratio of SF DY events in the range of the signal region outside the Z-peak divided by the SF events inside the Z-window. In order to even further purify the DY distribution, in the control region where is measured, the OF contribution in this region is subtracted from the SF contribution, therefore subtracting the $\mathrm{t}\bar{\mathrm{t}}$ contamination (and other FS background contributions) to the measurement of .

The measured values of for the regions in from data and MC are shown in Table 13. A systematic uncertainty of 25% is assumed from dependency studies for the edge and ICHEP legacy regions (Fig. 13). Trends are covered within this uncertainty except for a dependency on (which is not used in these regions). This is not suprising since the cut changes the distribution. This feature lead to the inclusion of an $>$ 80 GeV cut in the main control regions. This cut reduces the available statistics drastically and makes further dependency studies impossible. To account for the reduced statistics we an uncertainty of 50% is used for bins below 150 GeV where still several 100 events are left. In the bins above 150 GeV the statistics is even smaller (20-70 events) which results in very small factors and 100% systematic uncertainty is assigned in these bins.

The assigned systematic uncertainties dominate the total uncertainty of . Note that is only applied to the MET-template prediction which is the smallest background contribution in all edge signal bins.

4.5 Likelihood discriminator for $\mathrm{t}\bar{\mathrm{t}}$ events

#Xevents

Since the strong edge search in the low-, and high-mass regions features mainly $\mathrm{t}\bar{\mathrm{t}}$ as a SM background, it is of considerable interest to exploit this fact. The $\mathrm{t}\bar{\mathrm{t}}$ process is very distinct in its reconstructed objects and their kinematic distributions. Therefore, a likelihood discriminator was developed to classify the backgrounds in two region: $\mathrm{t}\bar{\mathrm{t}}$-like and non-$\mathrm{t}\bar{\mathrm{t}}$-like.

The probability density functions of four characteristic variables in $\mathrm{t}\bar{\mathrm{t}}$ are derived from data and MC for these variables:

1. the
2. the di-lepton system p_{T} (denoted as Z-p_{T} at times)
3. the — — between the leptons
4. a variable named , defined just below.

Table 13: Measured values for for data and MC in the different signal regions of the off-Z analysis. The uncertainty is dominated by the assigned systematic uncertainty.

	Data		MC	
	N_{in} 4295±65		N_{in} 3954±62	
mass range [GeV]	N_{out}	$R_{out/in}$	N_{out}	$R_{out/in}$
20-60	229±15	0.053±0.027	138±12	0.035±0.018
60-86	551±23	0.128±0.064	453±21	0.115±0.058
96-150	671±26	0.156±0.078	644±25	0.163±0.082
150-200	74±9	0.017±0.017	55±8	0.014±0.014
200-300	52±9	0.012±0.012	51±8	0.013±0.013
300-400	22±5	0.005±0.005	19±5	0.005±0.005
>400	23±5	0.006±0.006	27±5	0.007±0.007
No MT2 cut				
	N_{in} 591072±782		N_{in} 517874±732	
20-70	48043±554	0.081±0.020	39969±504	0.077±0.019
>101	43186±811	0.073±0.018	35776±773	0.069±0.017

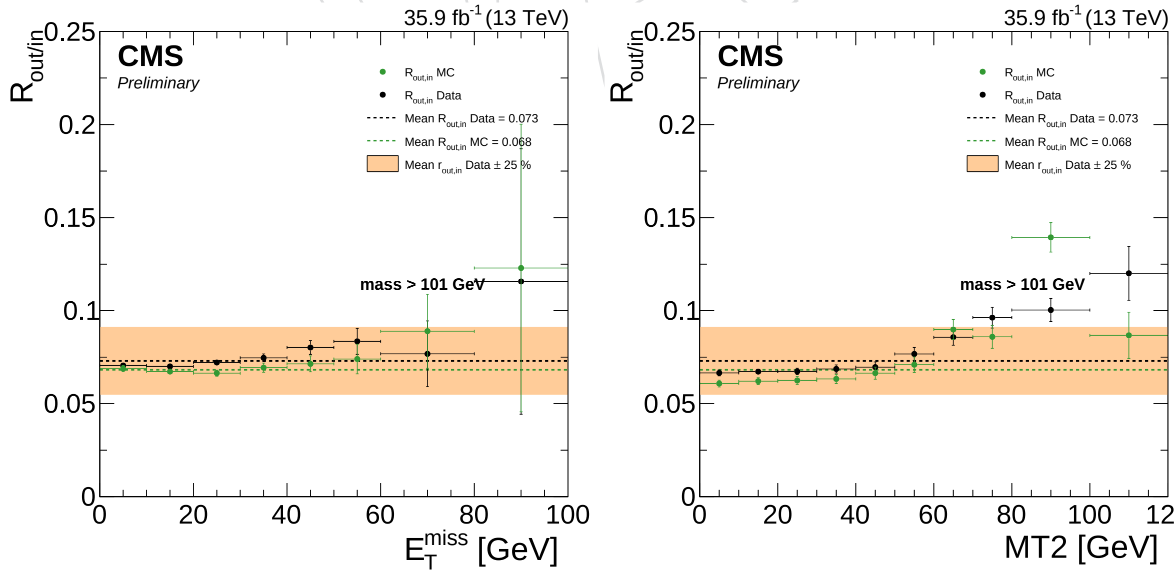

Figure 13: (left) and (right) dependency of in the mass bin from the ICHEP legacy region (> 101 GeV).

To calculate , all combinations of leptons and jets are selected and the minimum is found. This process is repeated for the remaining lepton and jets and the two minimized systems are then summed to give . If b-tagged jets are present, they are given priority in the calculation of both lepton-jet systems. I.e. if one or two (or more) b-jets are present, between the leptons and the b-jets is minimized first, and then the remaining (b-)jets are considered for the minimization of the second lepton's .

To calculate this likelihood the probability density functions of the four observables are determined by maximum likelihood fits in the opposite-flavor control sample in the same kinematic region as the same-flavor signal region. The respective fit functions for the variables are a sum of two exponentials for the , a second-order polynomial for the $|\Delta(\phi)|$, and a Crystal-Ball function for both the di-lepton p_T as well as the .

These four pdfs can be seen in Fig. 14 where fits are shown together with the data.

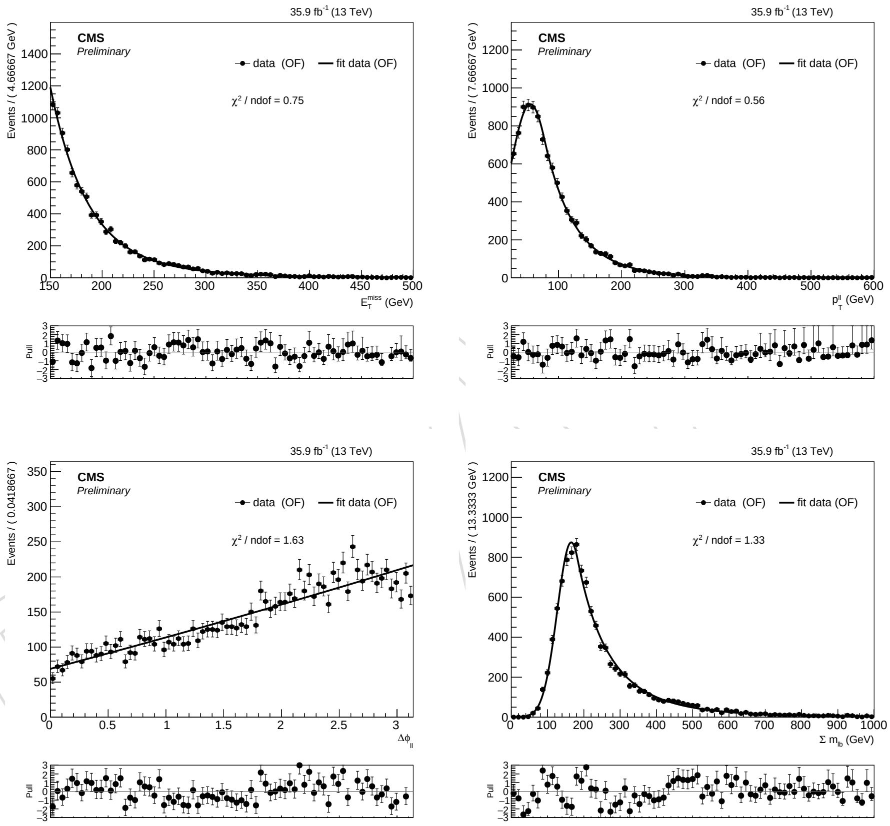

Figure 14: PDFs for the four input variables to the likelihood discriminant: (top left), di-lepton p_T (top right), || between the leptons (bottom left), and (bottom right).

The final pdfs that are used to construct the likelihood variable are taken from the data-OF sample.

To demonstrate the discrimination power of the input variables, Fig. 15 shows the distributions of the input variables for the likelihood function together with the fitted functions from the OF data and some example signal points from the T6bbslepton model ($\rightarrow$ b+$\rightarrow$ $\ell\ell$). Several things are shown in Fig. 15: data observations in the OF sample in black markers, $t\bar{t}$ MC (OF in dark blue markers and SF in light blue markers), as well as the pdf-fits from data (black line). The ratio of the analytic pdf to OF data and SF $t\bar{t}$ is displayed in the lower part of each plot. Also shown are some example signal points in colored markers, demonstrating separation in all of the variables.

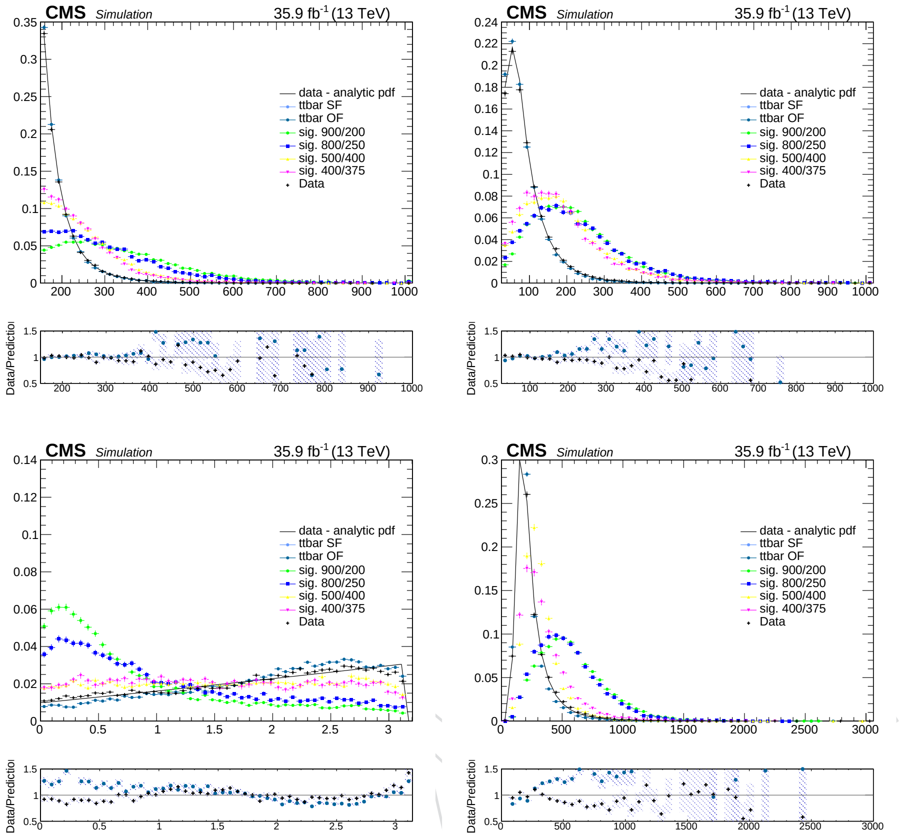

Figure 15: Distributions of OF data (black markers), $t\bar{t}$ (OF in dark blue markers and SF in light blue markers) overlaid with the pdf-fits from data (black line). Also shown are example signal points from the T6bbslepton model (colored markers). The distributions are for $E_{\mathrm{T}}^{\mathrm{miss}}$ (top left), di-lepton p_{T} (top right), lepton-delta-phi (bottom left), and sum of mlbs (bottom right). The ratio of the analytic pdfs to OF data and SF $t\bar{t}$ MC are shown in the lower part of each plot.

For each event passing the baseline signal region in the SF channel, a likelihood function is constructed by multiplying the evaluation of each of the pdfs. The negative logarithm is then defined as the likelihood discriminant and denoted by . Its distribution in $t\bar{t}$ MC is shown in Fig. 16 for an expected luminosity of 10 in the SF and OF samples (a closure test, essentially). One can see that the OF and SF samples in agree very well in the MC simulation, giving confidence in the derivation and application of the method.

The working point of $t\bar{t}$-like versus non-$t\bar{t}$-like is chosen at an efficiency corresponding to roughly 95%, which relates to a value of of 21.

To estimate any remaining difference in the likelihood discriminator between a pure $t\bar{t}$ sample and actual data-observation, Fig. 17 shows the cumulative distribution similar to Fig. 16, but for again a combination of data, $t\bar{t}$ (SF and OF), and the same example signal points as before. The black line is constructed by sampling the analytic pdfs from the fitted functions independently from each other 250k times, therefore ignoring any correlation between the variables in data. Comparison between the black markers (data) and the dark blue and light blue markers ($t\bar{t}$ OF

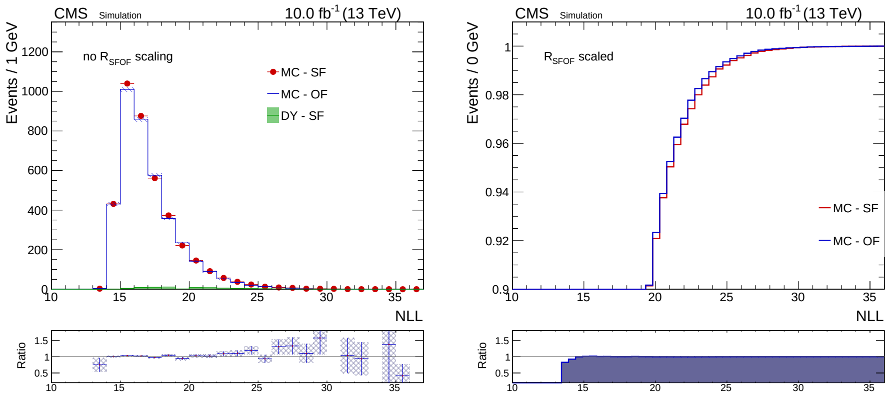

Figure 16: distribution in the SF and OF channel, before any reweighting of the OF sample (left). The cumulative distribution of the left plot scaled with is shown on the right.

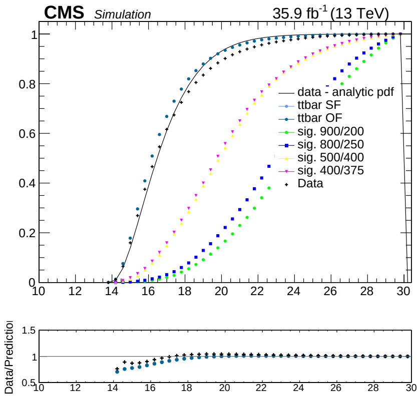

Figure 17: distribution comparison in the OF data (black markers) and MC simulation for $t\bar{t}$ (OF dark blue and SF light blue markers) as well as example signal models (colored markers). The black line is obtained by sampling the analytic pdfs from Fig. 14 independently 250k times. In the lower part the ratio of the analytic pdf to OF data and SF and OF $t\bar{t}$ is displayed

and SF, respectively[4]) therefore gives a sense of how big of an effect the correlations between the variables make in the likelihood discriminator. At a cut-value of 21, these differences are of the order of 1%. It is to be noted that while this proves the relative non-correlation between the variables, it is not very important for the final selection since the correlations in the data are expected to be well reproduced by the MC simulation, since all the input variables use (to a very good first order) matrix-element quantities such as the object-p_{T}'s and angular correlations. Fig. 17 additionally shows the ratio of the analytic pdf to OF data and SF and OF $\mathrm{t\bar{t}}$ MC.

---

[4] The two colors are hard to distinguish because they almost perfectly coincide

In this section we describe the techniques used to estimate the SM backgrounds in our signal regions. The SM backgrounds fall into three categories:

- **Z+jets**: this is the dominant background after the preselection. The $E_{\mathrm{T}}^{\mathrm{miss}}$ in events comes from jet mismeasurement, as there are no prompt neutrinos, and tends to fall steeply. The contribution to the signal regions estimated with the "$E_{\mathrm{T}}^{\mathrm{miss}}$ template" technique described in Sec. 4.6. This technique is an extension of the $E_{\mathrm{T}}^{\mathrm{miss}}$ template technique used in previous searches listed in section **??**.
- **Flavor-symmetric (FS) backgrounds**: this category includes processes which produce 2 leptons of uncorrelated flavor. The $E_{\mathrm{T}}^{\mathrm{miss}}$ comes from prompt neutrinos and thus this background can be sizeable in the $E_{\mathrm{T}}^{\mathrm{miss}}$ tail regions. It is dominated by $\mathrm{t\bar{t}}$ but also contains $\mathrm{Z}\rightarrow\tau\tau$, WW, and single top processes. The FS background is estimated using a data control sample of $\mathrm{e}\mu$ events as described in Sec. 4.7. This is the exact same method used in previous searches listed in section **??**.
- **Rare processes with Z+ν**: these backgrounds contain a leptonically decaying Z boson and also at least one prompt neutrino, from the decay of W or Z bosons. The methods above do not estimate this contribution, so we instead estimate it from simulation. We validate the MC modeling of the WZ, ZZ, and processes using data control samples with exactly 3 leptons and 0 b-tags (WZ control sample), exactly 3 leptons and $\geq$ 2 (control sample), or exactly 4 leptons (ZZ control sample). The results from this study are described in section 4.8.

4.6 Estimating the Background with $E_{\mathrm{T}}^{\mathrm{miss}}$ Template

Variations of this technique were used extensively in various run I analyses, listed in section **??**. In this section, we describe the general method used to obtain the estimate.

The premise of this data-driven technique is that $E_{\mathrm{T}}^{\mathrm{miss}}$ in events is predominantly produced by the hadronic recoil system and *not* by the leptons making up the Z. Therefore, the main idea of the $E_{\mathrm{T}}^{\mathrm{miss}}$ template method is to measure the $E_{\mathrm{T}}^{\mathrm{miss}}$ distribution in a control sample where the majority of the $E_{\mathrm{T}}^{\mathrm{miss}}$ comes from the hadronic recoil system and has the same general attributes regarding fake $E_{\mathrm{T}}^{\mathrm{miss}}$ as in events. We thus use a sample of events, since both and events consist of a well-measured object recoiling against hadronic jets. Our search region includes regions with at least 1 b-tagged jet, so we expect to have some real $E_{\mathrm{T}}^{\mathrm{miss}}$ in the background coming from semi-leptonic heavy flavor decay. This will still be accounted for using the $E_{\mathrm{T}}^{\mathrm{miss}}$ template method, because the same real $E_{\mathrm{T}}^{\mathrm{miss}}$ will be present in the sample when using the same b-tag requirement.

For selecting photon-like objects, the selection described in Sec. **??** is used. It is not essential to this method that our control sample gives a high-purity of photons. For our purposes, selecting jets with predominantly electromagnetic energy deposition in a good fiducial volume suffices to ensure that the photon-like object is well-measured and does not contribute to fake $E_{\mathrm{T}}^{\mathrm{miss}}$. The events are selected with a suite of single photon triggers with p_{T} thresholds varying from 22–165 GeV. The events are weighted by the trigger prescale such that events evenly sample the conditions over the full period of data taking.

For each of the signal regions listed in Table **??**, we select a control region with the same kinematic requirements and derive the template prediction separately. The treatment of the cuts on and is described below in Sec. 4.6.1.

In order to account for kinematic differences between the hadronic systems in the vs. the sample, largely due to the different boson masses, we reweight the sample such that the boson p_{T}

matches that of the sample. This is done for each signal region, where the same requirements are applied to the data as well as the sample. A separate reweighting scheme is derived for each region. The resulting $E_{\mathrm{T}}^{\mathrm{miss}}$ distribution is then normalized in the $50 < E_{\mathrm{T}}^{\mathrm{miss}} < 100$ GeV region where is the dominant background.

Contamination in the data control region from SM processes with true $E_{\mathrm{T}}^{\mathrm{miss}}$ from neutrinos is addressed below in Sec. 4.6.2, then the systematic uncertainties on the method are summarized in Sec. 4.6.4.

4.6.1 emulation for the $E_{\mathrm{T}}^{\mathrm{miss}}$ template method

Two visible objects are needed when calculating the variable, and only one photon is required in the events used to predict the $E_{\mathrm{T}}^{\mathrm{miss}}$ from the background in the electroweak signal region. Therefore in order to emulate the cut in the sample, a method was developed where the photon is decayed to two leptons and is calculated using the two decayed leptons as the visible objects.

This decay is done by assuming the mother particle has the mass of a Z boson and the momentum of the photon reconstructed from data. The angular distribution of the leptons is accounted for by assuming a scenario where the direction of the spin of the mother particle is sampled from a distribution that is uniformly distributed in $1 + \cos^2(\theta)$, where θ is the polar angle in the reference frame in which the mother particle is at rest. After the photon is decayed, the same p_{T} and η requirements that are applied to the events are applied to the decay products from the photon. is constructed using these leptons, and the same cut is applied as in each signal region. Finally, the p_{T} distribution is reweighted in the same way as described in the previous section.

4.6.2 Correcting Electroweak contamination in tails of $E_{\mathrm{T}}^{\mathrm{miss}}$ templates

After selecting events with a high-p_{T} photon and large $E_{\mathrm{T}}^{\mathrm{miss}}$, events from electroweak processes with real $E_{\mathrm{T}}^{\mathrm{miss}}$, e.g. where the W decays to $\ell\nu$, can be present in the tail of the $E_{\mathrm{T}}^{\mathrm{miss}}$ distribution. We apply the lepton vetoes from the preselection (Sec. **??**) to reduce these processes as much as possible. We subtract the remaining contribution from the observed data using MC, including , , $\mathrm{t\bar{t}}$, and $Z(\nu\nu)\gamma$.

To remove the overlap between the and samples, we check whether the leading reconstructed photon is matched in $\Delta R < 0.1$ to a gen-level status 1 photon with the `isPromptFinalState` flag. Events with a match are required to come from the sample while events without a match are required to come from the sample.

To check the MC modeling of these processes, we define a control region requiring exactly one muon and one photon, using events triggered by the single muon triggers given in table **??**. The selections applied are:

- exactly one muon, $p_{\mathrm{T}} > 25$ GeV
- exactly one photon, $p_{\mathrm{T}} > 25$ GeV
- $E_{\mathrm{T}}^{\mathrm{miss}} > 50$ GeV
- ≥ 2
- $M_T(\mu, E_{\mathrm{T}}^{\mathrm{miss}}) > 30$ GeV
- > 0.4
- lepton and isolated track vetos for additional leptons

Fairly good agreement is seen for the overall normalization and the shape of both photon p_{T}

and $E_{\mathrm{T}}^{\mathrm{miss}}$, as shown in Fig. 18.

Based on the level of agreement between data and MC in this control region, we take an uncertainty of 30% on the electroweak subtraction for the template prediction. Operationally, we obtain the difference between the prediction with and without the electroweak contamination subtracted and apply 30% of this difference as the uncertainty. There are a couple bins in the analysis where the subtraction makes the prediction negative. In those cases, the central value of the prediction is set to 0.

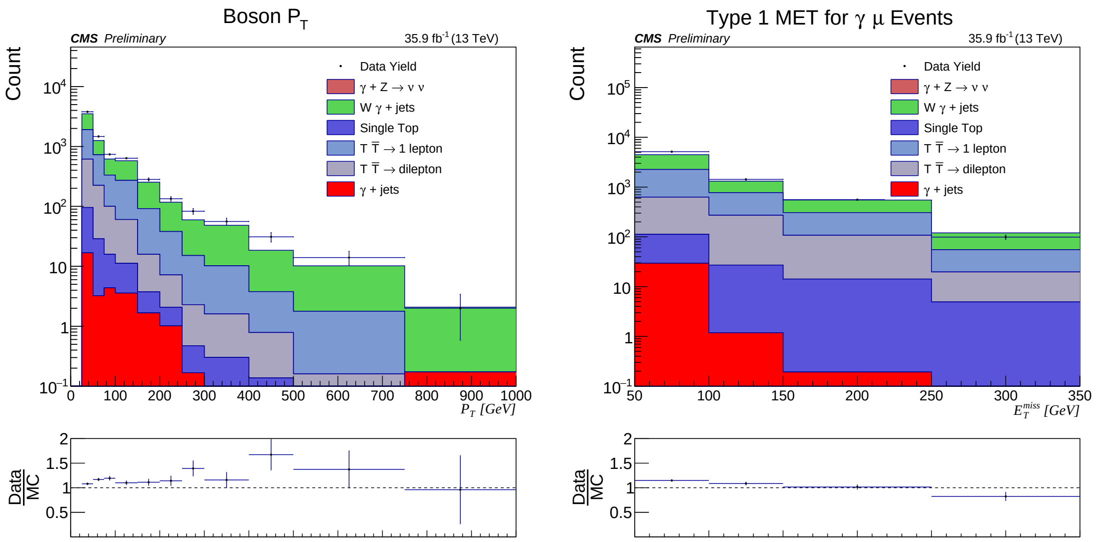

Figure 18: Distributions of (left) photon p_{T} and (right) $E_{\mathrm{T}}^{\mathrm{miss}}$ in the $\mu + \gamma$ control region, showing data vs MC. The $W\gamma$+Jets sample is a cocktail of $W\gamma$+Jets and W+Jets MC where only prompt photons are taken from $W\gamma$+Jets and non-prompt photons, as well as fakes, are taken from the W+Jets sample.

4.6.3 DY Prediction for the Edge Signal Region

In order to get the SM DY background prediction for the Edge analysis, the template method is performed in the Edge baseline signal region without a veto on additional leptons or isolated tracks; the isolated track veto is not used in the Edge signal region to increase sensitivity to certain models used for interpretation. The prediction is obtained by integrating the number of events expected with $E_{\mathrm{T}}^{\mathrm{miss}} > 150$ GeV, and this value is scaled using a set of factors, $\mathrm{R}_{\mathrm{out/in}}$, to get the number of expected events in the various bins considered. The $\mathrm{R}_{\mathrm{out/in}}$ factors are calculated in a control region using data and MC, and the details of this calculation can be found in AN-16-482 [**?**].

4.6.4 Systematic Uncertainties in the $E_{\mathrm{T}}^{\mathrm{miss}}$ Template Prediction

In this section we consider the systematic uncertainty in the $E_{\mathrm{T}}^{\mathrm{miss}}$ template prediction, which comes from four sources:

- the statistical uncertainty of the data sample in each bin of $E_{\mathrm{T}}^{\mathrm{miss}}$
- the MC closure study validating the method
- the normalization of the prediction at low $E_{\mathrm{T}}^{\mathrm{miss}}$
- the electroweak sample subtraction

In previous iterations of this analysis, we also assigned an uncertainty on the photon selection purity by varying the photon selection criteria. This was typically very small and has not been repeated here.

In order to assess systematic uncertainty on the $E_{\mathrm{T}}^{\mathrm{miss}}$ template method, we apply the method in MC and evaluate the overall level of closure. The way this is done is by generating a $E_{\mathrm{T}}^{\mathrm{miss}}$ template using a MC sample and using this template to predict the $E_{\mathrm{T}}^{\mathrm{miss}}$ for events in a MC sample, following section 4.6.

For the MC closure test, we evaluate the systematic uncertainty separately in each of our signal regions. The results of the closure test are shown in detail in appendix **??**. The systematic uncertainty is taken as the larger of the MC statistical uncertainty or non-closure and varies between 10–80% for the various signal regions.

We take the statistical uncertainty from the normalization of the template prediction in data in each signal region (using $E_{\mathrm{T}}^{\mathrm{miss}}$ between 50–100 GeV) as a systematic uncertainty on the prediction. This uncertainty ranges from 7–30% depending on the signal region.

For the electroweak subtraction uncertainty, we take 30% of the difference between the prediction with and without the subtraction. The size of each uncertainty contribution for each signal region bin is summarized in Table 14.

Table 14: Summary of template predictions in all analysis bins together with the uncertainty from each source considered, for . The “ratio” number for each uncertainty shows that particular uncertainty divided by the total template uncertainty for a given bin.

SR	MET Bin	Prediction	Closure (ratio)	Normalization (ratio)	Statistical (ratio)	EWK Sub (ratio)
SRA	50-100	208.50 ± 16.09	0.00 (0.00)	15.29 (0.95)	5.02 (0.31)	0.00 (0.00)
	100-150	13.61 ± 3.14	2.72 (0.87)	1.00 (0.32)	1.14 (0.36)	0.34 (0.11)
	150-250	2.45 ± 0.87	0.64 (0.74)	0.18 (0.21)	0.36 (0.42)	0.42 (0.49)
	250+	3.26 ± 2.36	0.85 (0.36)	0.24 (0.10)	2.16 (0.91)	0.39 (0.16)
SRAb	50-100	92.20 ± 10.36	0.00 (0.00)	9.99 (0.96)	2.76 (0.27)	0.00 (0.00)
	100-150	8.21 ± 2.10	1.64 (0.78)	0.89 (0.42)	0.92 (0.44)	0.27 (0.13)
	150-250	1.19 ± 0.54	0.31 (0.57)	0.13 (0.24)	0.24 (0.45)	0.35 (0.65)
	250+	0.51 ± 0.27	0.13 (0.48)	0.05 (0.20)	0.15 (0.56)	0.18 (0.64)
SRB	50-100	130.06 ± 12.77	0.00 (0.00)	12.11 (0.95)	4.07 (0.32)	0.00 (0.00)
	100-150	12.81 ± 2.35	1.54 (0.65)	1.19 (0.51)	1.30 (0.56)	0.16 (0.07)
	150-250	0.89 ± 0.34	0.13 (0.39)	0.08 (0.24)	0.22 (0.66)	0.20 (0.59)
	250+	0.38 ± 0.20	0.06 (0.29)	0.04 (0.18)	0.12 (0.63)	0.14 (0.69)
SRBb	50-100	37.93 ± 6.74	0.00 (0.00)	6.45 (0.96)	1.93 (0.29)	0.00 (0.00)
	100-150	7.74 ± 3.11	0.93 (0.30)	1.32 (0.42)	2.65 (0.85)	0.23 (0.07)
	150-250	4.04 ± 3.33	0.73 (0.22)	0.69 (0.21)	3.16 (0.95)	0.25 (0.07)
	250+	0.10 ± 0.14	0.02 (0.13)	0.02 (0.12)	0.04 (0.28)	0.14 (0.94)
SRC	50-100	23.76 ± 5.54	0.00 (0.00)	5.22 (0.94)	1.86 (0.34)	0.00 (0.00)
	100-150	1.24 ± 0.43	0.19 (0.43)	0.27 (0.64)	0.27 (0.63)	0.04 (0.09)
	150+	0.13 ± 0.11	0.04 (0.36)	0.03 (0.27)	0.05 (0.51)	0.08 (0.74)
SRCb	50-100	9.88 ± 3.73	0.00 (0.00)	3.45 (0.92)	1.42 (0.38)	0.00 (0.00)
	100-150	0.14 ± 0.47	0.03 (0.06)	0.05 (0.10)	0.04 (0.08)	0.47 (0.99)
	150+	0.00 ± 0.33	0.00 (0.00)	0.00 (0.00)	0.00 (0.00)	0.33 (1.00)
TChiWZ	50-100	773.18 ± 31.90	0.00 (0.00)	29.92 (0.94)	11.06 (0.35)	0.00 (0.00)
	100-150	29.27 ± 4.42	3.22 (0.73)	1.13 (0.26)	2.15 (0.49)	1.81 (0.41)
	150-250	2.87 ± 2.09	0.69 (0.33)	0.11 (0.05)	0.40 (0.19)	1.93 (0.92)
	250-350	1.00 ± 0.73	0.24 (0.33)	0.04 (0.05)	0.24 (0.33)	0.64 (0.88)
	350+	0.29 ± 0.30	0.07 (0.23)	0.01 (0.04)	0.08 (0.26)	0.28 (0.94)
TChiHZ	50-100	76.69 ± 9.39	0.00 (0.00)	9.08 (0.97)	2.39 (0.25)	0.00 (0.00)
	100-150	2.90 ± 2.39	2.32 (0.97)	0.34 (0.14)	0.41 (0.17)	0.24 (0.10)
	150-250	0.26 ± 0.19	0.09 (0.47)	0.03 (0.16)	0.08 (0.44)	0.14 (0.75)
	250+	0.09 ± 0.07	0.03 (0.45)	0.01 (0.16)	0.05 (0.77)	0.03 (0.42)

4.7 Estimating the Flavor-Symmetric Background with eμ Events

The flavor symmetric background prediction relies on a control sample of $e\mu$ or opposite-flavor (OF) events. For each signal region, a corresponding OF region is selected with the same kinematic requirements, except that the window requirement is loosened to be just $>$ 20 GeV. Two scaling factors are needed to convert the OF yield into a prediction:

- $\kappa \equiv \frac{N^{OF}(86<<96)}{N^{OF}(>20)}$, which scales the OF yield to account for the wider window used. This is discussed in detail below.
- , which transforms the OF yield into a prediction for SF. It includes lepton and trigger efficiency effects. The derivation of and its uncertainty is covered in detail in AN-16-482 [**?**]. We use the number from the direct control region determination for this analysis, 1.109 ± 0.046, which includes both statistical and systematic uncertainties.

The factor κ accounting for the wider window is derived on MC and checked in data. The expected OF yields in our signal regions are quite small, which motivates using this method. It also means that we cannot check κ in our exact signal region selections in data, so we instead check with looser selections.

The results are summarized in Fig. 19. The first three bins labeled "baseline" require the preselection, $>$ 80 GeV, and the $E_{\mathrm{T}}^{\mathrm{miss}}$ selection shown. The next regions labeled "Strong region, b-veto" and "Strong region, with bs" require the btagging and selections from the strong regions but do not include the further , , or $E_{\mathrm{T}}^{\mathrm{miss}}$ cuts. The last regions shown are the electroweak HZ and VZ regions with $E_{\mathrm{T}}^{\mathrm{miss}} > 100$ GeV.

This plot motivates the value of $\kappa = 0.065 \pm 0.020$. The uncertainty is taken to cover the differences in central values observed in MC. The statistical uncertainties on the data are larger but we see agreement within the assigned systematic uncertainty.

4.8 Estimating WZ, ZZ and other rare SM backgrounds using MC

The SM background predictions not covered by the above methods are predicted using MC. To avoid counting events that are already predicted by the data driven methods above, we use only MC events with prompt electrons or muons consistent with a Z boson decay and at least one prompt neutrino. The WZ, ZZ, and samples are verified in 3 and 4-lepton control regions. We take a 30% uncertainty on WZ and , a 50% uncertainty on ZZ, based on the studies documented in AN-16-482 [**?**]. Please refer to this AN for the details. We take a 50% uncertainty on all other rare samples used.

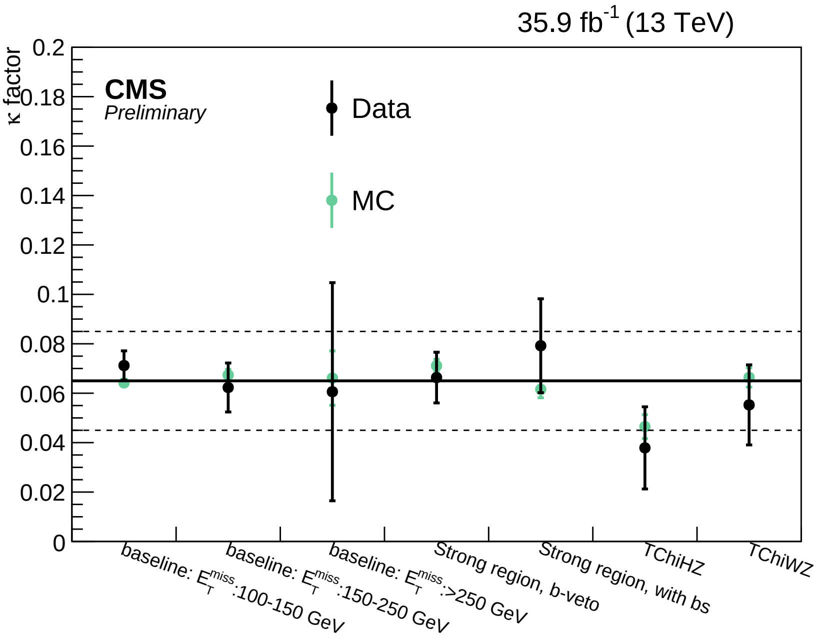

Figure 19: Comparison of κ in different baseline signal regions, in data and MC. The solid black line shows the central value of 0.065, and the dashed lines show the systematic uncertainty.

5 Search for a Kinematic Edge

In addition to a cut and count approach, a fit is performed to the mass spectrum to search for a kinematic edge. The fit is carried out simultaneously to the distribution in the dielectron, dimuon, and opposite flavor final state.

The fit consists of three separate components: the flavor-symmetric backgrounds, backgrounds containing a Z, and signal; the corresponding shapes are detailed in the following.

5.1 Model for Flavor-Symmetric Backgrounds

The FS background is described using a Crystal-Ball funtion: $\mathcal{P}_{FSCB}(m_{\ell\ell})$:

$$\mathcal{P}_{FSCB}(m_{\ell\ell}) = \begin{cases} \exp\left(-\frac{(m_{ll}-\mu_{FSCB})^2}{2\sigma^2_{FSCB}}\right) & \text{if } \frac{m_{ll}-\mu_{FSCB}}{\sigma_{FSCB}} < \alpha_{FS}, \\ A(B + \frac{m_{ll}-\mu_{FSCB}}{\sigma_{FSCB}})^{-n_{FS}} & \text{if } \frac{m_{ll}-\mu_{FSCB}}{\sigma_{FSCB}} > \alpha_{FS}, \end{cases} \tag{8}$$

where

$$A = \left(\frac{n}{|\alpha_{FS}|}\right)^{n_{FS}} \exp\left(-\frac{|\alpha_{FS}|^2}{2}\right) \quad \text{and} \quad B = \frac{n_{FS}}{|\alpha_{FS}|} - |\alpha_{FS}|. \tag{9}$$

Because of the requirement that the function and its derivative both be continuous, the FS model is left with four independent parameters plus the normalization.

While the three samples (dielectron, dimuon and opposite flavor) have different normalizations, they all use the same FS shape parameters:

$$\vec{p}_{FS} = (\mu_{FSCB}, \sigma_{FSCB}, \alpha_{FS}, n_{FS})$$

5.2 Model for Backgrounds Containing a Z

The shape for backgrounds containing a Z is based on the sum of an exponential function and a convolution of a Breit-Wigner $\mathcal{P}_{BW}(m_{ll}; m_Z, \sigma_Z)$ (with physical mean m_Z and width σ_Z) and a double-sided Crystal-Ball function $\mathcal{P}_{DSCB}(m_{\ell\ell})$:

$$\mathcal{P}_{DSCB}(m_{\ell\ell}) = \begin{cases} A_1(B_1 - \frac{m_{ll}-\mu_{CB}}{\sigma_{CB}})^{-n_1} & \text{if } \frac{m_{ll}-\mu_{CB}}{\sigma_{CB}} < -\alpha_1 \\ \exp\left(-\frac{(m_{ll}-\mu_{CB})^2}{2\sigma^2_{CB}}\right) & \text{if } -\alpha_1 < \frac{m_{ll}-\mu_{CB}}{\sigma_{CB}} < \alpha_2 \\ A_2(B_2 + \frac{m_{ll}-\mu_{CB}}{\sigma_{CB}})^{-n_2} & \text{if } \frac{m_{ll}-\mu_{CB}}{\sigma_{CB}} > \alpha_2 \end{cases}$$

where

$$A_i = \left(\frac{n_i}{|\alpha_i|}\right)^{n_i} \cdot \exp\left(-\frac{|\alpha_i|^2}{2}\right) \quad \text{and} \quad B_i = \frac{n_i}{|\alpha_i|} - |\alpha_i|.$$

The full description is therefore

$$\mathcal{P}_{DY}(m_{\ell\ell}) = f_{exp}\mathcal{P}_{exp}(m_{\ell\ell}) + (1 - f_{exp}) \int \mathcal{P}_{DSCB}(m_{\ell\ell})\mathcal{P}_{BW}(m_{\ell\ell} - m')dm'.$$

The model is fit separately for electrons and muons in a control region enriched in backgrounds containing Z's in order to extract the shape, which is then used with all parameters fixed (except the normalization) in the signal region. The control region used to extract the shape is the same as the one used to extract , i.e. contains events with two or more jets, and an upper E_T^{miss} cut at 50 GeV to improve DY purity. The shapes for di-electron events and di-muon events are shown in Fig. 20.

The electron and muon models use different values for the double-sided Crystal Ball function, and the relative normalization (f_{exp}) between the exponential and the convoluted function. They do, however, use the same value for m_Z^{pdg} and σ_Z^{pdg} (fixed to PDG values). The full parameter set in the fit for electrons is

$$\vec{p}^{\,e}_Z = (\mu^{ee}_{CB}, \sigma^{ee}_{CB}, \alpha^{ee}_1, \alpha^{ee}_2, n^{ee}_1, n^{ee}_2, f^{ee}_{exp}, \mu^{ee}_{exp})$$

and for muons

$$\vec{p}^{\,\mu}_Z = (\mu^{\mu\mu}_{CB}, \sigma^{\mu\mu}_{CB}, \alpha^{\mu\mu}_1, \alpha^{\mu\mu}_2, n^{\mu\mu}_1, n^{\mu\mu}_2, f^{\mu\mu}_{exp}, \mu^{\mu\mu}_{exp})$$

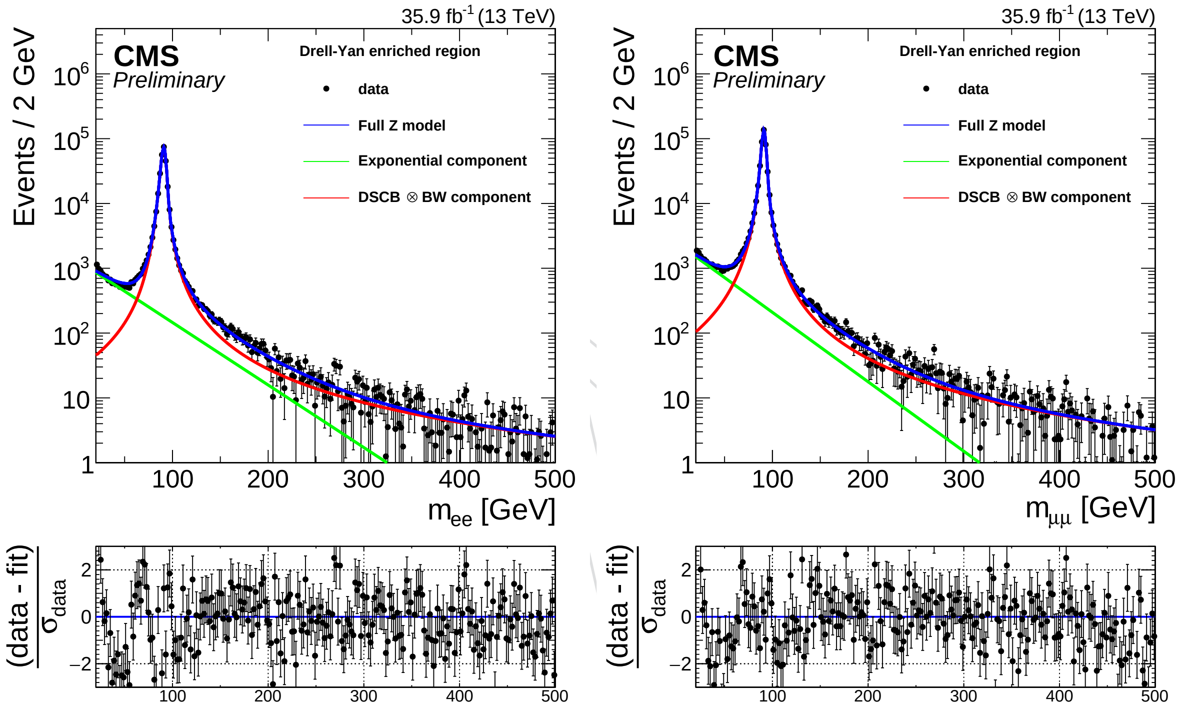

Figure 20: Fitted shape for backgrounds containing a Z for dielectron events (left) and dimuon events (right). The fitted shape consists of an exponential (green) and a Breit-wigner convoluted with a double-sided Chrystal-Ball (red), whose sum (blue) describes the backgrounds containing a Z .

5.3 Signal Model

The signal component is based on an edge model for two subsequent two-body decays with endpoint $m_{\ell\ell}^{edge}$, including a model for the dilepton mass resolution, $\sigma_{\ell\ell}$:

$$\mathcal{P}_S(m_{\ell\ell}) = \frac{1}{\sqrt{2\pi}\sigma_{\ell\ell}} \int_0^{m_{\ell\ell}^{edge}} y \cdot \exp\left(-\frac{(m_{\ell\ell}-y)^2}{2\sigma_{\ell\ell}^2}\right) dy$$

The function describes a triangle convoluted with a Gaussian to account for the mass resolution.

The electron and muon models share the edge position $m_{\ell\ell}^{edge}$, but use their own value for σ (which comes from the model for backgrounds containing a Z). The parameters are therefore

$$\vec{p}_S^{\,e} = (m_{ll}^{edge}, \sigma_{CB}^{ee})$$

for electrons and

$$\vec{p}_S^{\,\mu} = (m_{ll}^{edge}, \sigma_{CB}^{\mu\mu})$$

for muons.

5.4 Complete model

The model for the opposite flavor final state is as follows:

$$\mathcal{P}_{OF}(m_{\ell\ell}) = N_{FS}\mathcal{P}_{FS}(m_{\ell\ell})$$

while the model for the di-electron final state and the di-muon final state also contain the additional components for background with a Z and the signal shape:

$$\begin{aligned}
\mathcal{P}_{ee}(m_{\ell\ell}) &= f_{ee}\left(R_{SF/OF}N_{FS}\mathcal{P}_{FS}(m_{\ell\ell}) + N_Z\mathcal{P}_{Z,ee}(m_{\ell\ell}) + N_S\mathcal{P}_S(m_{\ell\ell}, \sigma_{ee})\right) \\
\mathcal{P}_{\mu\mu}(m_{\ell\ell}) &= f_{\mu\mu}\left(R_{SF/OF}N_{FS}\mathcal{P}_{FS}(m_{\ell\ell}) + N_Z\mathcal{P}_{Z,\mu\mu}(m_{\ell\ell}) + N_S\mathcal{P}_S(m_{\ell\ell}, \sigma_{\mu\mu})\right)
\end{aligned}$$

where N_S is fixed to zero for the null hypothesis. The fraction of same flavor events in the dielectron final state is denoted by f_{ee} , while $f_{\mu\mu}$ is the fraction of same flavor events in the dimuon final state, so that $f_{ee} + f_{\mu\mu} = 1$. In the following, the normalizations are abbreviated as follows:

$$\begin{aligned}
N_{FS}^{e} &= f_{ee}\cdot(R_{SF/OF}N_{FS}) & & & N_{FS}^{\mu} &= f_{\mu\mu}\cdot(R_{SF/OF}N_{FS}) \\
N_{Z}^{e} &= f_{ee}\cdot N_Z & &\text{and} & N_{Z}^{\mu} &= f_{\mu\mu}\cdot N_Z \\
N_{S}^{e} &= f_{ee}\cdot N_S & & & N_{S}^{\mu} &= f_{\mu\mu}\cdot N_S
\end{aligned}$$

Note that N_i^e and N_i^μ are therefore not floating parameters but are analytical expressions of floating parameters; it is also important to point out that f_{ee} is strongly constrained by the total size of the two same flavor datasets,

$$\begin{aligned}
N_{ee} &= f_{ee}\cdot(R_{SF/OF}N_{FS} + N_Z + N_S) \\
N_{\mu\mu} &= \underbrace{(1 - f_{ee})}_{f_{\mu\mu}}\cdot(R_{SF/OF}N_{FS} + N_Z + N_S)\,.
\end{aligned}$$

5.5 Procedure

A first fit is carried out separately for electrons and muons in the DY enriched control region to extract the DY shape (”backgrounds containing a Z”). Due to the size of the control region dataset, the uncertainties on the fitted parameters for the Drell-Yan shape are very small, making a variation of the DY-shape related variables in the full fit unnecessary.

A fit is then carried out in the signal region using an extended unbinned maximum likelihood fit, which is performed simultaneously for the dilepton invariant mass distribution in the dielectron, dimuon, and opposite flavor final state simultaneously. The likelihood is given by

$$
\begin{aligned}
\mathcal{L}(m_{\ell\ell};\mathbf{p}) = \quad & \frac{e^{-N^e_{FS}-N^e_Z-N^e_S-N^\mu_{FS}-N^\mu_Z-N^\mu_S-N^{OF}_{FS}}}{N!} \\
\times \quad & \prod_{\mathrm{e^+e^-}} \left[N^e_{FS}\cdot\mathcal{P}_{FS}(m_{\ell\ell};\mathbf{p}_{FS}) + N^e_Z\cdot\mathcal{P}_Z(m_{\ell\ell};\mathbf{p}^e_Z) + N^e_S\cdot\mathcal{P}_S(m_{\ell\ell};\mathbf{p}^e_S)\right] \\
\times \quad & \prod_{\mu^+\mu^-} \left[N^\mu_{FS}\cdot\mathcal{P}_{FS}(m_{\ell\ell};\mathbf{p}_{FS}) + N^\mu_Z\cdot\mathcal{P}_Z(m_{\ell\ell};\mathbf{p}^\mu_Z) + N^\mu_S\cdot\mathcal{P}_S(m_{\ell\ell};\mathbf{p}^\mu_S)\right] \\
\times \quad & \prod \left[N^{OF}_{FS}\cdot\mathcal{P}_{FS}(m_{\ell\ell};\mathbf{p}_{FS})\right] \\
\times \quad & \mathcal{G}\left(\mathbf{p};\text{constraints}\right)
\end{aligned}
$$

This likelihood has only one variable, the invariant di-lepton mass $m_{\ell\ell}$; N is the total number of events processed.

A penalty is added to take into account. This is done by using a Gaussian PDF centered at with σ equal to the uncertainty on :

$$
\mathcal{G}\left(\frac{N^e_{FS}+N^\mu_{FS}}{N^{OF}_{FS}};R_{SF/OF},\sigma_{R_{SF/OF}}\right),
$$

where and $\sigma_{R_{SF/OF}}$ are the values determined in Sec. 4.1.3.

An overview of the floating parameters in the fit in the signal region is given in Tab. 15, while the parameters in the fit in the control region (to extract the Drell-Yan shape) are summarised in Tab. 16 (these parameters are frozen in the full fit).

	Parameter	status	initial value	range
	N^{OF}_{FS}, N_Z	floating	-	$[0.0,\infty[$
	N_S	floating	-	$]-\infty,\infty[$
		constrained	^{comb}	$^{comb} \pm 4\cdot\sigma_{comb}$
	f_{ee}	floating	-	$[0,1]$
$\vec{p}_{FS}$	μ_{FSCB}	floating	50	$[0,200]$
	σ_{FSCB}	floating	20	$[0,100]$
	α_{FS}	floating	1	$[0,10]$
	n_{FS}	floating	1	$[0,100]$
$\vec{p}_S$	m^{edge}_{ll}	floating	-	$[30,500]$

Table 15: Overview of all floating parameters in the full fit in the signal region, including their status, initial value and parameter range. Note that the parameters pertaining to the Drell-Yan shape (summarized in Tab. 16) are fixed.

5.6 Closure Test

The fit is carried out using background Monte Carlo simulation first under the null hypothesis (results are shown in Fig. 21), and then under the signal hypothesis (see Fig. 22). In the absence of a signal, the fit reconstructs a small signal yield compatible with 0 ($N_S = 14.6 \pm 25.9$).

	Parameter	status	initial value	minimum	maximum
$\vec{p}_Z^e$	μ_{CB}^{ee}	floating	3.0	-10	10
	σ_{CB}^{ee}	floating	1.6	0	20
	α_1^{ee}	floating	1.16	0	10
	α_2^{ee}	floating	2.5	0	10
	n_1^{ee}	floating	2.9	0	20
	n_2^{ee}	floating	1.0	0	100
	f_{exp}^{ee}	floating	0.003	0	1000
	μ_{exp}^{ee}	floating	-0.02	-0.1	0
$\vec{p}_Z^\mu$	$\mu_{CB}^{\mu\mu}$	floating	3.0	-10	10
	$\sigma_{CB}^{\mu\mu}$	floating	1.6	0	20
	$\alpha_1^{\mu\mu}$	floating	1.16	0	10
	$\alpha_2^{\mu\mu}$	floating	2.5	0	10
	$n_1^{\mu\mu}$	floating	2.9	0	20
	$n_2^{\mu\mu}$	floating	1.04	0	20
	$f_{exp}^{\mu\mu}$	floating	0.003	0	1000
	$\mu_{exp}^{\mu\mu}$	floating	-0.02	-0.1	0

Table 16: Overview of all floating parameters in the fit in the Drell-Yan enriched control region, including their status, initial value and parameter range

	Parameter	N_{FS}	N_{FS}^{e}	N_{FS}^{μ}	$N_Z^e \mathcal{P}_{Z,ee}$	$N_Z^{\mu} \mathcal{P}_{Z,\mu\mu}$	$N_S^e \mathcal{P}_{S,ee}$	$N_S^{\mu} \mathcal{P}_{S,\mu\mu}$
	N_{FS}^{OF}	n	n	n				
	N_Z				n	n		
	N_S						n	n
			n	n				
	f_{ee}		n	n	n	n	n	n
$\vec{p}_{FS}$	$\mu_{FS,CB}$	$\surd$	$\surd$	$\surd$				
	$\sigma_{FS,CB}$	$\surd$	$\surd$	$\surd$				
	α_{FS}	$\surd$	$\surd$	$\surd$				
	n_{FS}	$\surd$	$\surd$	$\surd$				
$\vec{p}_S$	m_{ll}^{edge}						$\surd$	$\surd$
$\vec{p}_Z^{\,e}$	μ_{CB}^{ee}				$\surd$			
	σ_{CB}^{ee}				$\surd$		$\surd$	
	α_1^{ee}				$\surd$			
	α_2^{ee}				$\surd$			
	n_1^{ee}				$\surd$			
	n_2^{ee}				$\surd$			
	f_{exp}^{ee}				$\surd$			
	μ_{exp}^{ee}				$\surd$			
$\vec{p}_Z^{\,\mu}$	$\mu_{CB}^{\mu\mu}$					$\surd$		
	$\sigma_{CB}^{\mu\mu}$					$\surd$		$\surd$
	$\alpha_1^{\mu\mu}$					$\surd$		
	$\alpha_2^{\mu\mu}$					$\surd$		
	$n_1^{\mu\mu}$					$\surd$		
	$n_2^{\mu\mu}$					$\surd$		
	$f_{exp}^{\mu\mu}$					$\surd$		
	$\mu_{exp}^{\mu\mu}$					$\surd$		

Table 17: Use of floating parameters for the different components; parameters used for the normalization are marked with an "n", parameters used for the shape are ticked ($\surd$). Note that parameters in $\vec{p}_Z^{\,i}$ are frozen in the fit in the signal region.

Fig. 23-26 show the fit for injected signal MC under the null hypothesis for and the signal hypothesis. T6bbslepton scenarios with a mass of 850 and 800 GeV and masses of 150 (Fig. 23 and 24) and 300 GeV (Fig. 26 and 26) are used. In combination with the mass of 100 GeV this yields kinematic endpoints for the edge shape in the distibution at 50 and just below 200 GeV. Especially for high neutralino mass differences the endpoint of the shape tends to be washed out and results in mass edges below the actual mass difference. In the presence of an injected signal, the likelihood significantly improves when evaluating H_1 as opposed to H_0, and a large signal yield is obtained. In the considered scenarios the found number of signal events is $N_S = 40 \pm 25$ (130 ± 30) for the edge at 50 (200) GeV while the injected number of signal MC events are $N_S^{true} = 58$ (153). The reconstructed edge positions of the injected signals are determined to be $m_{\ell\ell}^{edge} = 49.6 \pm 4.2\,\text{GeV}$ and $190.9 \pm 2.8\,\text{GeV}$. As mentioned, for the injected mass at 200 GeV the reconstructed mass is a about 10 GeV below the actual mass difference due to the MC kinematics.

5.7 Fit in Control Region

To test the fit performance on data, it is performed in the $\mathrm{t\bar{t}}$ control region with exactly two jets and $E_{\mathrm{T}}^{\mathrm{miss}}$ between 100 and 150 GeV, where no excess above Standard Model prediction is expected. To make the selection more similar to the one in the signal region of the kinematic fit the requirements $MT2 > 80$ GeV and $|\Delta\phi(\mathrm{jet}_{1,2}, MET)| > 0.4$ are applied as well. The fit results for the H1 hypothesis are shown in Figure 27. No significant excess above Standard Model expectation is observed. The best edge position is found for a small fluctuation at an invariant mass of about 125 GeV.

5.8 Shape Variation

As a cross check, the shape that was used to model the FS background at 8 TeV is still used. This shape is split into three regions: a low-mass region modeling the rising distribution shaped by lepton acceptance requirements, a transition region, and a high-mass region in which the distribution falls exponentially. The probability density functions describing the three regions are:

$$\mathcal{P}_{FSold}(m_{\ell\ell}) = \begin{cases} \mathcal{P}_{FSold,1}(m_{\ell\ell}) = c_1 \cdot m_{\ell\ell}^{\alpha} & \text{if } 20\,\text{GeV} < m_{\ell\ell} < m_{\ell\ell}^{(1)}, \\ \mathcal{P}_{FSold,2}(m_{\ell\ell}) = \sum_{i=1}^{4} c_{2,i} \cdot m_{\ell\ell}^{i-1} & \text{if } m_{\ell\ell}^{(1)} < m_{\ell\ell} < m_{\ell\ell}^{(2)}, \\ \mathcal{P}_{FSold,3}(m_{\ell\ell}) = c_3 \cdot e^{-\beta m_{\ell\ell}} & \text{if } m_{\ell\ell}^{(2)} < m_{\ell\ell} < 500\,\text{GeV}, \end{cases} \tag{10}$$

where $m_{\ell\ell}^{(1)}$ and $m_{\ell\ell}^{(2)}$ define the boundaries between the regions. In this case five independent parameters plus the normalization remain.

The comparison of old and new shape on MC can be seen in Fig. 28 and 29. Overall, the new shape gives a slightly better agreement between MC data and fit, requires less free parameters and thus performs faster and more stable.

5.9 Fit performance studies using toy MC

The performance of the fit is studied using toy datasets. These are generated by fitting the background shape for flavour-symmetric backgrounds to OF in simulation. From this shape new opposite-flavour datasets are generated, fluctuating the normalization using a Poisson distribution. Electron-electron and muon-muon datasets are generated by adding the Z peak model. The Z and flavour-symmetric yield is split into these two datasets using the value measured in data and fluctuated independently. The combined fit is performed on these datasets.

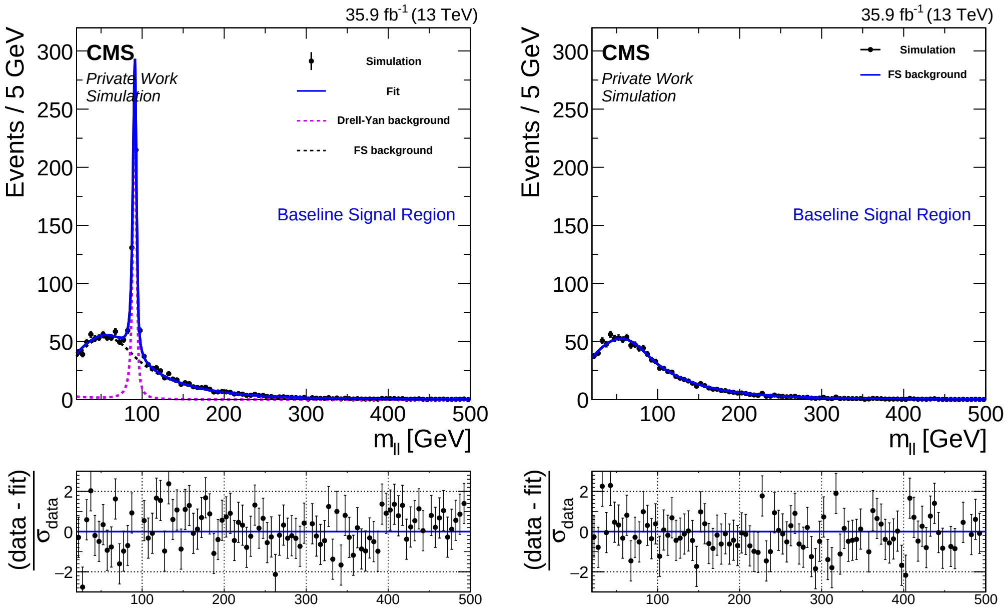

Figure 21: Result of fit in signal region for same-flavor (left) and opposite-flavor (right) events for Monte Carlo simulation **without injected signal** evaluating the **null hypothesis**.

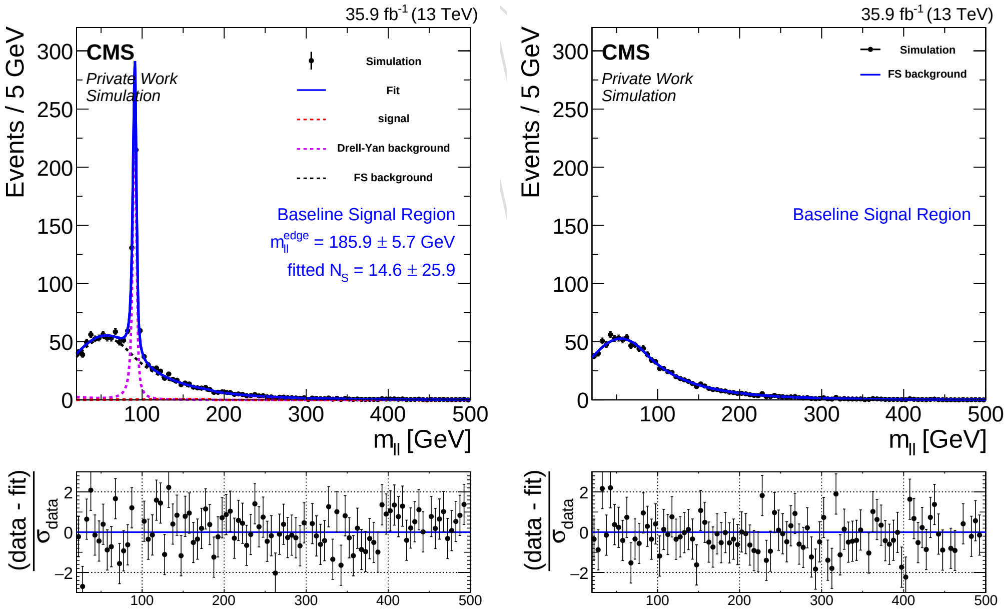

Figure 22: Result of fit in signal region for same-flavor (left) and opposite-flavor (right) events for Monte Carlo simulation **without injected signal** evaluating the **signal hypothesis**.

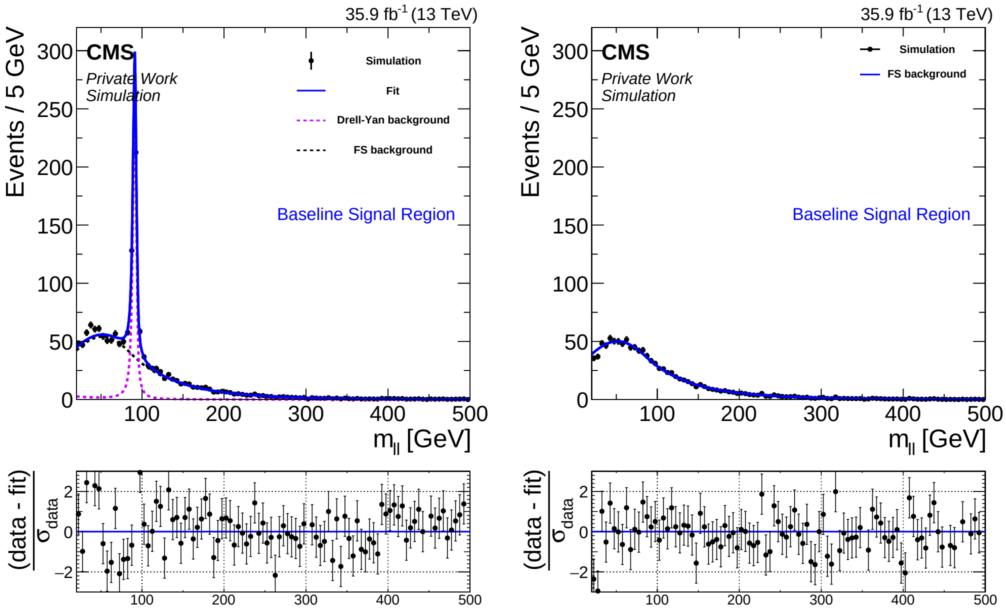

Figure 23: Result of fit in signal region for same-flavor (left) and opposite-flavor (right) events for Monte Carlo simulation **with an injected signal at 50 GeV** evaluating the **null hypothesis**.

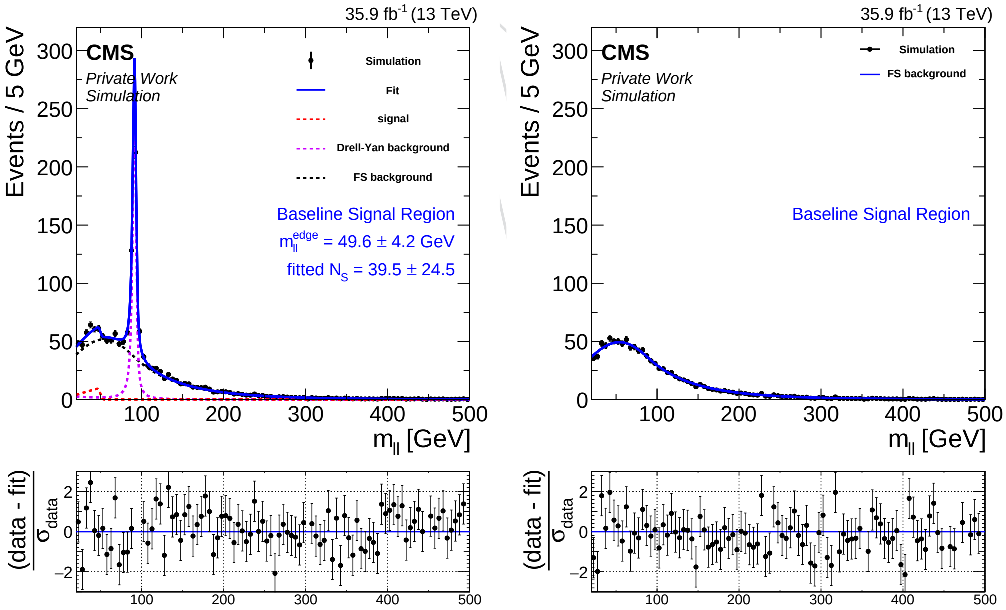

Figure 24: Result of fit in signal region for same-flavor (left) and opposite-flavor (right) events for Monte Carlo simulation **with an injected signal at 50 GeV** evaluating the **signal hypothesis**.

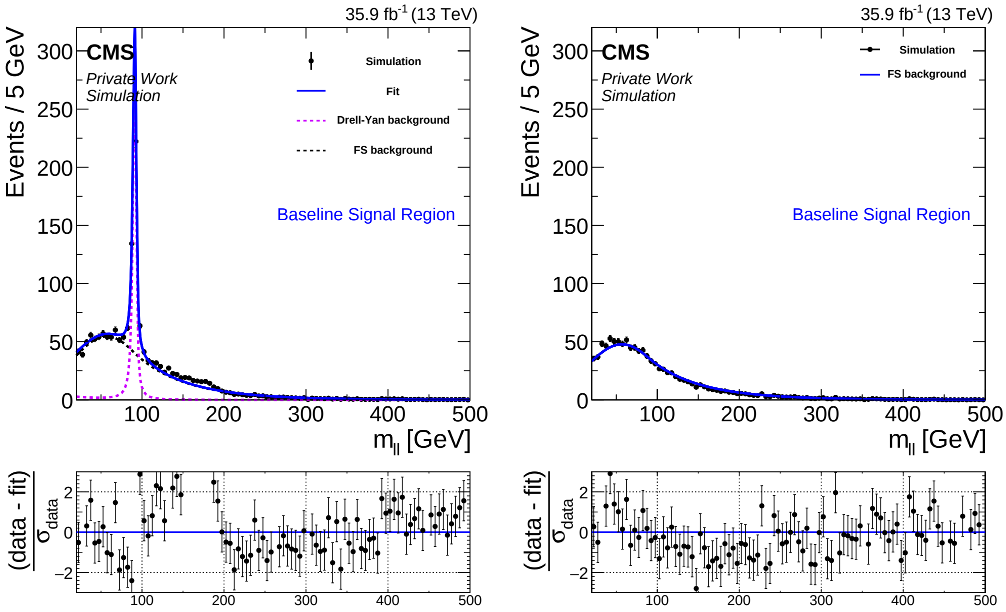

Figure 25: Result of fit in signal region for same-flavor (left) and opposite-flavor (right) events for Monte Carlo simulation **with an injected signal just below 200 GeV** evaluating the **null hypothesis**.

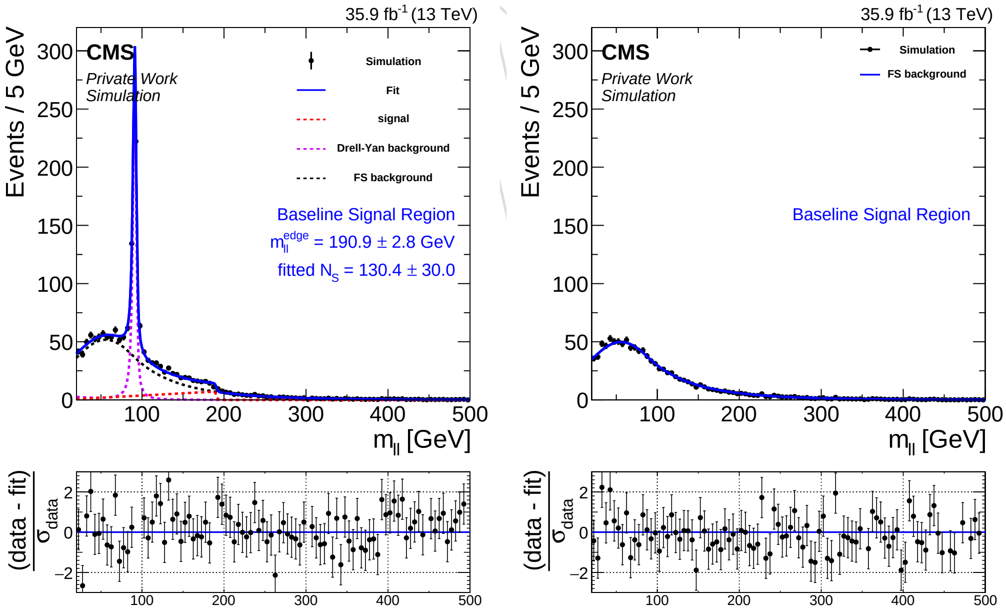

Figure 26: Result of fit in signal region for same-flavor (left) and opposite-flavor (right) events for Monte Carlo simulation **with an injected signal just below 200 GeV** evaluating the **signal hypothesis**.

5.9.1 Toy studies without signal injection

The edge fit is performed on toys generated from the background models only. Figure 30 shows resulting distributions for the fitted number of signal events. Two configurations of the fit are used in these studies. In the first case (black) the edge position is a free parameter while in the other case (blue) it is fixed to 150 GeV. The left plot shows just the number of fitted signal events. On the right the number of fitted signal events divided by the fitted uncertainty is shown. The distribution with a floating edge position exhibits two peaks, symmetrically below and above zero. As the fit will choose an edge position for which the likelihood is improved the most when the signal model is included compared to the background only model, this biases the fit towards more significant signals. Since the fit can also vary within its uncertainties, it can also increase and fit a negative signal contribution to compensate this. This results in slightly more cases where a negative signal yield is fitted. In case of a fixed edge position, the distribution of $N_{sig}/\sigma_{N_{sig}}$ is now a unit Gaussian centred around zero, as one would expect in the absence of a signal.

5.9.2 Toy studies with signal injection

Further studies have been performed with signal events injected at different edge positions. The following combinations of edge position and number of signal events have been studied: 50 GeV / 50 events, 100/200, 150/150, 200/100, 250/200, 300/50. The pull distribution $((N_{sig} - N_{injected})/\sigma_{N_{sig}})$ is shown in figure 31 for a floating edge position and a fixed edge. If the edge position is fixed, the pull distribution peaks at 0 with a width of 1 as expected for an unbiased method. If the edge position is left floating a bias is introduced, which is expected since the floating edge introduces a look-elsewhere-effect. The look-elsewhere-effect can cause the fit to find less signal events than injected or even to fit a fluctuation in a different mass regime. Several effects have an impact on the probability not to find the injected signal:

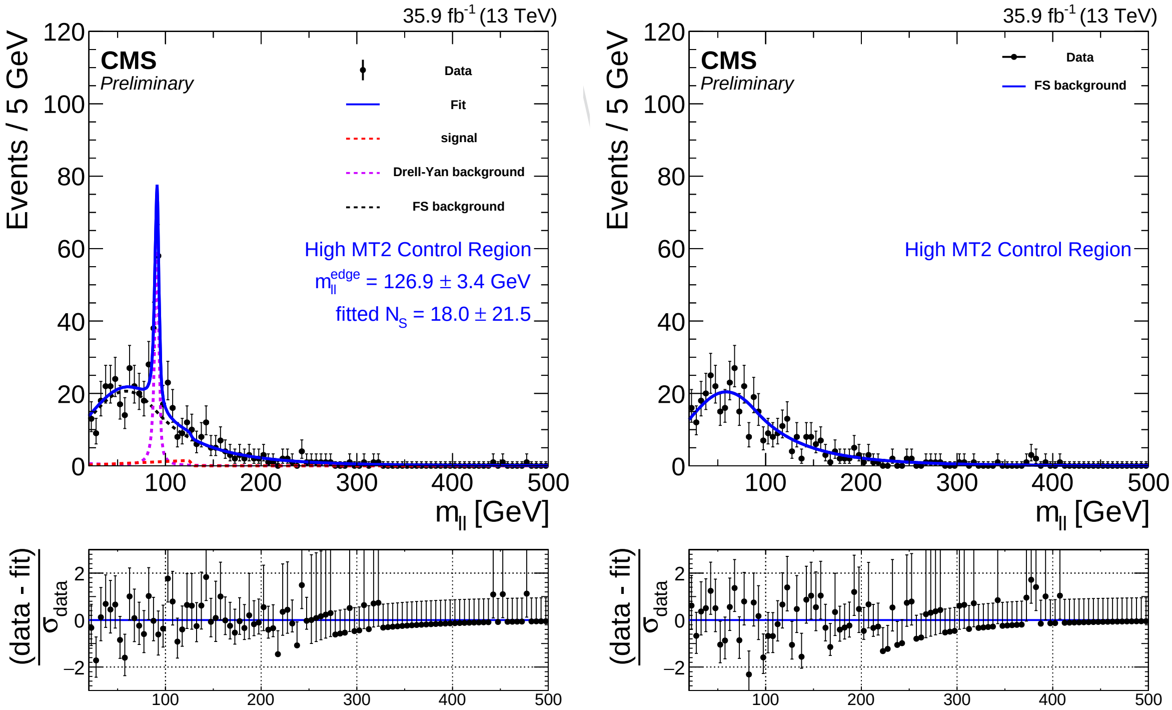

Figure 27: Fit to dilepton-mass distributions in the control region.

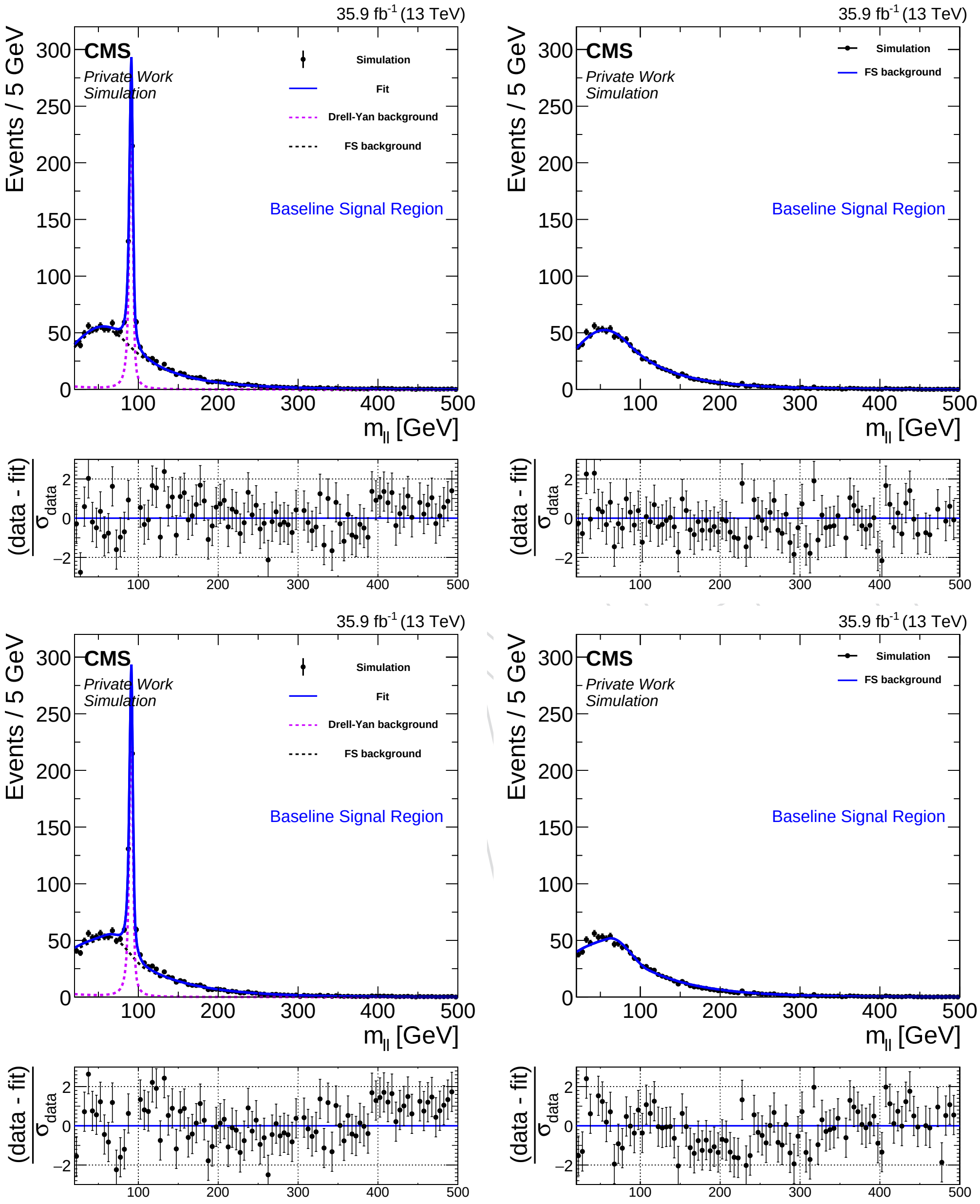

Figure 28: Result of fit in signal region for same-flavor (left) and opposite-flavor (right) events using the standard (upper) and the old shape (lower) for Monte Carlo simulation **without injected signal** evaluating the **null hypothesis**.

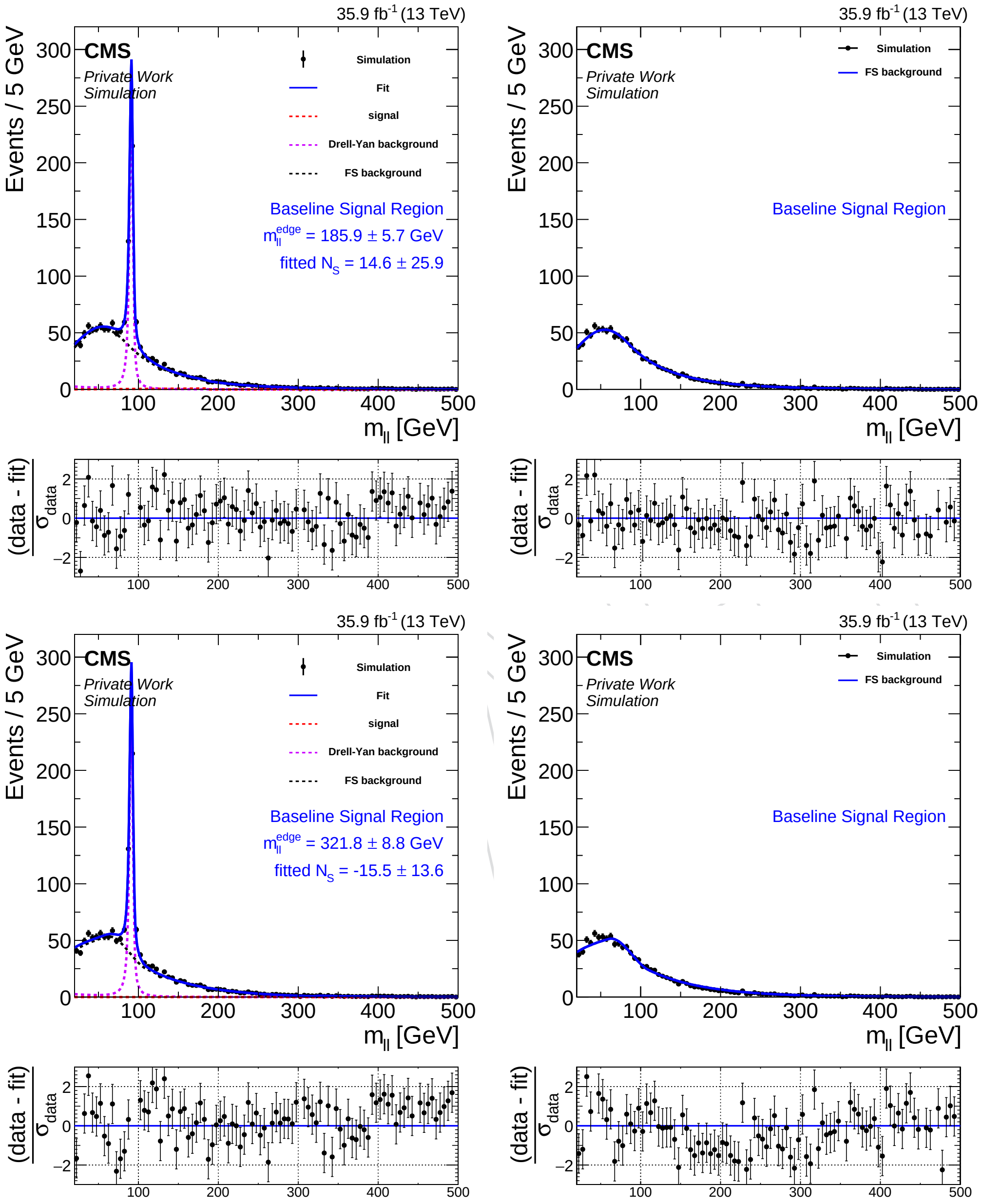

Figure 29: Result of fit in signal region for same-flavor (left) and opposite-flavor (right) events using the standard (upper) and the old shape (lower) for Monte Carlo simulation **without injected signal** evaluating the **signal hypothesis**.

- If the number of signal events is small the probability of fitting a fluctuation elsewhere increases (e.g. combinations 50/50, 300/50);
- For low/moderate mass edges, the signal/background ratio is smaller since most of the background is located in this regime. Thus, a signal at high mass is easier to catch than a signal at low mass (50/50 vs. 300/50 or 100/200 vs. 250/200);
- A special case is an edge at or just above the Z mass. A larger Z contribution can be fitted which reduces the number of signal events (combination 100/200);
- The anti-correlation between the number of fitted signal events and causes the asymmetry in the tails. As can be observed in the left plot of figure 32 for the (150/150) case, the fit can use a larger value of in combination with a smaller signal yield. For a fixed edge positon no correlation is observed.

All of these effects are taken into account by using background only toys that are subject to these effects as well when the p-value and significance of a fit result is determined. Toys with a constant edge position are used to evaluate the local significance (i.e. no look-elsewhere-effect is considered) while toys with a floating edge position yield the global p-value and significance.

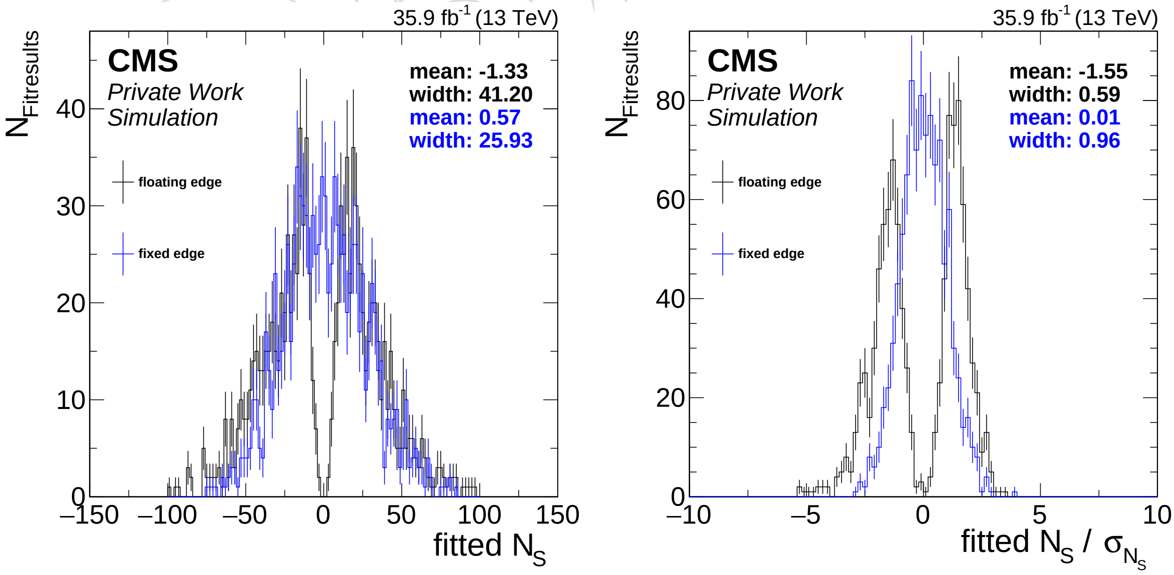

Figure 30: Distribution of fit observables in toy studies for background only toys. Shown are the fitted number of signal events (left) and the fitted number of signal events divided by the fitted uncertainty (right) for a floating edge position (black) and an edge fixed at 150 GeV.

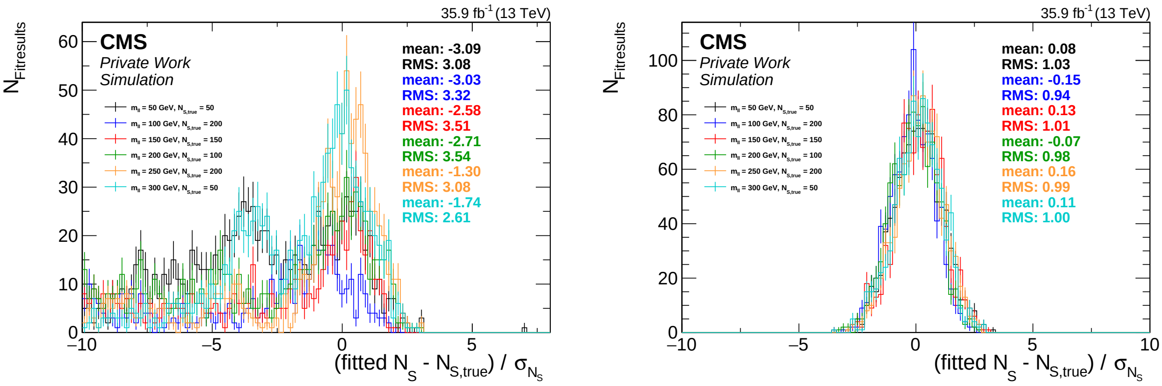

Figure 31: Distribution of fit observables in toy studies for different signal scenarios. Shown are the fitted number of signal events subtracted by the number of injected signal events divided the fitted uncertainty for a floating edge position (left) and a fixed edge (right).

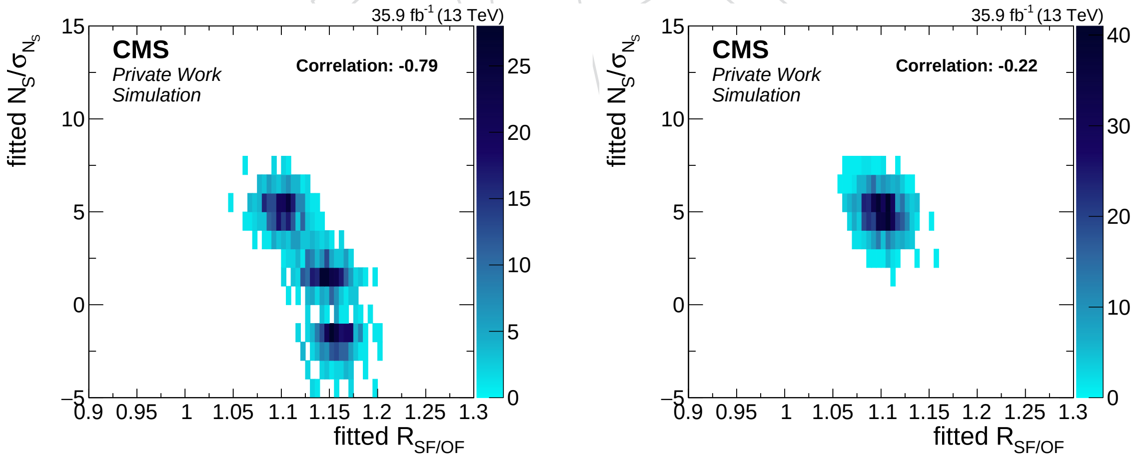

Figure 32: Distribution of fit observables in toy studies for a signal of 150 events injected at 150 GeV. Shown are the fitted number of signal events subtracted by the number of injected signal events divided the fitted uncertainty for a floating edge position (left) and a fixed edge at 150 GeV (right) as a function of the fitted value.

6 Results

This chapter summarizes the results of the cut and count off-Z edge and electroweak on-Z searches as well as for the kinematic fit for the full 140 fb^{-1} of 2016 data.

6.1 Cut and Count experiment in the edge search

In this section, the results of the edge search on the unblinded dataset are presented.

The spectra of the $t\bar{t}$ like and non $t\bar{t}$ like selection are shown in Fig. 33, while a visualization of all signal regions (including the ICHEP and 8 TeV legacy regions) is shown in Fig. 34. Each mass bin in Fig. 33 corresponds to one signal bin, while the Z window is excluded since it is not part of the edge signal regions.

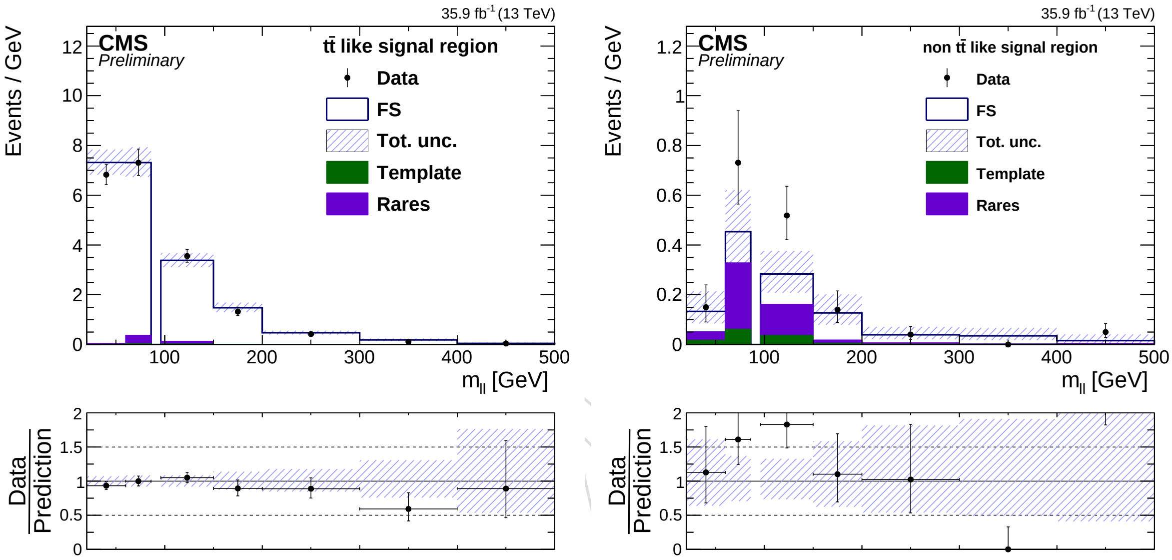

Figure 33: Results of the counting experiment of the edge search for both $t\bar{t}$ like (left) and non $t\bar{t}$ like (right) selection. The data is shown as dots, the estimated flavor symmetric background as a white area, the non flavor symmetric with instrumental from the MET-template method as a green area and rare Z+ν backgrounds as a violet area. The total background uncertainty is given as a shaded blue band. The ratio of observed data to the total background estimates is shown below the plot. Each mass bin corresponds to one signal bin and the Z window (86-96 GeV) is excluded.

The quantitative results in the fourteen bins for the different and selections and the two regions where deviations were observed at 8 TeV or in the ICHEP dataset are shown in Tab. 18. Especially at high mass and in the non ttbar like regions the uncertainty on the background prediction is driven by the Poisson uncertainty on the number of events in the OF sample. Good agreement between the data and background estimates are observed in most bins. In the highest mass bin in the high-selection about 1.5 background event is expected while 5 events are observed. In the mass bin from 96-150 GeV $15.3^{+5.0}_{-4.1}$ events are expected and 28 events observed. This corresponds to a local significance of 2.0 σ. Two super signal regions were defined by combining all non ttbar like mass regions below/above the Z peak. Due to the mentioned deviations, there are 44 events observed in the super signal region at high mass while only about 31 are expected. Due to the small event numbers, these deviations are likely to be fluctuations.

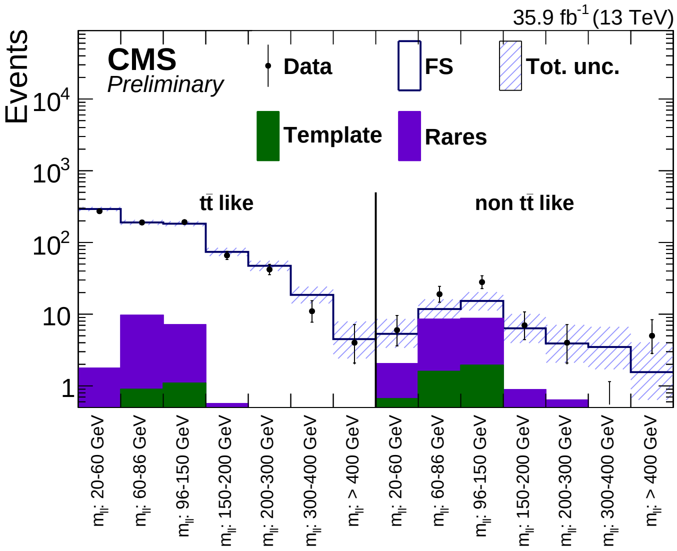

Figure 34: Results of the counting experiment of the edge search. For each of the signal region, the number of observed events, shown as black data points, is compared to the total background estimate, shown as a blue line with a blue uncertainty band. The non flavor symmetric with instrumental from the MET-template method as is shown as a green area and rare Z+ν backgrounds as a violet area.

Both legacy bins are in very good agreement with the prediction. In the PAS for ICHEP (SUS-16-021) that used the first third of the 2016 data, the event counts were 212±16 expected and 285 observed (about 3 σ local significance). With the full dataset, the September rereco of the data, the removed electron trigger emulation cut, updated rare MC samples for the prediction and updated likelihood pdfs the deviation is completely gone ($636.8^{+33.2}_{-32.3}$ events are expected and 638 observed).

As a cross check of the result obtained using data-driven techniques, a comparison of the observed data to MC simulation of the SM backgrounds is shown in Fig. 35 for SF and OF events in the baseline signal region. The Z window (86-96 GeV) is excluded again. Both SF and OF sample show reasonable agreement with the MC prediction. The largest disagreements between data and MC is observed in the OF 300-400 GeV mass bin (about 11 events in MC and 20 in data).

The covariance and correlation matrices of all 14 edge signal bins can be observed in Fig. 36. They have been produced with the HiggsCombine tool accordingly to the instructions on slide 37 and 38 of `https://indico.cern.ch/event/576113/contributions/2331065/attachments/1352728/2043018/SUSY_SL_MC.pdf`.

6.2 Results of the electroweak search

The results of the electroweak regions can be seen in the on-Z analysis note complementing this document [**?**].

6.3 Results of the kinematic fit

The dilepton mass distributions and the results of the fit in the baseline signal region are shown in Fig. 37 and 38 for the fits without and with signal model. A signal yield of 61.4 ± 27.9 events is obtained when evaluating the signal hypothesis in the baseline signal region, with an edge

Table 18: Results of the edge-search counting experiment for event yields in the signal regions. The statistical and systematic uncertainties are added in quadrature. ttbar like refers to $NLL < 21$, non-ttbar like to $NLL \geq 21$.

mass range [GeV]	FS	Template	Rares	Sum	observed
ttbar like					
20-60	$290.9^{+20.7}_{-19.7}$	0.4±0.3	1.4±0.5	$292.7^{+20.7}_{-19.7}$	273
60-86	$180.5^{+15.7}_{-14.7}$	0.9±0.7	8.8±3.4	$190.1^{+16.1}_{-15.1}$	190
96-150	$175.5^{+15.4}_{-14.4}$	1.1±0.9	6.0±2.4	$182.7^{+15.7}_{-14.6}$	192
150-200	$73.3^{+10.4}_{-9.2}$	0.1±0.1	0.4±0.2	$73.9^{+10.4}_{-9.2}$	66
200-300	$46.9^{+8.4}_{-7.3}$	0.1±0.1	0.3±0.1	$47.3^{+8.4}_{-7.3}$	42
300-400	$18.5^{+5.7}_{-4.5}$	0.0±0.0	0.0±0.0	$18.6^{+5.7}_{-4.5}$	11
>400	$4.3^{+3.4}_{-2.1}$	0.0±0.0	0.1±0.0	$4.5^{+3.4}_{-2.1}$	4
non ttbar like					
20-60	$3.3^{+3.2}_{-1.8}$	0.7±0.5	1.4±0.5	$5.3^{+3.3}_{-1.9}$	6
60-86	$3.3^{+3.2}_{-1.8}$	1.6±1.3	6.9±2.7	$11.8^{+4.4}_{-3.5}$	19
96-150	$6.6^{+3.9}_{-2.6}$	1.9±1.5	6.8±2.7	$15.3^{+5.0}_{-4.1}$	28
150-200	$5.5^{+3.7}_{-2.4}$	0.2±0.3	0.7±0.3	$6.4^{+3.7}_{-2.4}$	7
200-300	$3.3^{+3.2}_{-1.8}$	0.2±0.2	0.5±0.2	$3.9^{+3.2}_{-1.8}$	4
300-400	$3.3^{+3.2}_{-1.8}$	0.1±0.1	0.2±0.1	$3.5^{+3.2}_{-1.8}$	0
>400	$1.1^{+2.5}_{-0.9}$	0.1±0.1	0.4±0.2	$1.6^{+2.5}_{-0.9}$	5
Super signal regions (non ttbar like)					
20-86	$6.5^{+3.9}_{-2.6}$	2.3±1.5	8.3±3.2	$17.1^{+5.3}_{-4.4}$	25
>96	$19.6^{+5.8}_{-4.6}$	2.4±1.6	8.5±3.4	$30.6^{+7.0}_{-6.0}$	44
ICHEP legacy region					
>101	$617.6^{+32.7}_{-31.8}$	19.2±5.7		$636.8^{+33.2}_{-32.3}$	638
8 TeV legacy region					
20-70	$5867.4^{+202.1}_{-201.7}$	69.5±15.6		$5936.9^{+202.7}_{-202.3}$	5894

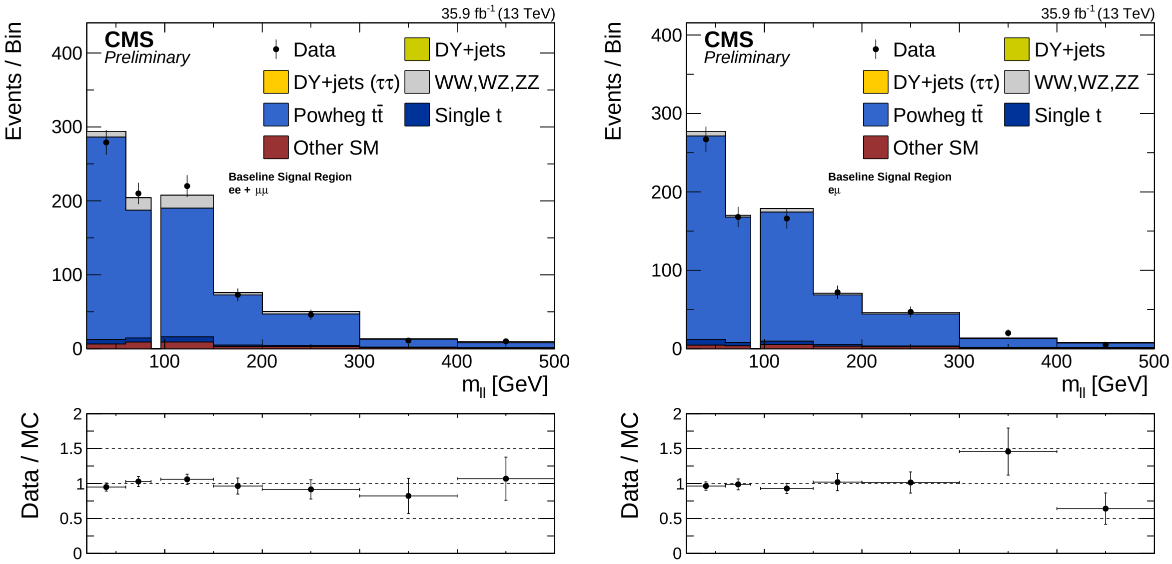

Figure 35: Data to MC comparison in the signal region for SF (left) and OF (right) leptons in the baseline signal region. Shown is the distribution of in black dots for data and stacked histograms for the different background contributions. The Z window (86-96 GeV) is excluded since it is not part of the edge search signal region. Decent agreement is observed over the full mass range for both SF and OF.

located at $144.2^{+3.3}_{-2.2}$ GeV. This is in agreement with the small upwards fluctuations in the mass regions between 96 and 150 GeV in the counting experiment. The p-value, evaluated using $-2\ln Q$, where Q denotes the ratio of the fitted likelihood value for the signal-plus-background hypothesis to the background-only hypothesis. Toy MC is used to estimate a p-value for a fixed edge position of 0.021 (local p-value) and of 0.136 in case the edge position is allowed to float (global p-value). These p-values are interpreted as the one-sided tail probability of a Gaussian distribution and corresponds to an excess in the observed number of events compared to the SM background estimate of 2.3(1.5) σ local (global) standard deviations.

In Fig. 39 a cross check using the shape for the flavor symmetric background from 8 TeV is shown. Both edge position and number of fitted signal events are in good agreement with the fit using the Crystal-Ball shape.

Table 19: Results of the unbinned maximum likelihood fit for event yields in the signal region. The quoted uncertainties account for both statistical and systematic sources.

Drell–Yan	191 ± 19
OF yield	768 ± 24
	1.07 ± 0.03
Signal events	61.4 ± 27.9
edge	$144.2^{+3.3}_{-2.2}$ GeV
Local significance	$2.3\,\sigma$
Global significance	$1.5\,\sigma$

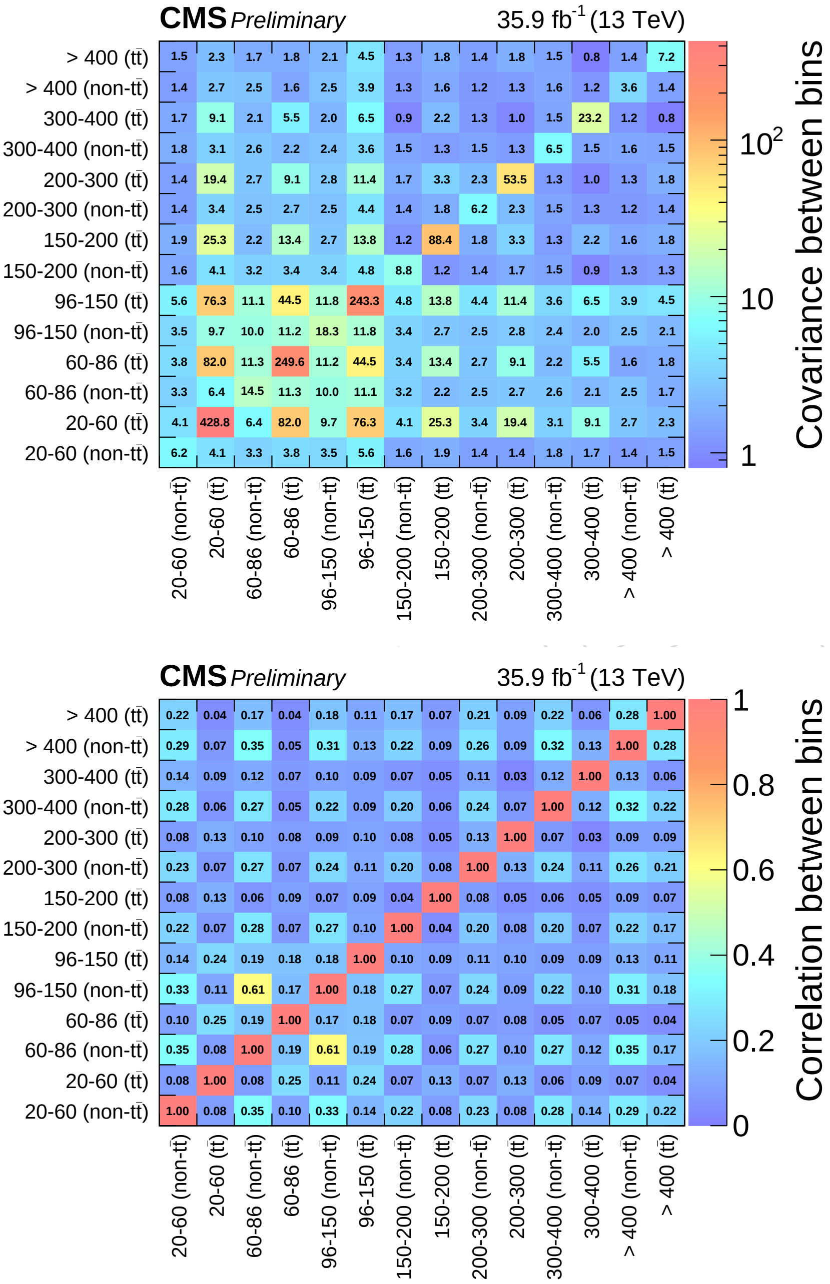

	20-60 (non-$t\bar{t}$)	20-60 ($t\bar{t}$)	60-86 (non-$t\bar{t}$)	60-86 ($t\bar{t}$)	96-150 (non-$t\bar{t}$)	96-150 ($t\bar{t}$)	150-200 (non-$t\bar{t}$)	150-200 ($t\bar{t}$)	200-300 (non-$t\bar{t}$)	200-300 ($t\bar{t}$)	300-400 (non-$t\bar{t}$)	300-400 ($t\bar{t}$)	> 400 (non-$t\bar{t}$)	> 400 ($t\bar{t}$)
> 400 ($t\bar{t}$)	1.5	2.3	1.7	1.8	2.1	4.5	1.3	1.8	1.4	1.8	1.5	0.8	1.4	7.2
> 400 (non-$t\bar{t}$)	1.4	2.7	2.5	1.6	2.5	3.9	1.3	1.6	1.2	1.3	1.6	1.2	3.6	1.4
300-400 ($t\bar{t}$)	1.7	9.1	2.1	5.5	2.0	6.5	0.9	2.2	1.3	1.0	1.5	23.2	1.2	0.8
300-400 (non-$t\bar{t}$)	1.8	3.1	2.6	2.2	2.4	3.6	1.5	1.3	1.5	1.3	6.5	1.5	1.6	1.5
200-300 ($t\bar{t}$)	1.4	19.4	2.7	9.1	2.8	11.4	1.7	3.3	2.3	53.5	1.3	1.0	1.3	1.8
200-300 (non-$t\bar{t}$)	1.4	3.4	2.5	2.7	2.5	4.4	1.4	1.8	6.2	2.3	1.5	1.3	1.2	1.4
150-200 ($t\bar{t}$)	1.9	25.3	2.2	13.4	2.7	13.8	1.2	88.4	1.8	3.3	1.3	2.2	1.6	1.8
150-200 (non-$t\bar{t}$)	1.6	4.1	3.2	3.4	3.4	4.8	8.8	1.2	1.4	1.7	1.5	0.9	1.3	1.3
96-150 ($t\bar{t}$)	5.6	76.3	11.1	44.5	11.8	243.3	4.8	13.8	4.4	11.4	3.6	6.5	3.9	4.5
96-150 (non-$t\bar{t}$)	3.5	9.7	10.0	11.2	18.3	11.8	3.4	2.7	2.5	2.8	2.4	2.0	2.5	2.1
60-86 ($t\bar{t}$)	3.8	82.0	11.3	249.6	11.2	44.5	3.4	13.4	2.7	9.1	2.2	5.5	1.6	1.8
60-86 (non-$t\bar{t}$)	3.3	6.4	14.5	11.3	10.0	11.1	3.2	2.2	2.5	2.7	2.6	2.1	2.5	1.7
20-60 ($t\bar{t}$)	4.1	428.8	6.4	82.0	9.7	76.3	4.1	25.3	3.4	19.4	3.1	9.1	2.7	2.3
20-60 (non-$t\bar{t}$)	6.2	4.1	3.3	3.8	3.5	5.6	1.6	1.9	1.4	1.4	1.8	1.7	1.4	1.5

	20-60 (non-$t\bar{t}$)	20-60 ($t\bar{t}$)	60-86 (non-$t\bar{t}$)	60-86 ($t\bar{t}$)	96-150 (non-$t\bar{t}$)	96-150 ($t\bar{t}$)	150-200 (non-$t\bar{t}$)	150-200 ($t\bar{t}$)	200-300 (non-$t\bar{t}$)	200-300 ($t\bar{t}$)	300-400 (non-$t\bar{t}$)	300-400 ($t\bar{t}$)	> 400 (non-$t\bar{t}$)	> 400 ($t\bar{t}$)
> 400 ($t\bar{t}$)	0.22	0.04	0.17	0.04	0.18	0.11	0.17	0.07	0.21	0.09	0.22	0.06	0.28	1.00
> 400 (non-$t\bar{t}$)	0.29	0.07	0.35	0.05	0.31	0.13	0.22	0.09	0.26	0.09	0.32	0.13	1.00	0.28
300-400 ($t\bar{t}$)	0.14	0.09	0.12	0.07	0.10	0.09	0.07	0.05	0.11	0.03	0.12	1.00	0.13	0.06
300-400 (non-$t\bar{t}$)	0.28	0.06	0.27	0.05	0.22	0.09	0.20	0.06	0.24	0.07	1.00	0.12	0.32	0.22
200-300 ($t\bar{t}$)	0.08	0.13	0.10	0.08	0.09	0.10	0.08	0.05	0.13	1.00	0.07	0.03	0.09	0.09
200-300 (non-$t\bar{t}$)	0.23	0.07	0.27	0.07	0.24	0.11	0.20	0.08	1.00	0.13	0.24	0.11	0.26	0.21
150-200 ($t\bar{t}$)	0.08	0.13	0.06	0.09	0.07	0.09	0.04	1.00	0.08	0.05	0.06	0.05	0.09	0.07
150-200 (non-$t\bar{t}$)	0.22	0.07	0.28	0.07	0.27	0.10	1.00	0.04	0.20	0.08	0.20	0.07	0.22	0.17
96-150 ($t\bar{t}$)	0.14	0.24	0.19	0.18	0.18	1.00	0.10	0.09	0.11	0.10	0.09	0.09	0.13	0.11
96-150 (non-$t\bar{t}$)	0.33	0.11	0.61	0.17	1.00	0.18	0.27	0.07	0.24	0.09	0.22	0.10	0.31	0.18
60-86 ($t\bar{t}$)	0.10	0.25	0.19	1.00	0.17	0.18	0.07	0.09	0.07	0.08	0.05	0.07	0.05	0.04
60-86 (non-$t\bar{t}$)	0.35	0.08	1.00	0.19	0.61	0.19	0.28	0.06	0.27	0.10	0.27	0.12	0.35	0.17
20-60 ($t\bar{t}$)	0.08	1.00	0.08	0.25	0.11	0.24	0.07	0.13	0.07	0.13	0.06	0.09	0.07	0.04
20-60 (non-$t\bar{t}$)	1.00	0.08	0.35	0.10	0.33	0.14	0.22	0.08	0.23	0.08	0.28	0.14	0.29	0.22

Figure 36: Covariance (top) and correlation (bottom) matrices for the edge signal regions. Mass regions are indicated by the stated ranges and likelihood bins via the (non) $t\bar{t}$ label in brackets.

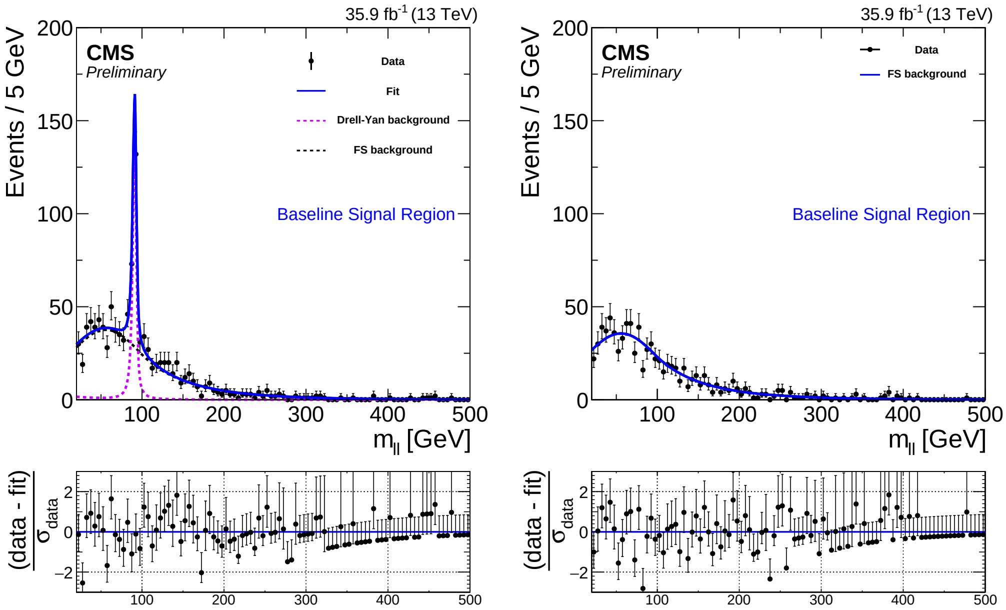

Figure 37: Result of fit in signal region for same-flavor (left) and opposite-flavor (right) events for **data** evaluating the **null hypothesis**.

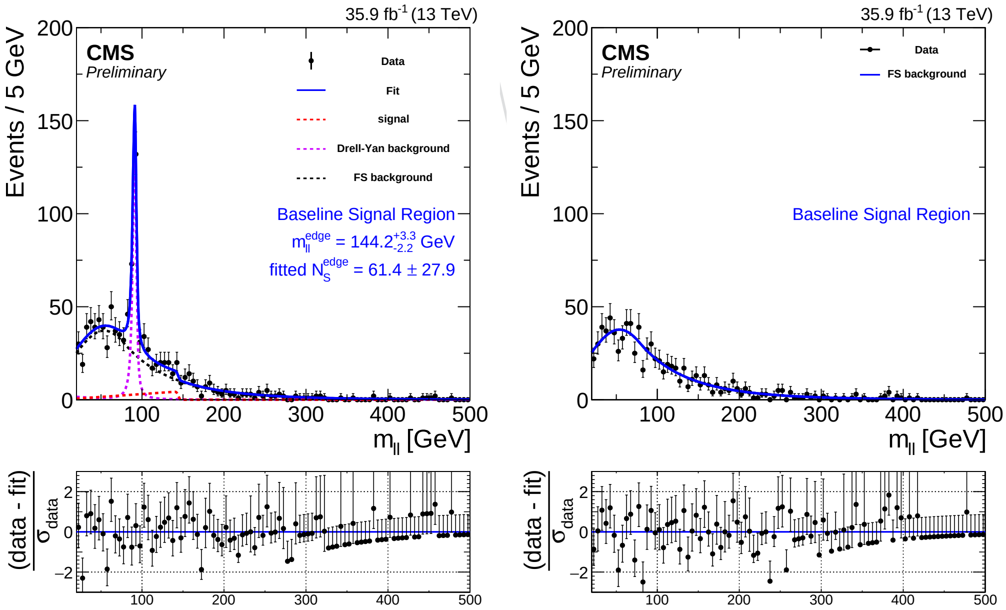

Figure 38: Result of fit in signal region for same-flavor (left) and opposite-flavor (right) events for **data** evaluating the **signal hypothesis**.

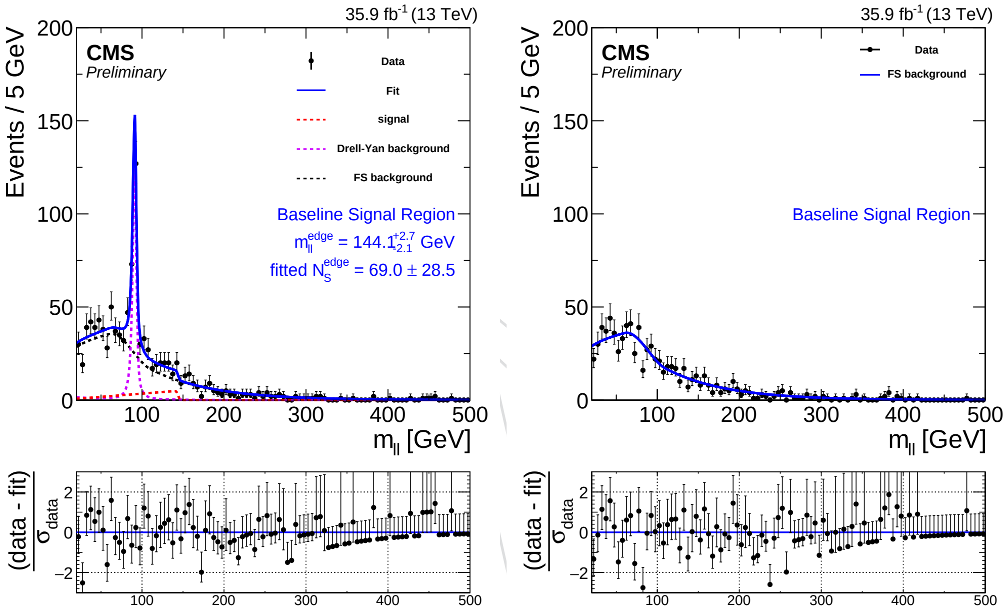

Figure 39: Result of fit in signal region for same-flavor (left) and opposite-flavor (right) events for **data** evaluating the **signal hypothesis** using the flavor symmetric shape from 8 TeV.

7 Interpretation

In this section we interpret the results of the analysis in terms of the simplified models described in section 3.

7.1 Systematic uncertainty on signal events in the edge search

The uncertainty related to the measurement of the integrated luminosity is 2.6%. The uncertainty of the corrections to account for lepton reconstruction differences between the data and simulations is 6% for dimuon and 3% for dielectron events which results in an uncertainty of about 5% on the SF yield. A further systematic uncertainty of 4% (2% per lepton) is considered on the scale factors correcting for the differences between fast and GEANT4 simulations for leptons and 3% are assumed for each dilepton trigger efficiency (see Section 4.1.2).

The influence of other uncertainty sources on the signal acceptance varies between different parts of the phase space. In general, the non-ttbar like signal regions have a larger signal acceptance and are less influenced by these uncertainties. The uncertainty due to the b-tagging efficiency is quite small for most points but can reach up to 5% in certain parts of phase space. Jet energy scale variations have nearly no impact in the non ttbar like case, except for points directly at the diagonal where the uncertainty is about 1.5%. The effect is larger for ttbar like regions and accounts for an uncertainty of 1-5%. The uncertainty associated with the modeling of initial-state radiation (ISR) is below 1% in the non ttbar like case and ranges up to 2.5% in the ttbar like regions. Determining the signal acceptance in a high pileup and low pileup regime seperately, yields a 1-2% uncertainty on the pileup indepentent of the actual signal region. To account for uncertainties in in fast simulation, the evaluation of the signal yield is repeated using generator . The average of both yields is used for the signal yields and the difference between this value and the yield using standard is used as an uncertainty that ranges from 0-4%. Varying the Q^2 scale changes the signal acceptance by 1-3%. Finally the statistical uncertainty on the number of simulated events is also considered and ranges from 1-15% depending on the mass point and signal region. These uncertainties are summarized in Table 20.

7.1.1 Applied scale factors for leptons

All scale factors applied follow the latest SUSY PAG recommendation: Tracking reconstruction factors are applied for both electrons and muons. For muons scale factors for the medium ID, miniIso0.2 vs. medium ID, $d_{xy} < 0.05$, $d_z < 0.1$ vs Medium ID, and SIP3D < 4 vs Medium ID are applied as well. For electrons the additional scale factors are: MVA Tight ID + TightIP2D + TightIP3D, MiniIso < 0.1, and ConvVeto + MissHits = 0. For the signal MC the corresponding FullSim/FastSim scale factors are applied on top of the data/FullSim MC SFs.

7.2 Interpretation of the electroweak on-Z search

The interpretation of the electroweak regions can be seen in the on-Z analysis note complementing this document [**?**].

7.3 Interpretation of the edge search

The edge search is interpreted using the slepton-edge model, combining the seven invariant mass and two likelihood regions. The left plot in figure 40 shows the exclusion contour in the plane of the masses of the bottom squark and the second neutralino. We exclude bottom squark masses up to 1200 GeV. Since the mass edge is located about 100 GeV below the mass and most of the signal events enter the non ttbar like signal bins just below this edge position certain features can be observed in the limit plot. The decrease in sensitivity at a neutralino mass of

Table 20: List of systematic uncertainties taken into account for the signal yields and typical values in the edge search.

Source of uncertainty	Uncertainty (%)	
	ttbar like	non ttbar like
Luminosity	2.6	
Lepton reconstruction and isolation	5	
Fast simulation scale factors	4	
Trigger modeling	3	
Jet energy scale	0-1.5	1-5
ISR modeling	0-1	0-2.5
Pileup	1-2	1-2
b tag modeling	0-3	0-5
Fast simulation MET uncertainty	0-1.5	0-4
Q^2 scale	1	1-3
Statistical uncertainty	1	3-15
Total uncertainty	9	10-18

$\sim$ 200–250 GeV corresponds to a kinematic edge located at $\sim$ 100–150 GeV. In this case, signal events fall into the signal regions with the highest background prediction and in some cases have an invariant mass close to the Z boson mass and do not fall into any of the regions. The observed limit in this regime is even weaker than the expected one due to the 2.0 σ deviation in the non ttbar like, 96-150 GeV mass bin. For high masses, the majority of signal events fall into the highest non ttbar like mass bin, where 5 events are observed and 1.5 expected. This results in a weaker observed limit for these mass points. The 300-400 GeV non ttbar like mass bin contains an underfluctuation of 0 observed events vs. 3.5 expected and causes the stronger observed limit at about 500 GeV of mass.

The observed significances for this model is shown in the right plot of figure 40. Here, the regimes where certain mass bins dominate can be observed as well. The significance is about 1.5 σ for high masses and for masses at about 300 GeV. The signal bin with the underfluctuation causes the low observed significance at 500 GeV mass.

References

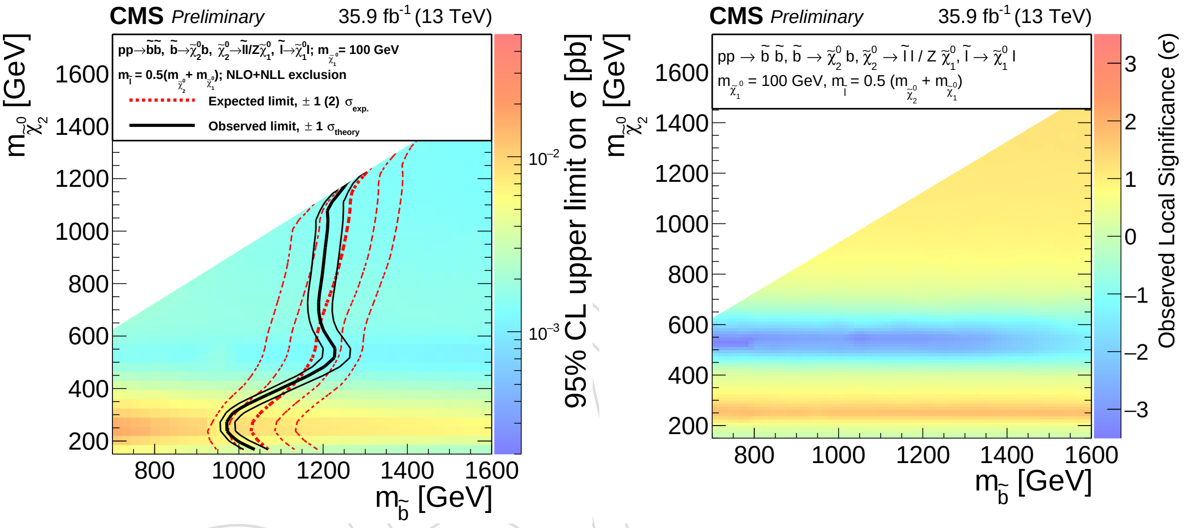

Figure 40: Cross section upper limits and exclusion contours at 95% CL with the results of the edge search interpreted in the slepton-edge model (left) and observed significances (right). The region to the left of the red dotted (black solid) line shows the masses which are excluded by the expected (observed) limit.